Effects of the Solar Cycles and Longer-Term Solar Variations: Modulation of Galactic Cosmic Radiation and Filtration of Neutral Atoms from the Local Interstellar Medium

BY

Fatemeh Rahmanifard
B.Sc., Amirkabir University of Technology, 2007
M.Sc., Amirkabir University of Technology, 2011

THESIS

Submitted to the University of New Hampshire
in Partial Fulfillment of
the Requirements for the Degree of

Doctor of Philosophy
in
Physics

September, 2019

This thesis has been examined and approved in partial fulfillment of the requirements for the degree of Doctor of Philosophy in Physics by:

Thesis Director, Dr. Nathan Schwadron, Presidential Chair, Norman S. and Anna Marie Waite Physics Professor
Dr. Eberhard Möbius, Physics Professor Emeritus
Dr. Martin Lee, Physics Professor Emeritus
Dr. Lynn Kistler, Physics Professor
Dr. Karsten Pohl, Physics Professor

On July 22, 2019.

Original approval signatures are on file with the University of New Hampshire Graduate School.

DEDICATION

To my mom and dad,

to my sisters,

to my brother,

and to Hamid,

for being who they are.

ACKNOWLEDGEMENTS

First and foremost, I would like to thank my advisor, Nathan Schwadron, for being a source of inspiration and support, and for teaching me what it takes to be a physicist.

I am thankful for Eberhard Möbius who has been an endless source of knowledge and patience. I appreciate all the time and effort he devoted to answering my questions.

I would also like to thank Marty Lee, Lynn Kistler, and Karsten Pohl for accepting to serve on my committee and for setting good examples of dedicated scientists.

Many thanks to all my friends and colleagues at UNH, on the IBEX team, on the CRaTER team, and to my amazing coauthors from whom I learned a lot.

TABLE OF CONTENTS

LIST OF TABLES

LIST OF FIGURES

LIST OF ACRONYMS

ACE — Advanced Composition Explorer

ACR — Anomalous Cosmic-Ray

AU — Astronomical Unit

aFINM — analytical Full INtegration Model

BON — Badhwar-O'Neil

BON14 — Badhwar-O'Neil 2014

BS — Bow Shock

CACTus — Computer Aided CME Tracking

CME — Coronal Mass Ejections

COSTEP — COmprehensive SupraThermal and Energetic Particle analyzer

CRaTER — Cosmic Ray Telescope for the Effects of Radiation

CRIS — Cosmic Ray Isotope Spectrometer

EMMREM — Earth-Moon-Mars Radiation Exposure Module

ESA — ElectroStatic Analyzer

E-Step — Energy Step

FAX — Female Adult voXel

FWHM — Full Width at Half Maximum

GCR — Galactic Cosmic Ray

GMIRs — Globally Merged Interaction Regions

HCS — Heliospheric Current Sheet

HIDH — Human Integration Design Handbook

HMF — Heliospheric Magnetic Field

HMI — Helioseismic and Magnetic Imager

HP — HelioPause

HZETRN — High-charge(Z) and Energy TRaNsport

IBEX — Interstellar Boundary EXplorer

ICMEs — Interplanetary Coronal Mass Ejections

IMAP — Interstellar Mapping and Acceleration Probe

ISEE — International Sun-Earth Explorer

ISM — InterStellar Medium

ISN — InterStellar Neutral

LASCO — Large Angle and Spectrometric COronagraph

LASP — Laboratory for Atmospheric and Space Physics

LET — Linear Energy Transfer

LIS — Local InterStellar

LISM — Local InterStellar Medium

LRO — Lunar Reconnaissance Orbiter

Lyα — Lyman Alpha

MAS — Magnetohydrodynamics Algorithm outside a Sphere

MAX — Male Adult voXel

MCNP6 — Monte Carlo N-Particle transport code 6

MHD — MagnetoHydroDynamics

NAO — North Atlantic Oscillation

NCRP — National Council on Radiation Protection and measurements

NEP — North Ecliptic Pole

NGRIP — North GReenland Ice Core Project

NRC — National Research Council

PCR — PaleoCosmic Radiation

PELs — Permissible Exposure Limits

PMD — Permissible Mission Durations

PREDICCS — Predictions of Radiation from REleASE, EMMREM, and Data Incorporating the CRaTER, COSTEP

REID — Risk of Exposure-Induced Death

REleASE — Relativistic Electron Alert System for Exploration

SDO — Solar Dynamics Observatory

SEP — Solar Energetic Particle

SILSO — Sunspot Index and Long-term Solar Observations

SOHO — SOlar and Heliospheric Observatory

SOLSTICE — SOLar STellar Irradiance Comparison Experiment

STEREO — Solar and Terrestrial RElations Observatory

SUMER — Solar Ultraviolet Measurement of Emitted Radiation

SWAN — Solar Wind ANisotropies

TS — Termination Shock

TEP — Tissue Equivalent Plastic

UARS — Upper Atmosphere Research Satellite

VLISM — Very Local InterStellar Medium

WTPM — Warsaw Test Particle Model

UV — UltraViolet

ABSTRACT

Effects Of The Solar Cycle And Longer-Term Solar Variation: Modulation Of Galactic
Cosmic Radiation And Filtration Of Neutral Atoms From The Local Interstellar Medium

by

Fatemeh Rahmanifard
University of New Hampshire, September, 2019

Recent solar conditions include a prolonged solar minimum (2005-2009) and a weak solar maximum. The Heliospheric Magnetic Field (HMF) strength was consistently weaker in solar cycle 24 compared to the previous maxima during the space age. These anomalies may indicate that we are entering an era of persistent decline in solar activity. In my first study, I investigated past solar secular (grand) minima, especially the Maunder period (1645-1715) to gain further insight into grand minima. I found the timescale parameters associated with the magnetic flux balance in the heliosphere. I also investigated the existence of a floor in the heliospheric magnetic flux, in the absence of coronal mass ejections (CMEs), and showed that a floor ≤ 1.49 nT is sufficient to successfully describe the HMF evolution.

As a result of the unprecedentedly low solar activity, the fluxes of galactic cosmic rays (GCRs) have increased to levels never reported previously in the space age, which might limit safe human space exploration over long-term missions (e.g., to Mars). In my second study, I used data from the Cosmic Ray Telescope for the Effects of Radiation (CRaTER) on the Lunar Reconnaissance Orbiter (LRO) to examine the correlation between the heliospheric

magnetic field, solar wind speed, and the modulation potential of the GCRs through cycle 24. I applied this correlation to past secular minima conditions, including the Dalton minimum (1790-1830) and the Gleissberg minimum (1890-1920) as extreme scenarios, to estimate the deep space radiation environment throughout cycle 25. I showed that these scenarios could lead to significant increases in dose rates (up to $\sim 60\%$). I used these results to predict the most conservative permissible mission durations (PMD) based on 3% risk of exposure-induced death (REID) in interplanetary space.

Variations in the level of solar activity affect our heliosphere's interaction with the Very Local Interstellar Medium (VLISM), as well. As the sun moves through the LISM, neutral atoms travel through the heliosphere and can be detected by IBEX. We consider Interstellar neutral (ISN) hydrogen atoms with a drifting Maxwellian distribution function in the LISM that travel on almost hyperbolic trajectories to the inner heliosphere. They are subject to solar gravity and radiation pressure as well as ionization processes. For ISN H, the radiation pressure, which exerts an effective force comparable to gravitation, decelerates individual atoms and shifts the longitude of their observed peak relative to that of ISN He. I used the peak longitude of the observed flux in the lowest energy channel of IBEX-Lo to investigate how radiation pressure shifts the ISN H signal over almost an entire solar cycle (2009 to 2018). Thus, I have created a new methodology to determine the Lyα effective radiation pressure over gravity (μ_{eff}) from IBEX ISN H data. My analysis indicates an increase of μ_{eff} with solar activity albeit with substantial uncertainties. My study of IBEX H response functions prepares for future IMAP data, which will enable a significant reduction of the uncertainties and improvements in our understanding of the effects of radiation pressure on interstellar neutral atoms.

CHAPTER 1

Introduction

1.1 From The Milky Way to Our Solar System

Our Galaxy, The Milky Way, has a spiral form with a diameter on the order of 5×10^4 pc. Our Solar system is located $\sim 2/3$ the way out from the center on an outer spiral arm. The spiral arms are composed of stars and interstellar medium (ISM) consisting of ions, electrons, neutral atoms, and dust. Atomic hydrogen is the dominant component of the ISM neutral gas.

The Local Interstellar Medium (LISM) is a bubble extending by about 30 pc in the Galactic plane and about 200 pc toward the galactic north pole. The LISM gas is similar to the hottest phase of the ISM, which seems to be the remnant of a single supernova explosion from $\sim 10^5$ years ago (McKee and Ostriker, 1977; Cox and Anderson, 1982).

The region within ~ 3.5 pc of our solar system appears to be more dense than the gas in the LISM, often referred to as the Local Cloud (Frisch, 1986). The very local interstellar medium (VLISM) is the innermost part of the Local Fluff, which includes a region of space within 0.01 pc (2000 AU) of the Sun (Holzer, 1989). Recent studies suggest the possibility that our heliosphere is currently at the edge of the LIC in some sort of boundary region (for example McComas et al., 2015a; Schwadron et al., 2015). The VLISM is the region of space referred to when addressing the penetration of neutral atoms and Galactic cosmic rays (GCRs) into the heliosphere.

The Sun continuously sheds a supersonic stream of ions and electrons, known as the solar wind, which shapes a bubble-like structure in the surrounding VLISM. This bubble is called the Heliosphere and has a relative motion with respect to the VLISM at a speed of ~ 25 km/s. The solar wind and the interstellar plasma are both highly conductive fluids and their encounter forms the heliospheric interface with distinctive features. The four basic elements of this interface are the solar wind plasma, the LISM plasma, the LISM neutrals, and the GCRs. GCRs are energetic charged particles, likely accelerated in supernova explosions, that diffuse deep into the heliosphere from the VLISM. Their low flux does not allow a significant effect on the dynamics of the interface (See Section 4.1). ISN H (and He into some extent), on the other hand, is coupled to both the VLISM and solar wind through charge exchange. As a result, it affects the dynamics of the interaction region profoundly, and its extension into the inner heliosphere drastically changes the nature of the solar wind as well.

At the termination shock (TS), the supersonic solar wind decelerates to subsonic speeds, forming a collisionless hydromagnetic shock. Inside the termination shock, the heliospheric magnetic field (HMF), generally described by the Parker spirals, is the dominant feature. Beyond a cavity of $\sim 6 - 10$ AU, due to ionization, the interstellar neutral (ISN) hydrogen is the main constituent of the solar wind. The charge exchange between ISN H and the solar wind plasma leads to the production of pickup ions so that near the TS the internal energy of the solar wind is dominated by the pickup ions. The pick-up process itself leads to low-frequency turbulence, which in turn causes isotropization of the pickup ion population, heating of the solar wind and scattering of GCRs. At the termination shock, a fraction of the pickup ions will be further energized and accelerated up to MeV energies to form the anomalous cosmic-ray (ACR) component. The TS probably has a complicated shape that changes both temporally and spatially with variations of the solar wind. The solar wind at the TS becomes compressed, heated and turbulent. The region between the TS and the heliopause is called the inner heliosheath.

The heliopause (HP) is a discontinuity between the VLISM plasma and the subsonic solar wind, where the pressure of the solar wind and VLISM is balanced. In reality, a distinct HP surface might be idealized since diffusion and other interactions blur the HP, extending it spatially. As the solar wind becomes decelerated and heated at the TS , its dominant ram pressure transforms to thermal pressure at the HP. On the other side of the HP, the VLISM plasma pressuer consists mainly of magnetic and ram pressure. Schwadron and Bzowski (2018) showed that for an interstellar magnetic field of $\sim 3\mu$G the ram pressure dominates, leading to a commet-like shape for the heliosphere, with a tail in the downwind of the the ISN flow.

In models with supersonic VLISM flow, there is an additional bow shock (BS) upstream of the interaction region, where the interstellar plasma starts to react to the obstacle created by the heliosphere. As a result, the interstellar plasma is diverted, decelerated, and heated as the VLISM magnetic field is draped around the heliosphere. The same process might occur through a bow wave, in the absence of a BS (see McComas et al., 2012; Zank et al., 2013).

Far away from the heliospheric interface, the ionized and neutral parts of the VLISM are highly coupled through charge exchange and elastic collisions. The neutral part of the VLISM still moves toward the Sun after passing the BS (or bow wave). In the outer heliosheath, the space between the BS and the HP, charge exchange leads to the creation of two new ion and neutral populations: Newly ionized particles are deflected with the VLISM plasma whereas neutralized atoms decouple from the VLISM magnetic field and create a secondary population. This population is hotter and slower than the primary flow and piles up to form the hydrogen wall (for a more detailed discussion see Frisch et al., 2009).

Most of the topics discussed in this section are adapted from the Zank et al. (1998) review paper, the Hall (1992) Ph.D. thesis, and Frisch et al. (2009). The basic elements of the heliospheric interface and the features it creates are shown schematically in Figure 1.1. This figure is adapted from Bzowski (2017).

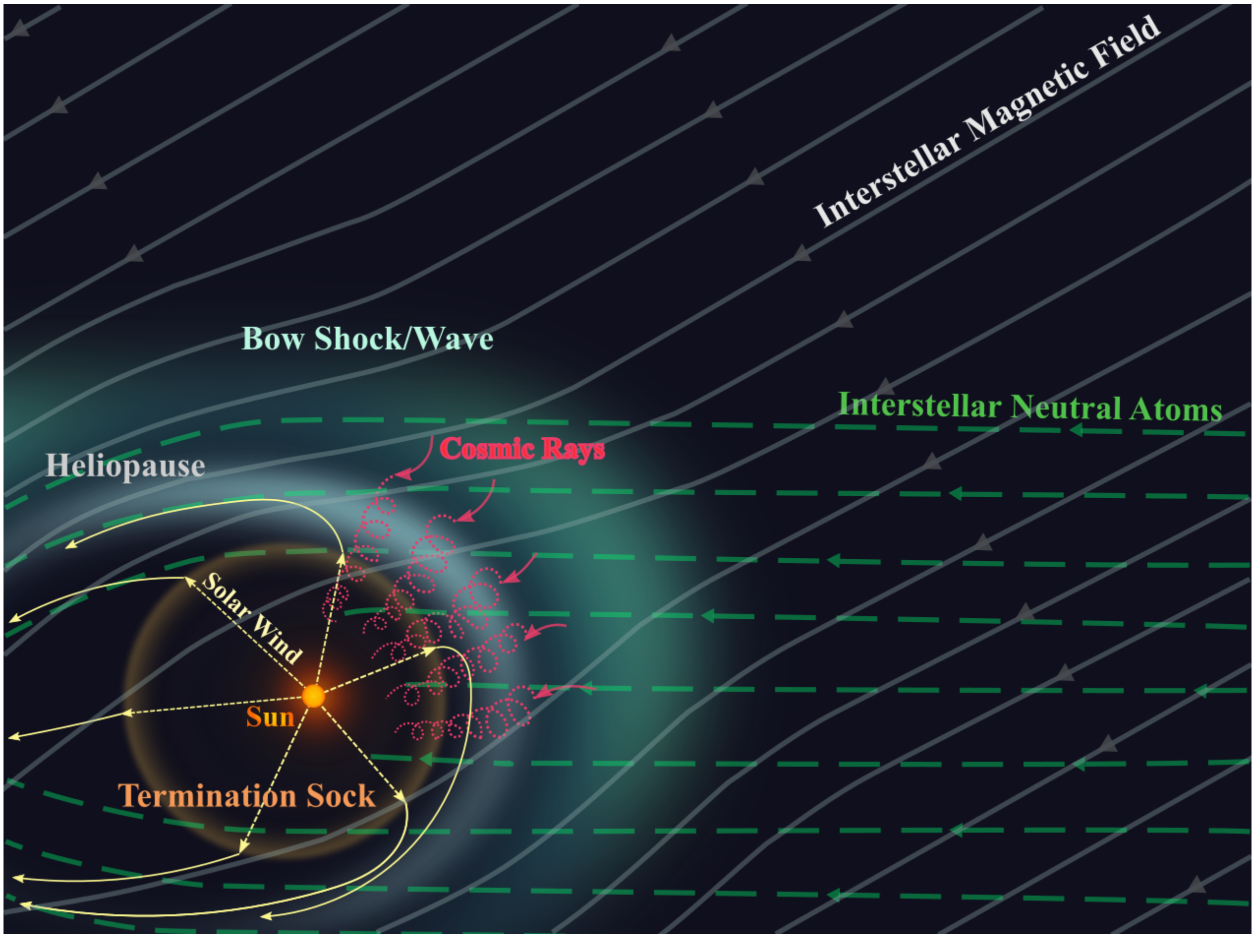

Figure 1.1 A schematic view of the heliospheric interface. This figure is adapted from Bzowski (2017). The four basic elements of the heliospheric interface can be seen, including the interstellar neutral part, interstellar plasma (which moves along the interstellar magnetic field), the solar wind, and the GCRs.

1.2 An Overview of This Research

In this work, I investigate solar variations and their effects on the interaction between the heliosphere and the LISM. Figure 1.2 provides an overview of my research and the relation between the three studies presented in this work. Solar variations range from seconds to centuries. My focus in this study is on the 11-year solar cycles and longer-term variations, known as secular variations. In Chapter 2, we review the heliospheric magnetic field (HMF) and its variations through different phases of solar cycles to provide background for Chapter 3. Chapter 3 presents my study 1, published in the Astrophysical Journal (Rahmanifard et al., 2017), where I investigated the processes attributed to the magnetic flux balance in the heliosphere. In my first study, I reconstructed time series for the HMF intensities back through the Maunder period to show the HMF evolution during periods of extremely low activity, which may be important in the context of the recent decline in solar activity.

The recent unprecedented decline in the strength of solar cycles started with the prolonged solar minimum of cycle 23 (2008-2009) and persisted to the shallow solar maximum of cycle 24 and its subsequent deep solar minimum. This might indicate that we are at the beginning of a secular solar minimum. As a result, we have observed the highest fluxes of GCRs in the space age and relatively few solar energetic particle events. Despite the rare occurrence of the solar energetic particle (SEP) events, the September 2017 event was extremely hard, carrying the largest dose rates in the most shielded detectors of CRaTER (the Cosmic Radiation Telescope for the Effects of Radiation). The radiation from GCRs and SEPs challenge the success of human space missions beyond the magnetic shielding of the Earth, though in different ways. SEPs are associated with short-term or acute radiation effects, due to their sporadic nature, while the GCRs are associated with long-term effects that pose a threat for the space mission's crew. In my second study, I investigate the effect of solar variations, in this case, a persistent decline in solar activity, on the space radiation environment, that mostly consists of SEPs and GCRs. In Chapter 4, we investigate the September 2017 event to demonstrate the radiation risk from discrete solar energetic particle events. Chapter 4 presents some of the work that is published in the Schwadron et al. (2018) paper, published in Space Weather. In Chapter 5, we focus on the radiation hazard from the GCRs that might limit safe human space exploration over long-term missions (e.g., to Mars). In this chapter, we investigate the possible space radiation environment and its resulting limits on human space exploration if the next solar cycle leads us to a deeper phase of a secular solar minimum. This part of study 2 will be submitted to Space Weather in the near future (Rahmanifard et al., 2019a).

In my third study, I investigated the effect of variations in the level of solar activity over a complete solar cycle on the flow of ISN H. Heliospheric distributions of ISN atoms are affected primarily by gravitation, charge exchange collisions, photoionization, and for ISN H, radiation pressure. The radiation pressure is caused by a resonant interaction between Lyα photons and hydrogen atoms, resulting in a radially outward force acting on ISN H atoms. During phases of low solar activity, radiation pressure is less effective in decelerating ISN H atoms since the emission of Lyα irradiance drops dramatically, due to a decrease in active regions. In this study, I concentrated on a quantitative determination of the effect of radiation pressure on ISN H, in particular, on the longitudinal shift of the ISN H peak over almost a full solar cycle. Based on these observations, I created a new methodology to determine the Lyα effective radiation pressure from IBEX (Interstellar Boundary Explorer) ISN H data. Chapters 6 and 7 present this study, which is submitted to the Astrophysical Journal and is currently under revision (Rahmanifard et al., 2019b). A brief overview and outlook of this research is provided in Chapter 8.

All these studies are presented in coauthored papers. Throughout this thesis pronoun"I" has been used to refer to my contribution to this research. Wherever I use "we", I am referring to a contribution of a coauthor or a genuinely collaborative work. "We" has also been used to refer to the reader and author together.

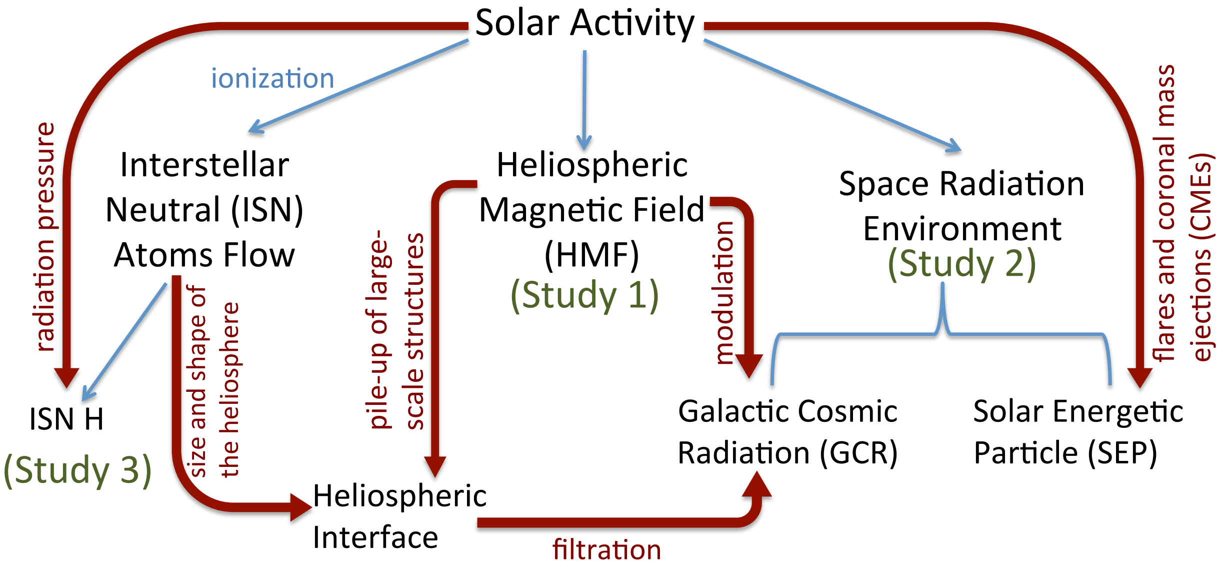

Figure 1.2 An Overview of This Research. This diagram shows different elements of my research and their relation.

CHAPTER 2

Variations of the Heliospheric Magnetic Field with Solar Cycles

2.1 Introduction

Variations of the heliospheric magnetic field (HMF) range from seconds to centuries. The shortest time scales are associated with waves and turbulence which result in fine-scale HMF structure. The $\sim$ 27-day solar rotation period can be noticed in the solar wind parameters. The nearly-periodic 11-year changes in the Sun's activity, corresponding to a switch in the polarity of the solar magnetic field and most famously known as solar cycles, is evident in various factors including the level of solar radiation, sunspot records, and coronal mass ejections (CMEs) and flares frequencies. It takes two solar cycles, or 22 years, before the solar magnetic field returns to its original configuration, known as the Hale cycle. The secular minima/maxima occurring on the scale of centuries are evident in the paleocosmic radiation (PCR) data, sunspot records, and geomagnetic records. This chapter aims to provide adequate background for Chapter 3, which includes my study 1 on the evolution of the HMF published in the Astrophysical Journal (Rahmanifard et al., 2017). Most of the discussion provided in this chapter is adopted from/ inspired by Owens and Forsyth (2013) and Schwadron et al. (2008).

2.2 HMF Variations with Solar Cycles

2.2.1 Steady-State HMF

The heliospheric magnetic field lines that are shaped into Parker spirals are in fact excursions of the coronal magnetic field into the interplanetary space. The coronal magnetic field, in turn, is controlled by the photospheric plasma motions. Most of the photospheric flux, which forms coronal loops, is "closed". The high coronal temperature leads to the formation of the solar wind and increasing its gas pressure until it exceeds the magnetic pressure in the source surface. Beyond this surface, the solar wind drags the coronal magnetic field out into the heliosphere, forming the HMF. These field lines can only connect at the boundary of the heliosphere and for heliospheric purposes are considered as "open". The bulk of the field lines, which stay below the source surface do not contribute to the HMF carried by the solar wind (e.g. Wang and Sheeley, 2003). Between $\sim$ 10 to 50% of the coronal loops (Arge et al., 2002), with footpoints in the photosphere extend high enough to pass the source surface, be dragged out by the solar wind, and form the HMF.

In order to better understand the geometry of the HMF, we consider an idealized steady-state solar wind. We assume that an exactly radial outflow of the solar wind is dragging out the frozen HMF. Since the magnetic field lines have footpoints in the photosphere, and thus rotate with the Sun, they are wound into Archimedean spirals in the solar equatorial plane (Parker, 1958):

$$\mathbf{B}(R,\theta,\phi) = B_R(R_0,\theta,\phi_0)(\frac{R_0}{R})^2\hat{e_r} - B_R(R_0,\theta,\phi_0)\frac{\Omega R_0^2 \sin\theta}{V_R R}\hat{e_\phi} \tag{2.1}$$

where $B_R(R_0,\theta,\phi_0)$ is the radial component of the HMF at the source surface (distance R_0 from the Sun), at colatitude θ, and with its footpoint fixed at longitude ϕ_0., Ω is the Sun's rotational speed. This equation is deduced in Appendix A and shown schematically in Figure 2.1). This equation shows that the radial and azimuthal components of the interplanetary field behave quite differently. The radial component decreases as R^{-2}, while the azimuthal component decreases as R^{-1}. Thus as one moves out in the heliosphere the magnetic field becomes more azimuthal in the equatorial plane so that the Earth meets the HMF at $\sim 45°$.

Furthermore, the $\sin(\theta)$ term in the azimuthal component suggests that field lines can be understood as wrapped around the surface of a cone of half angle equal to the latitude θ. So that at high heliospheric latitudes, the $\sin(\theta)$ term can get very small, and in the theoretical approach, directly over the solar poles, the magnetic field becomes completely radial at all distances (See Figure 2.2).

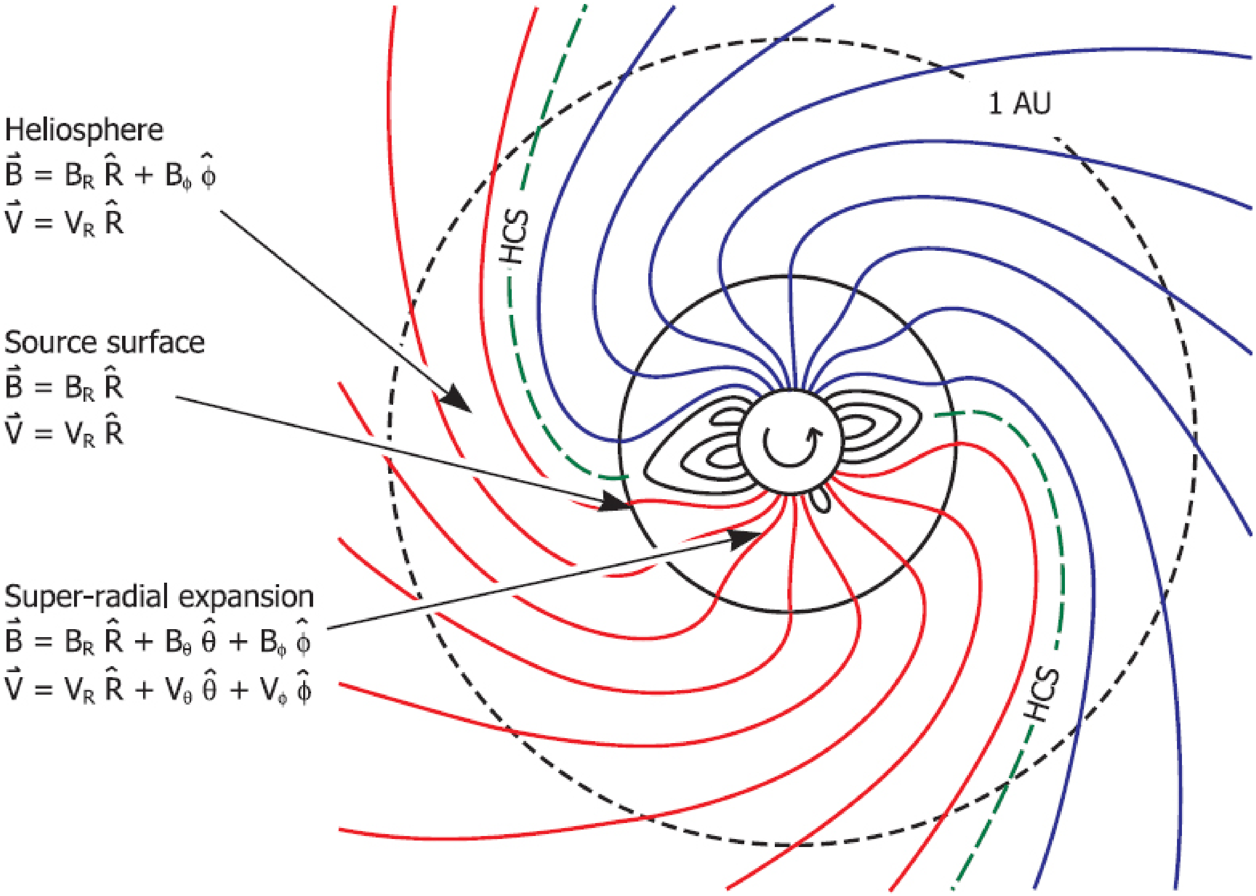

Figure 2.1 A schematic view of the steady-state solar magnetic field in the ecliptic plane. At small helio-radii, approximately within the boundaries of the solar corona, the coronal magnetic field dominates the plasma flow, exhibiting significant non-radial (super-radial) behavior. At $\sim 2.5R_s$ known as the source surface, the gas pressure exceeds the magnetic pressure leading both the field lines and the solar wind to become purely radial. Beyond this surface, rotation of the footpoints of the field lines frozen into a radial solar wind leads to a spiral geometry. A small tilt between the magnetic and rotational axes causes both inward (blue solid lines) and outward (red solid lines) polarities to be present at the ecliptic plane, with a two-sector structure (as shown in this figure).The green dashed line, which separates regions of opposite HMF polarity, show the heliospheric current sheet (HCS). The HCS encircles the Sun close to the ecliptic plane. The quadrupolar component of the field (increasing during solar maximum) leads to a more complex sector structure along with creating wavy spiral shape in the HCS, simillar to a ballerina's skirt. This figure is adopted from Owens and Forsyth (2013).

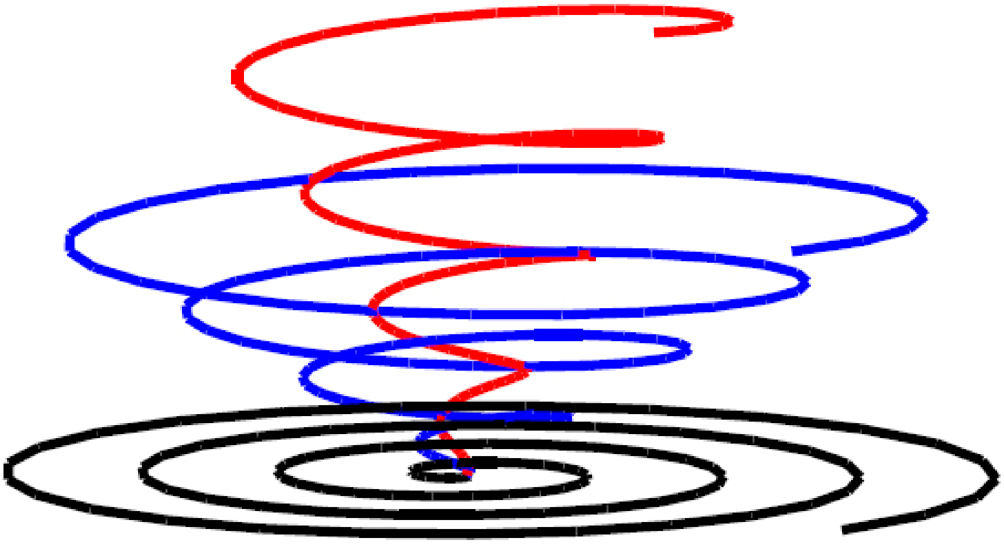

Figure 2.2 Ideal Parker spirals with a solar wind speed of 450 kms^1. Black, blue, and red lines respectively represent latitudes of 0°, 30°, and 60°. This figure is adopted from Owens and Forsyth (2013).

2.2.2 HMF at Solar Minimum

During solar minimum, the solar magnetic field can be adequately described by dipolar behavior leading to Parker spirals throughout most of the heliosphere, with a small inclination between the magnetic and rotational axes. However, there are still non-dipolar structures, which introduce more complex patterns to the ecliptic HMF. Near the equator, an equal (B_r) cannot be restored at the source surface without a significant non-radial expansion below this surface.

At solar minimum, coronal holes and thus the open magnetic flux that rises into the HMF is predominantly confined to the polar regions. Fast solar wind originates from the unipolar regions over the poles, and thus fast solar wind fills the high-latitude heliosphere. The slow solar wind, on the other hand, is expected at low latitudes, where opposite magnetic polarities meet to produce the heliospheric current sheet (HCS). The HCS encircles the Sun close to the rotational equator and thus the ecliptic plane, although still with some little warps due to weak quadrupole distortions. Due to the small tilt between the magnetic and rotational axes, near the ecliptic plane, alternate fast and slow solar wind streams can be observed.

2.2.3 HMF at Solar Maximum

At solar maximum, the solar magnetic field is at its most dynamic. The coronal magnetic field evolves rapidly, leading to frequent releases of huge eruptions of solar plasma and magnetic field known as coronal mass ejections (CMEs). CMEs move out through the corona and into the heliosphere, and therefore, can be considered as a source of transforming closed coronal magnetic flux into open heliospheric flux. CMEs do occur during solar minimum, although at much lower frequencies.

Furthermore, during phases of solar maximum, quadrupolar and higher-order moments of the coronal magnetic field dominate (e.g. Hoeksema, 1991; Wang et al., 2000). Although an approximately dipolar field is still present, it has a very high tilt to the rotation axis. The increased non-dipolar structures lead to an increase in the total open solar flux, although in smaller spatial concentrations. As a result, large coronal holes are torn into small active regions spread at all latitudes, which in turn lead to a reduction in the occurrence of the fast solar wind. This results in the slow solar wind becoming ubiquitous throughout the heliosphere. A summary of Section 2.2.3 and Section 2.2.2 is presented in Figure 2.3 adopted from Owens and Forsyth (2013). For a more thorough discussion covering all the topics mentioned in Section 2.2 see Owens and Forsyth (2013).

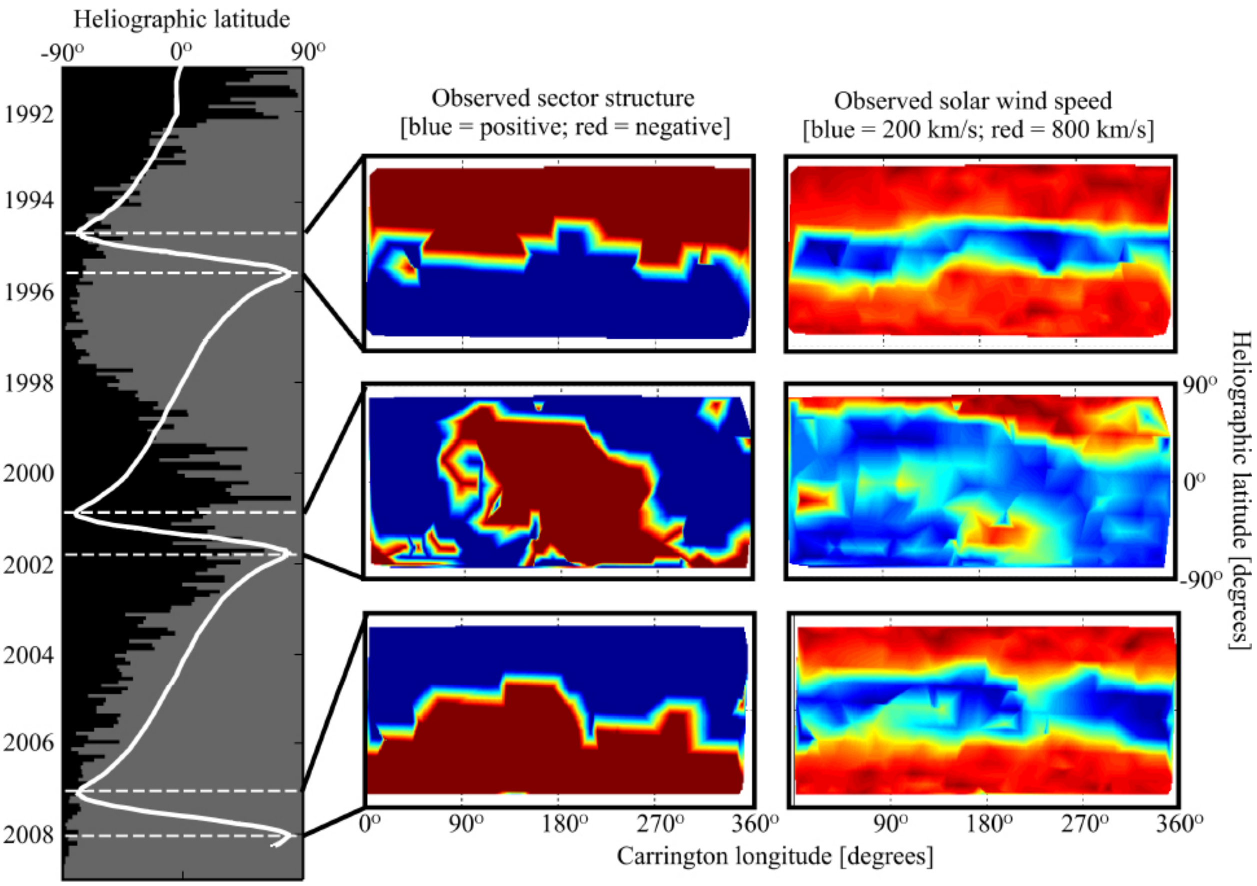

Figure 2.3 Summary of Ulysses observations. The left-hand panel presents the heliographic latitude of the spacecraft (white line), overlaid on the sunspot number. The three panels in the center are maps of magnetic field polarity, where blue (red) represents inward (outward) polarity, during the three fast-latitude scans of Ulysses. The three panels on the right demonstrate solar wind speed, with blue through red showing 200 to 800 kms^{-1}, during the three fast-latitude scans of Ulysses. This figure is adopted from Owens and Forsyth (2013).

2.2.4 Evolution of the HMF through a Solar Cycle

The 22-year cycles which returns the solar magnetic field to its original configuration is named after George E. Hale who linked sunspots and the solar magnetic field. A qualitative model for variations of solar magnetic field with solar cycles was proposed in 1961, based on differential rotation of the Sun (Babcock, 1961). This model, known as Babcock model or Babcock-Leighton dynamo model, was advanced to describe the oscillatory exchange of energy between poloidal and toroidal solar magnetic field components as a driving force for solar cycles. In this model, the toroidal quadrupolar magnetic field is generated by buoyant upwelling within the convective zone,which is itself created by the differential rotaton of the Sun (Figure 2.4) and reaches its maximum during solar maximum. This quadrupolar field is responsible for the emergence of active regions. A poloidal dipolar field, on the other hand, is created by the shift of energy from the toroidal field to the poloidal field, during declining phase of the solar cycle, so that the poloidal field's maximum/minimum coincides with solar minimum/maximum (Babcock, 1961; Leighton, 1969).

There are different theories about how the open field reverses. One theory is that the Sun sheds its open flux and creates the new open flux of the reversed polarity from one solar minimum to the next (Wang and Sheeley, 2003). Another approach, proposed by Fisk and Schwadron (2001), considers open magnetic flux a conserved quantity. They argue that migration of the open flux, through reconnection between open field lines and a large underlying medium of closed loops, can lead to a massive rotation of open flux. In these reconnection processes, the footpoints of the open magnetic field lines and the footpoints of one side of the loops are interchanged (Crooker et al., 2002). Through such interchange reconnection processes, the net amount of open magnetic flux remains conserved. Therefore, in this scenario, the reversal of the open flux should be thought of as a reconfiguration of the open magnetic flux.

Figure 2.5 shows a sketch of the evolution of the open magnetic flux and migration of the open field lines through interchange reconnection with CMEs as a source of transient magnetic flux throughout a full solar cycle. The Alfvén surface, where the solar wind speed equals the Alfvén speed and beyond which field lines are considered “open” to the heliosphere, is shown in dashed line in this figure. The beginning stages of the rising phase in solar activity is demonstrated in the first panel. An increase in the coronal magnetic content leads to closed loops that pass the Alfvén radius and undergo interchange reconnection with ambient open flux, which leads to an extension of the coronal holes and migration of the open flux toward lower latitudes. In the second panel, the pre-reversal phase is shown, in which the Sun is closer to a maximum and the increasing release of CMEs triggers more intense interchange reconnection leading to greater extensions of coronal hole boundaries. Eventually, a configuration is reached at which polar coronal holes are replaced by a series of smaller coronal holes spread unevenly about the Sun. The third panel shows the Sun in the post-reversal phase, where continued induction of CMEs leads to new polar coronal holes with reversed polarity. In the fourth panel, the declining phase is presented, where solar activity quiets, and the Sun moves into a solar minimum configuration with its large-scale field reversed.

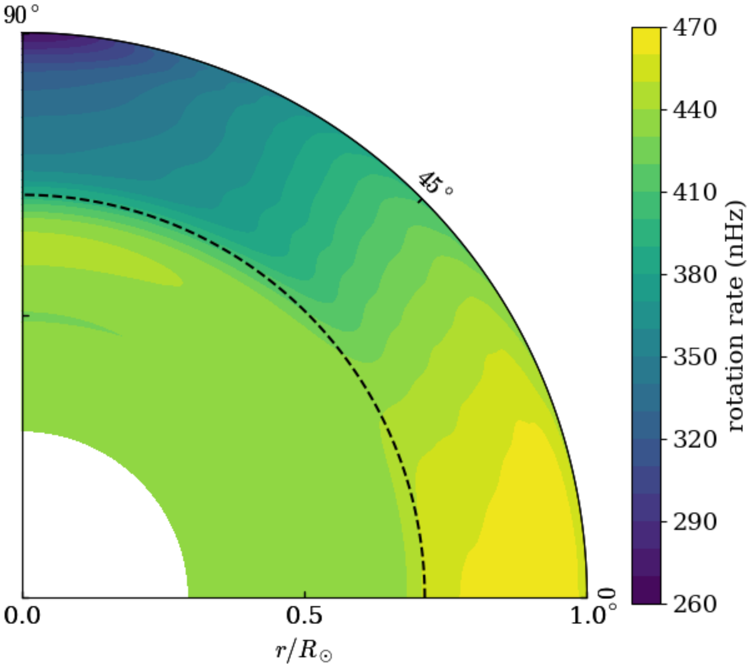

Figure 2.4 The internal rotation profile of the Sun from the Helioseismic and Magnetic Imager (HMI) data aboard the Solar Dynamics Observatory (SDO). The dashed line shows the base of the solar convection zone.

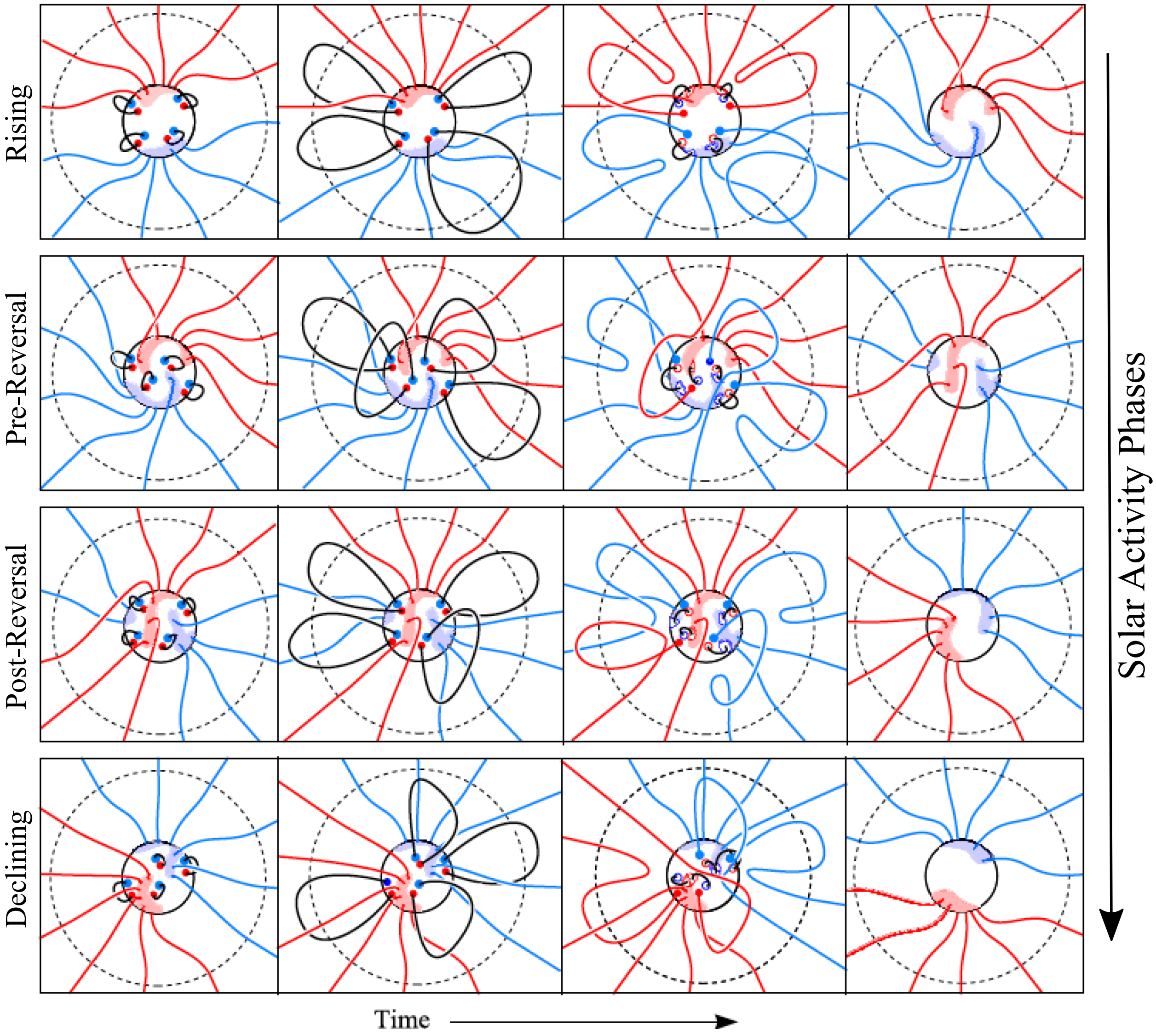

Figure 2.5 A sketch of the evolution of the HMF. The source surface is shown in black dashed lines. Light red (blue) shaded regions represent negative (positive) polarity of the coronal holes. The inward (outward) magnetic field lines are shown in red (blue). Closed CME loops are shown in black, with the red (blue) circles showing the polarity of the footpoints. This figure is adopted from Schwadron et al. (2008).

2.3 Long-Term Variations of the HMF

As stated previously in Section 2.1, sunspot records, PCR data, and geomagnetic records can be used to investigate the secular variation of the HMF. Sunspots are associated with large-scale magnetic features in the photosphere, and hence can be used as a proxy for solar activity. A new release of sunspot and group sunspot records are introduced in Appendix B. There is a well-established anti-correlation between the galactic cosmic ray (GCR) fluxes and HMF intensity. Stronger HMF coupled with increased irregularities in the heliospheric magnetic content due to a disturbed, tilted HCS can modulate the energetic ions penetrating from the outer space, thus decreasing GCR fluxes. Cosmogenic isotope abundances, in ice-core records, can provide proxies for GCR flux, and thus, the HMF thousands of years into the past. Sunspot records and PCR data are discussed at length in Chapter 3.

Historic geomagnetic activity observations can be used to obtain solar wind parameters at 1 AU, including the intensity of the HMF and solar wind speed. Lockwood (2013) provides a complete review of the methods and techniques of reconstructing geomagnetic data. For the past 135 years, there is a good agreement between various methods due to sufficient reliable magnetic observations being available.

In Figure 2.6, 22-year averages of open solar flux obtained from ^{10}Be and ^{14}C abundances in polar ice-cores since 1610 (red and blue lines) are extended to the space age using neutron monitor records (see Muscheler et al., 2007; Lockwood and Fröhlich, 2008, and references therein for more detail). The long-term secular variations, such as the Gleissberg, Dalton and Maunder minima, as well as the space age/modern maximum, are clearly evident in this figure. Investigating a full record of PCR data suggests that secular maxima similar to what was observed through the space age have occurred previously on 24 occasions in the last 9300 years, though the space age maximum has been the longest in the record (Abreu et al., 2008). Maunder minimum-like conditions have been reported within 50 years from the end of two previous secular (grand) solar maxima (Barnard et al., 2011).

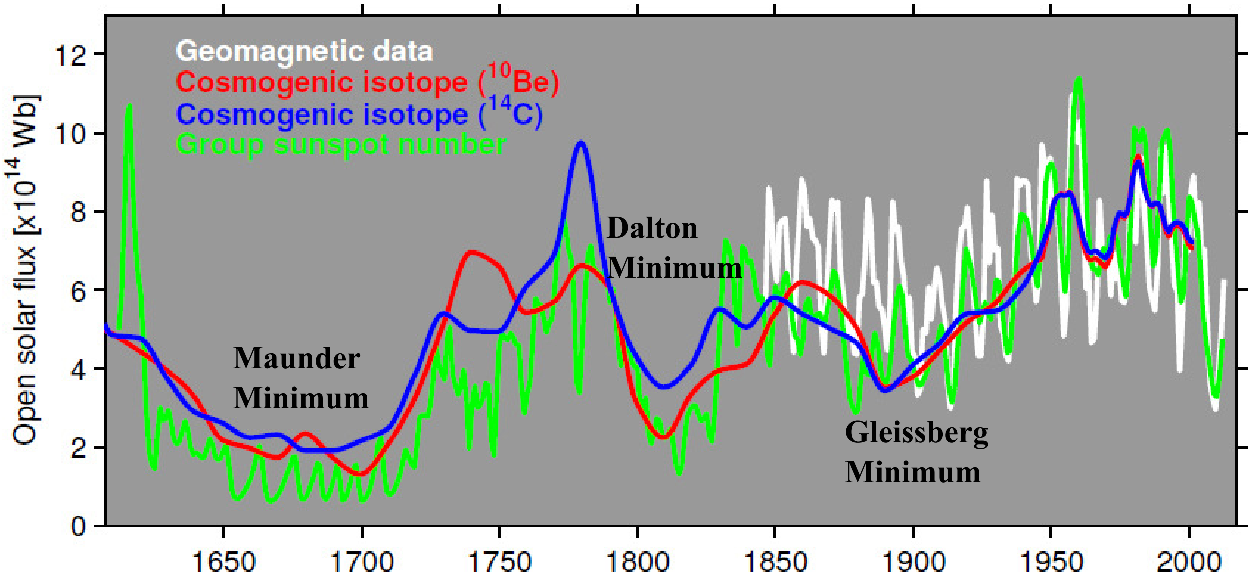

Figure 2.6 Reconstructions of the total open solar flux since 1610, based on geomagnetic reconstructions (Lockwood et al., 2013b,a, white), Group sunspot number (Owens and Lockwood, 2012, green) , Cosmogenic isotope reconstructions using ^{14}C(blue) and ^{10}Be (red) (see Lockwood and Fröhlich, 2008, for more detail). This figure is adopted from Owens and Forsyth (2013).

2.4 Conclusion

At the end of the long secular maximum observed in the space age, the unprecedented decline in the strength of solar cycles has been persisting over a decade. This might indicate that we are at the beginning of a secular solar minimum. In Chapter 3 we investigate the processes attributed to the magnetic flux balance in the heliosphere. We find the timescales associated with these processes and reconstruct a time series for the HMF intensities back through Maunder period. This study shows HMF evolution during periods of extremely low activity, which may be important in the context of the recent solar conditions. Chapter 3 presents my study 1, published in the Astrophysical Journal (Rahmanifard et al., 2017).

CHAPTER 3

Inferring the Heliospheric Magnetic Field Back through the Maunder Minimum (Study 1)

3.1 Introduction

It has been over 150 years since Heinrich Schwabe discovered that the sunspot number varies with 11-year solar cycles. Since then it has been well established that the solar cycle is in phase with changes in the heliospheric magnetic field (HMF) (see Lockwood, 2003; McCracken, 2007; Smith and Balogh, 2008; Lockwood et al., 2009; Connick et al., 2009, 2011; Smith et al., 2013; McCracken et al., 2013). Sunspot records and reconstructed HMF show that $\sim$ 11 year Schwabe cycles are superimposed on longer time-scale cycles (e.g., Grand Minima/Maxima, see Usoskin et al. 2012). These secular variations are defined in Solanki et al. (2000) as "changes that occur on timescales of centuries."

Although sunspots can be seen by the naked eye, the invention of telescopes in the early 1600s led to a reliable recorded telescopic observation of the sunspots. During the Maunder Minimum (1645-1715), the reported number of sunspots is unusually low (Ribes and Nesme-Ribes 1993), raising the question of whether this period is actually a prolonged sunspot minimum rather than an ordinary secular minimum. However, Schröder (1992) and Beer et al. (1998) used auroral data and cosmogenic ^{10}Be to show that during this period the solar cyclicity was normal, though with low activity, suggesting that the Maunder Minimum is a secular minimum with suppressed Schwabe cyclicity. Zolotova and Ponyavin (2015) suggested that the sunspot number from the Maunder Minimum is underestimated, and concluded that it can be an ordinary secular minimum although their work is largely disputed for example by Usoskin et al. (2015). The new sunspot number and sunspot group number released by Sunspot Index and Long-term Solar Observations (SILSO) are corrected for the large underestimation before 1850. The group sunspot number is reconstructed to show higher group numbers for the Maunder Minimum though the number is still remarkably low (Svalgaard and Schatten, 2016). The so-called “backboning” method used to obtain this data set is questioned by Lockwood et al. (2016), arguing that it leads to an overestimation of the sunspot group numbers as we go back in time. Recently other sunspot and sunspot group number data sets have been proposed by Lockwood et al. (2016); Usoskin et al. (2016); and Vaquero et al. (2015).

Schrijver et al. (2011) address the discrepancy between sunspot numbers and the reconstructed HMF data from the Maunder Minimum (the magnetic field intensity derived from ground-based measurements of ^{10}Be atoms captured in ice cores known as paleocosmic radiation data, PCR), suggesting that even during the least active phases of the Maunder Minimum, when no sunspots are observed, ephemeral regions still persist. An ephemeral region is an area of the Sun where a magnetic dipole, or flux tube, surfaces on the disk and eventually produces a bipolar sunspot group. Previously, Solanki et al. (2000) had used the sunspot number as a proxy to describe the flux emergence rate in active regions and ephemeral regions. Solanki et al. (2002) improved their model by adding an extended cycle attributed to small ephemeral regions. Although the field flux tubes indicated by these ephemeral regions are too weak to form sunspots (Spruit, 1977), they form a minimum state of solar magnetic activity (Schrijver et al., 2011). Cliver (2012) suggested that the minimal solar activity indicated by Schrijver et al. (2011) is a requirement for a floor in the HMF intensity at 1 AU, which occurs for no CMEs. However, Wang and Sheeley (2013) disputed this by arguing that the ephemeral regions cannot have been the sole source of the magnetic flux during the Maunder Minimum: the 11 year solar cyclicity continues to be observed in ^{10}Be data through the Maunder Minimum despite the fact that ephemeral regions remain relatively unchanged over a solar cycle. Wang and Sheeley (2013) stated that the floor (if any) resulting from ephemeral regions must be much smaller than the values ~ 0.6 to 4.6 nT proposed in previous studies (Svalgaard, 2007; Owens et al., 2008; Cliver and Ling, 2011). Riley et al. (2015) introduced a set of possible configurations of the photospheric magnetic field during the Maunder Minimum and inferred the most likely configuration of the solar corona using a global MHD model. They suggested that the Sun might have started evolving from a configuration similar to the 2008-2009 minimum to an ephemeral-only configuration during the Maunder period. Owens et al. (2017) provided the first timeseries of estimates for the global solar wind variations back through the Maunder minimum using sunspot-based open solar flux reconstruction and streamer belt width. Krivova et al. (2007) used the model from Solanki et al. (2002) to investigate the evolution of the solar photospheric magnetic flux and solar total irradiance since 1700 using sunspot number (and since 1610 using sunspot group number). Vieira and Solanki (2010) successfully reproduced solar open flux reconstructed since 1904 by Lockwood et al. (2009), using an extension of the Solanki et al. (2002) model and the Krivova et al. (2007) model.

In the space age, solar activity has been relatively high but there are suggestions (brief Schwabe maximum 2011-2014 and protracted Schwabe minimum, 2005-2009) that we are entering another grand minimum (see Smith and Balogh, 2008; Connick et al., 2009, 2011; Smith et al., 2014). Owens et al. (2012) utilize an open solar flux model to anticipate how cycles 24 and 25 could develop given different scenarios for the sunspot cycle. The protracted solar minimum of 2008 and 2009 shows a reduction in solar wind speed, density, and temperature, which also results in lower solar wind particle flux (McComas et al., 2008). Goelzer et al. (2013) have shown that a failure in restoring flux levels to the previous maximum values will likely lead to a deeper minimum. They used the theory of Schwadron et al. (2010b) (Section 3.2.2) and sunspot data record since 1749 to show that the results from the model match favorably to the reconstructed HMF (PCR). Smith et al. (2013) had previously used the same parameters and techniques to compare the predicted HMF intensity with *in situ* HMF measurements from OMNI from 1963 onward.OMNI compiles a set of data including near-Earth solar wind and magnetic field parameters from multiple sources. In this study I extend their method back to 1610 to investigate the intensity of the HMF during the Maunder period.

Schwadron et al. (2010b) describe the evolution of the heliospheric magnetic flux with the closed flux injected from CMEs and the balance provided by conversion (opening), loss, and interchange reconnection of the flux (see also publications from Gosling et al., 1987; McComas et al., 1989, 1991, 1992; Crooker et al., 2001; Low, 2001; Owens et al., 2007; DeForest et al., 2012). Schwadron et al. (2010b) also allow for a minimum floor flux. Instead of using fixed parameters as in previous works, I employed a data analysis method to find parameters that best describe the HMF including the fundamental timescales that control evolution of the HMF (these time scales are introduced in Section 3.2.1). The heliospheric magnetic balance as investigated by Schwadron et al. (2010b) is briefly reviewed in Section 3.2.2. The frequency of CMEs as the source of the closed flux and the paleo-cosmic ray (PCR) reconstructed HMF data set are discussed in Sections 3.2.3 and 3.2.4. I used a chi-square minimization method to derive parameters, as explained at length in Sections 3.2.5, 3.3 by comparing the results from the theory to the geomagnetic-based data (since 1845) (Owens et al., 2016) and OMNI data (since 1963). Geomagnetic data is a source for reconstruction of historical records of near-Earth HMF, solar wind speed and open solar flux (e.g., Russell, 1975; Svalgaard, 1977; Feynman and Crooker, 1978; Cliver et al., 1998; Lockwood et al., 1999, 2013b,a, 2014b,a; Owens et al., 2016). We review implications of the study results and sources of uncertainty in Section 3.4. Concluding remarks are provided in Section 3.5. Appendix B provides detail concerning the SILSO sunspot number reconstructions applied in this work.

3.2 Theory and Background

3.2.1 Sources and Losses of the Ambient Heliospheric Magnetic Field

Coronal Mass Ejections (CMEs) are the source for the transient heliospheric magnetic flux. They harbor substantial amounts of closed magnetic flux, which evolves with time through three processes shown in Figure 3.1. The closed magnetic flux does not penetrate the Alfvén surface and therefore can be retracted into the photosphere as defined in Smith et al. (2013). In the top panel of Figure 3.1, I show the situation that results if CME-associated closed flux has the same polarity as the surrounding ambient heliospheric magnetic flux. In this case, the magnetic flux is dragged out into the solar wind, beyond the Alfvén radius (where the solar wind speed equals the Alfvén speed, typically about 12 to $40R_s$ shown as the dashed ovals in Figure 3.1), and eventually becomes a component of the ambient HMF. This leads to "conversion of transient CME magnetic flux to ambient heliospheric magnetic flux", and, at the Sun, causes the extension of coronal holes. This conversion process can grow the HMF and cause a magnetic flux catastrophe in the absence of a disconnection process (McComas et al., 1989) in the ambient magnetic field. However, the excessive ambient (or open) field lines that are newly added to the heliosphere build up transverse magnetic pressure, which compresses the plasma and enhances processes leading to the loss of the ambient heliospheric magnetic flux (McComas et al., 1991, 1992).

As shown in the middle panel (Figure 3.1), magnetic reconnection between opposite polarity magnetic flux either within CMEs or the ambient heliospheric flux leads to the conversion of magnetic flux within the heliosphere to large-scale closed fields at the Sun and loss of inverted U-shaped field structures that are convected out of the heliospheric magnetic system. We note that these inverted structures have been identified in Solar Maximum Mission (McComas et al., 1991) and STEREO data (DeForest et al., 2012). We label this process as "loss of heliospheric and CME magnetic flux."

The bottom panel of Figure 3.1 shows the process that results when CME-associated magnetic flux undergoes magnetic reconnection with the ambient HMF. This process, termed "interchange reconnection" (Crooker et al., 2001) essentially reconfigures the magnetic fields. The footpoint of the ambient HMF moves from its initial position to the matching polarity footpoint of CME magnetic field, which, at the Sun, leads to the extension of the coronal hole. A new large-scale magnetic loop is also formed in the process with a footpoint connection near the coronal hole.

The three processes shown in Figure 3.1 each have characteristic timescales identified as τ_c (**conversion**, top panel), τ_l (**loss**, middle panel) and τ_{ic}(**interchange reconnection**, bottom panel). These timescales reflect the interplay between physical processes responsible for the balance of the heliospheric magnetic flux. The conversion timescale dictates how long it takes for the CME-associated flux to convert to ambient open flux, resulting in a rise in the field magnitude during the phases of increasing solar activity and a decline during phases of low solar activity. The loss timescale is an estimate of the time it takes for the ambient field lines to get disconnected from the ambient field lines in advected U-shaped structures, prohibiting build up of the excessive ambient field lines into a magnetic flux catastrophe. The loss timescale introduces a hysteresis property to the model supported by observations (McCracken and Beer, 2014). The interchange reconnection timescale estimates the time it takes for the closed field lines to be displaced by an adjacent open field line, resulting in the extension of the coronal holes and removal of closed flux. Greater interchange reconnection timescales lead to faster increase in the strength of HMF during active solar phases and slower decline during low activity phases. In this study, I found the best values for these three parameters by comparing results from the model of Schwadron et al. (2010b) (Section 3.2.2) with geomagnetic-based data (1845 onward) and OMNI data (1963 onward).

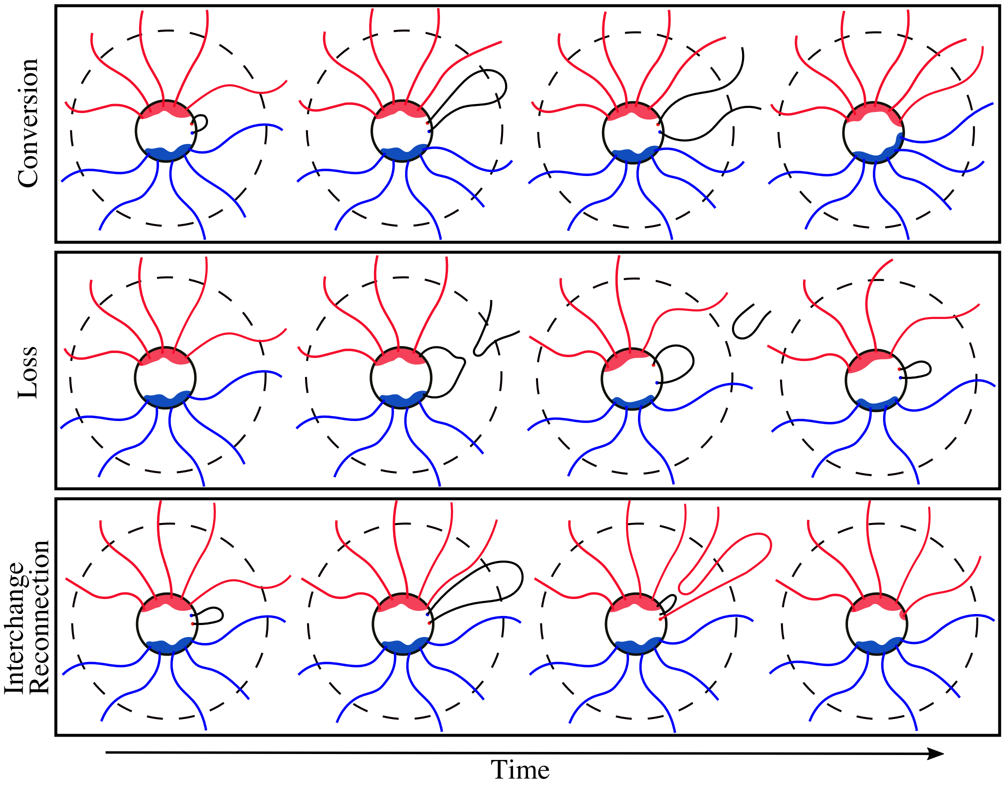

Figure 3.1 Three processes responsible for transformation of CMEs, conversion (top), loss (middle) and interchange reconnection (bottom). **The top panel** shows conversion of transient CME magnetic flux to ambient heliospheric magnetic flux. When the closed flux has the same polarity as the surrounding ambient flux, the magnetic loop is dragged out into the solar wind beyond the Alfvén surface (shown in dashed line), and eventually becomes a component of the ambient HMF. **The middle panel** shows loss of heliospheric and CME magnetic flux which closes heliospheric magnetic flux below the Alfvén surface and releases inverted U-shaped field structures. This process is responsible for removing excessive open flux and limits the growth of the HMF. **The bottom panel** shows interchange reconnection, which occurs when CME-associated magnetic flux undergoes magnetic reconnection with the ambient HMF and reconfigures the magnetic fields. This figure is adapted from Schwadron et al. (2010b).

3.2.2 Heliospheric Magnetic Flux System

Schwadron et al. (2010b) broke the heliospheric magnetic flux system into two components: the transient CME associated magnetic flux ϕ_{ej}, and the ambient heliospheric magnetic flux ϕ_{HMF}. The resulting balance of magnetic flux is derived by considering contributions of each of the processes shown in Figure 3.1:

$$\frac{d\phi_{ej}}{dt} = f(1-D)\phi_{CME} - \phi_{ej}(\frac{1}{\tau_c} + \frac{1}{\tau_l} + \frac{1}{\tau_{ic}}), \tag{3.1}$$

where f is the frequency of CME ejections (discussed in Section 3.2.3), D is the fraction of CME ejecta that reconnects immediately after release, ϕ_{CME} is the average flux of a CME. CMEs can supply their magnetic flux to the heliospheric system only if they remain closed. That is why the fraction of CMEs that open immediately through reconnection ($\sim$ 0.5) should be subtracted (Owens and Crooker, 2006). The three processes discussed in Section 3.2.1 cause a decrease in the content of closed ejecta-associated flux and thus the flux lost through these processes must be subtracted.

Schwadron et al. (2010b) take into account the source of ejecta-associated flux that evolves into the ambient heliospheric flux and the loss of flux to the heliospheric magnetic flux system. The resulting balance in heliospheric magnetic flux is expressed:

$$\frac{d\phi_{HMF}}{dt} = -\frac{\phi_{HMF} - \phi_{flr}}{\tau_l} + \frac{\phi_{ej}}{\tau_c}, \tag{3.2}$$

where ϕ_{flr} is the floor of the magnetic open flux. A floor was suggested by Owens et al. (2008) and Crooker and Owens (2010) based on the linear correlation between the magnetic field strength and the CME rate, meaning that at a zero CME rate there is a nonzero value for the field strength.Wang et al. (2000) also predicted the existence of such a floor, suggesting that pressure provided by the solar wind can drag out some heliospheric flux. Owens et al. (2008) and Crooker and Owens (2010) refered to individual solar cycles while in this study I calculated single values for the floor flux (and the three timescales) assuming constant solar wind parameters over centuries. However, the value for this floor can change locally over solar cycles depending on parameters associated with the solar wind and the timescales associated with the balance of heliospheric flux. Smith et al. (2013) and Goelzer et al. (2013) reproduced the observed HMF (OMNI data) and reconstructed PCR data using the Schwadron et al. (2010b) model assuming the floor flux to be zero. In the present work, I applied chi-square analysis to find the best values for the floor flux as well as the three timescales.

Summing the two equations above, we obtain the total magnetic flux rate of change:

$$\frac{d\phi_{tot}}{dt} = -\frac{\phi_{tot} - \phi_{flr}}{\tau_l} + f(1-D)\phi_{CME} - \frac{\phi_{ej}}{\tau_{ic}}. \tag{3.3}$$

When integrating this to get the magnetic flux balance it is important to know that Schwadron et al. (2010b) only took into account the mean heliospheric field B_{mean} and neglected any turbulent component in the field that arises from *in situ* turbulence, random footpoint motions at the Sun, and randomly distributed interchange reconnection between heliospheric footpoints and loops near the Sun. We may solve for the net magnetic flux of the mean HMF of a single polarity that intersects an idealized 1 AU sphere with unit normal $\hat{n}$:

$$\phi_{tot} = \int \mathbf{B}_{mean}.\hat{n}dS. \tag{3.4}$$

assuming that $\mathbf{B}_{mean}$ does not change with latitude. This simplifying assumption does not apply, except for large heliocentric radii and that is why we need more analysis to estimate the total flux. The integration changes sign from one side of the current sheet to the other side. The total magnetic flux is calculated from full integration over the unsigned magnetic intensity. Hereafter, we use scalar B since we are only interested in the unsigned magnetic intensity. The total field intensity also contains the toroidal field components associated with magnetic clouds and contains turbulent magnetic fluctuations, which are both absent from the definition of the mean HMF. Goelzer et al. (2013) used the OMNI *in situ* measurements of the solar wind at 1 AU starting in 1963 to show that there is a systematic ~ 2.4 nT difference between the total field and the mean field with a greater (lower) difference at solar maximum (minimum). This type of analysis had been previously applied by Connick et al. (2009, 2011) and Smith et al. (2013). Connick et al. (2009) used 45 years of OMNI data to show a linear relation between open flux density and toroidal flux density (Connick et al., 2009, Figure 4). Based on the results of Goelzer et al. (2013), I added an estimate for the field components above the mean field (obtained by averaging over the difference between the observed total field and the observed mean field from OMNI data. I also applied a variant toroidal component, assuming a linear relation between the toroidal and the mean field, explained further in Section 3.3). I, therefore, have predicted a total magnetic field intensity that can be compared directly to the average total field intensity derived by McCracken et al. (2013) using ^{10}Be, geomagnetic-based B series derived by Owens et al. (2016), and *in situ* measurements from OMNI.

3.2.3 Frequency of Coronal Mass Ejections

Schwadron et al. (2010b) assumed the frequency of CMEs can be described as a sinusoid with a steady decrease after 2006 to account for the protracted solar minimum. Smith et al. (2013) took a step further and normalized the correlation between sunspot numbers and CME rates(see Smith et al., 2013, Figure 1a and 1b). They used the normalization factor to find the frequency of CMEs based on the sunspot number, in order to compare the predicted HMF from the theory to OMNI data. Later, Goelzer et al. (2013) used the same technique to apply the theory back to 1749. Both of these papers applied monthly average sunspot number data from the NOAA Geophysical Data Center and used $f = (\frac{8}{200}) \times (sunspot\ number)$, $D = 0.5$, $\tau_c = 2.5$ years, $\tau_l = 6.0$ years, $\tau_{ic} = 20$ days, and $\phi_{flr} = 0$. Assuming the CME rate to be proportional to sunspot number ignores the near constant minimum CME rate of $0.5\mathrm{d}^{-1}$ as the sunspot number tends to zero at the end of cycle 23 (Owens et al., 2011).

In the present work using the new sunspot group number from Sunspot Index and Long-term Solar Observations (SILSO), I extended my results back to 1610 (see Appendix B), which covers the Maunder minimum by assuming a linear relationship between the sunspot number (obtained from sunspot group record) and CME rate. A chi-square analysis (as will be explained in 3.2.5) was applied to obtain a linear relationship that gives the best agreement with the CME rate. I obtained

$$f = (0.019 \pm 0.002) \times (sunspot\ number) + 0.37 \pm 0.13 \tag{3.5}$$

to get the best agreement with the CME rate observed with the Large Angle and Spectrometric Coronagraph (LASCO) from Computer Aided CME Tracking (CACTus) (Robbrecht and Berghmans, 2004; Robbrecht et al., 2009). Figure 3.2 compares the CME rate obtained from the new sunspot number, using the linear relationship, with the CME rate observed by LASCO. The CME rates used in this study are corrected to remove the effect of near-doubling of the LASCO image cadence after August 2010 by multiplying CME rates by 60/110 (Wang and Colaninno, 2014). The blue shaded area in Figure 3.2 includes two sources of uncertainty: 1) sunspot number uncertainties; and 2) the chi-square fitting and propagation uncertainties in the linear scaling of CME rate from sunspot number using Equation 3.9.

3.2.4 Paleocosmic Radiation (PCR) Data

The intensity of the galactic cosmic radiation (GCR) at Earth provides a proxy for the HMF strength, since the HMF controls the transport of cosmic rays in the heliosphere (Parker, 1965; Jokipii, 1991), resulting in 50% variations in the intensity of $\sim 1 - 3$ GeV cosmic radiation near Earth throughout the 11-year solar cycle. The GCR particles undergo collisions with atmospheric atoms, producing cosmogenic radionuclides such as ^{10}Be and ^{14}C when nucleons (protons and neutrons) are expelled from target atoms. These radionuclides are sequestered in polar ice and biological material, providing a record of the paleocosmic radiation (PCR) that stretches $> 10,000$ years into the past (Beer, 2011). Caballero-Lopez

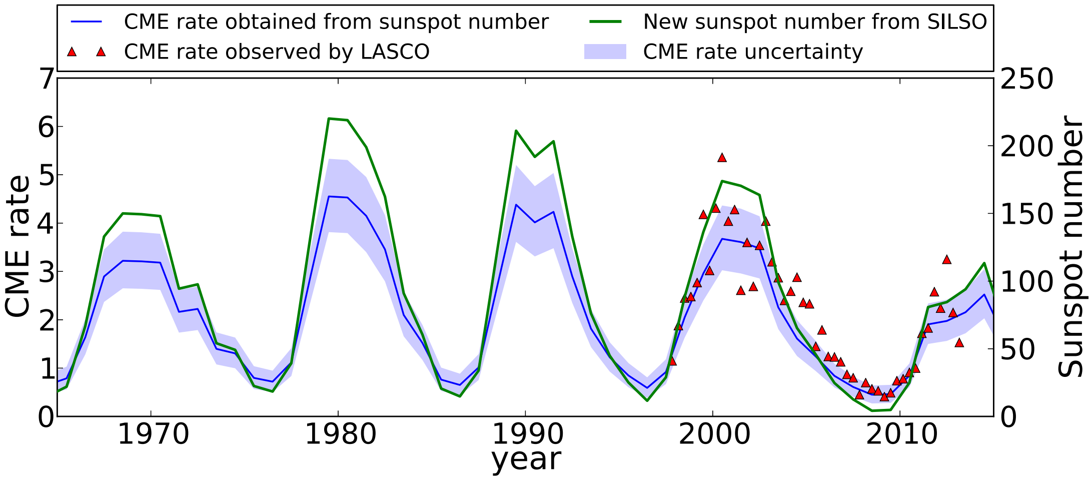

Figure 3.2 CME rate derived from sunspot number (blue curve) using Equation 3.5 is compared to CME rates (red triangles) observed by LASCO. The shaded blue area shows the uncertainty caused by sunspot number uncertainty (standard error) and the uncertainty of the linear relationship parameters obtained by chi-square method. The green line shows the new sunspot number released by SILSO.

et al. (2004) used the cosmic ray transport equation to invert the 22-year averages of the cosmic ray intensity to obtain estimates of the 22-year average of the heliomagnetic intensity since 850 AD. McCracken (2007) adapted their method to estimate the annual intensity of the HMF since 1428. More recently, McCracken and Beer (2015) extended this work to include the annual data from two ice cores that were corrected for long-term climate induced changes (Steinhilber et al., 2012) and for removal of the effects of particle radiation events (i.e., Solar Proton Events) generated by the Sun. I used this data set along with the yearly averages of OMNI HMF *in situ* measurements as my estimates of the HMF strength in the past. Note that the estimation process is not used for values of the HMF strength < 2.5 nT; the eight lowest annual data points in Figures 3.4 and 3.7 are all upper limits of 2.5 nT.

3.2.5 Chi-Square Analysis

I applied the yearly average sunspot group number data from SILSO to the theory as explained in Section 3.2.3 to find parameters that provide the best match between the model results and the two independent data sets (geomagnetic-based data and OMNI data). For the present work, I set D (the fraction of CMEs that open immediately) to be 0.5 and calculated a set of timescales (τ_c, τ_l and τ_{ic}) along with a floor in the heliospheric flux (ϕ_{flr}) for which chi-square statistics reaches its minimum value.

I calculated the chi-square for different values of these parameters in order to determine their best values

$$\chi^2 = \sum_{i=1}^{m} \frac{(O_i - M_i)^2}{\sigma_i^2} \tag{3.6}$$

where O_i is the observed value, M_i is the value obtained from the model, σ_i is the uncertainty assigned to the observed value and m is the number of the data points. In a chi-square analysis it is common to use the reduced chi-square

$$r\chi^2 = \frac{\chi^2}{n} \tag{3.7}$$

to measure the fit quality, where n is the degree of freedom defined as

$$n = m - \nu \tag{3.8}$$

where ν is the number of free parameters. The reduced chi-square is restricted to be greater than one.

We find the parameters τ_c, τ_l, τ_{ic} and ϕ_{flr} for which the reduced chi-square reaches its minimum value. The uncertainties of the parameter τ can be obtained by using the propagation and fit uncertainties determined from the chi-square dependence on fit parameters (Schwadron et al., 2016a).

$$(\delta\tau)^2 = (1 + r\chi^2_{min}) \times (\frac{d^2\chi^2}{d\tau^2})^{-1}_{min} \tag{3.9}$$

3.3 Results

Figure 3.4 compares the simulated HMF (B_{total}) shown as the dark blue line with the magnetic field derived from the ^{10}Be data set (grey circles), the magnetic field derived from geomagnetic data set (red squares with error bars) and the OMNI data set (yellow triangles with error bars). An average value of 2.36 ± 0.05 nT has been added to the predicted mean heliospheric field value in order to compensate for the role of the turbulent and toroidal components of the HMF (Goelzer et al., 2013). In order to obtain the simulated field, I applied the chi-square minimization method by varying the three timescale parameters and the floor flux to obtain the global minimum value of the reduced chi-square by fitting the resulting points to a polynomial, shown in Figure 3.3a to 3.3d. The best-fit parameters for the timescales are $\tau_c = 3.07 \pm 0.03$ years (3.3a), $\tau_l = 5.91 \pm 0.06$ years (3.3b), and $\tau_{ic} = 24.00 \pm 0.18$ days (3.3c). Varying ϕ_{flr} from 0 to 25×10^{13} Wb yields the minimum value of the reduced chi-square at 0 and fitting the resulting points to a second order polynomial yields $\phi_{flr} = (-0.19 \pm 0.54) \times 10^{13}$ Wb (3.3d). This result is statistically consistent with no magnetic flux floor. The blue shaded area in Figure 3.4 shows the uncertainty of the total HMF caused by the uncertainty of the sunspot group numbers, the uncertainty of the slope and intercept of the linear relation found between CME rates and sunspot number (Equation 3.5), the uncertainty of the three parameters found by chi-square analysis, as detailed in 3.2.5, and the uncertainty associated with the average value of the toroidal component. All the uncertainties and error bars in this figure show the 90% confidence interval.

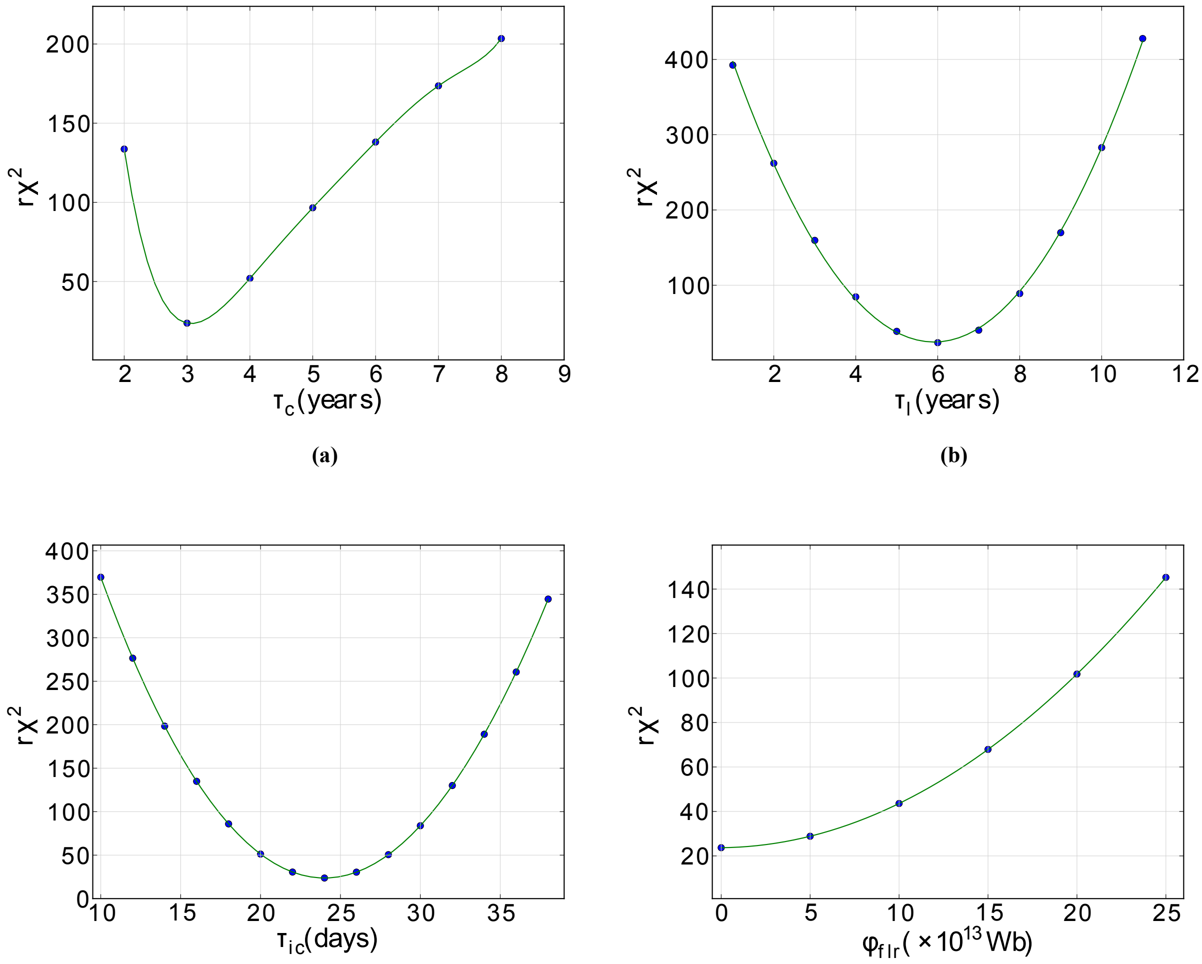

(a) **(b)** **(c)** **(d)**

Figure 3.3 (a) Reduced χ^2 vs. conversion timescale (τ_c). Other parameters (τ_l , τ_{ic} and ϕ_{flr}) are held at the χ^2 minimum values. $\tau_c = 3.07 \pm 0.03$ years minimizes the reduced chi-square. (b) Reduced χ^2 vs. loss timescale (τ_l). Other parameters (τ_c, τ_{ic} and ϕ_{flr}) are held at the χ^2 minimum values. $\tau_l = 5.91 \pm 0.06$ years minimizes the reduced chi-square. (c) Reduced χ^2 vs. interchange reconnection timescale (τ_{ic}). Other parameters (τ_c, τ_l and ϕ_{flr}) are held at the χ^2 minimum values. $\tau_{ic} = 24.00 \pm 0.18$ days minimizes the reduced chi-square. (d) Reduced χ^2 vs. floor flux (ϕ_{flr}). Other parameters (τ_c, τ_l and τ_{ic}) are held at the χ^2 minimum values. As can be seen zero value for the ϕ_{flr} minimizes the reduced chi-square.

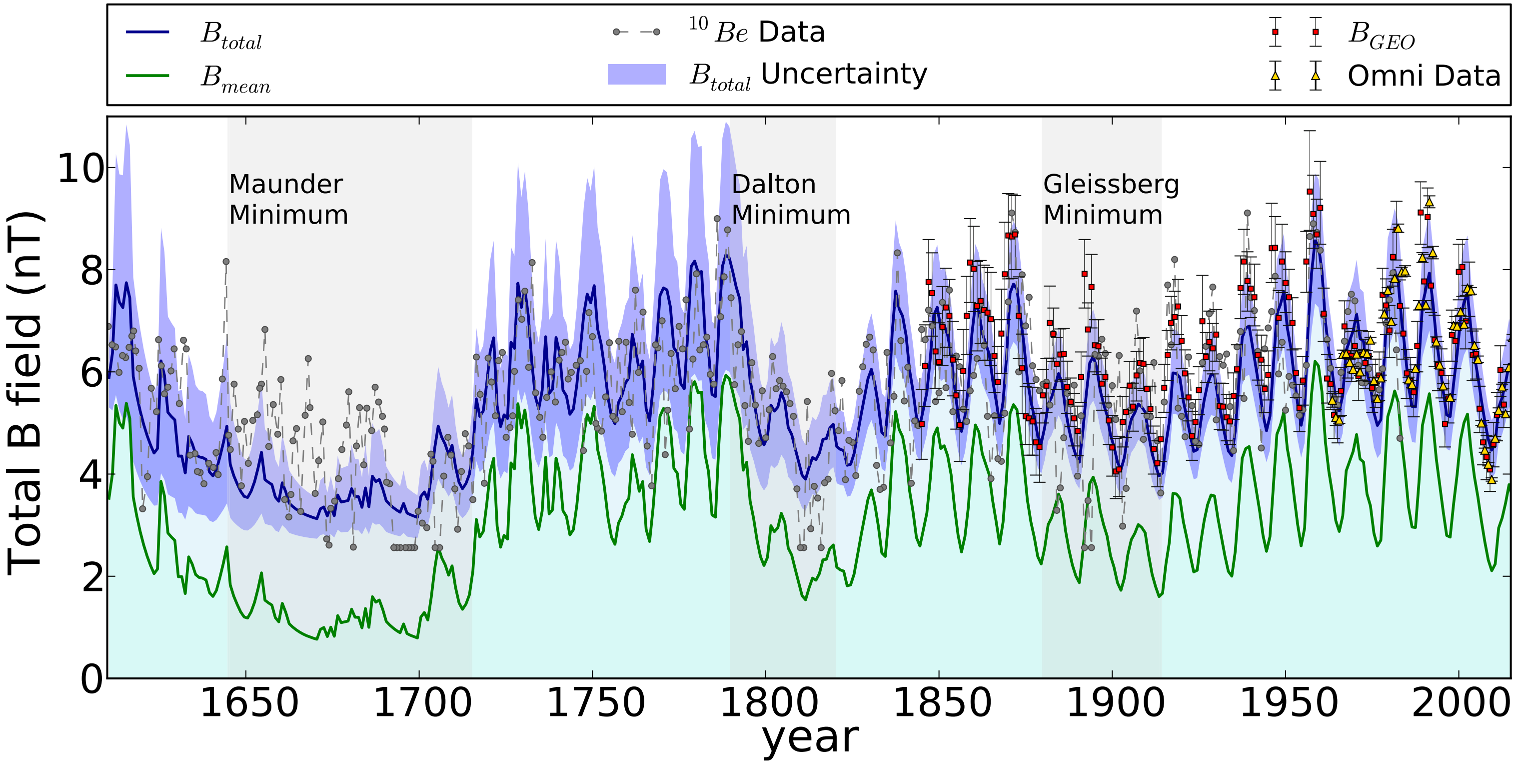

Figure 3.4 The simulated heliospheric mean field is shown in green. The simulated HMF (B_{total}) is shown in dark blue with 90% confidence interval uncertainty region (shown in blue), found by adding a constant toroidal field to the mean magnetic field. The HMF estimates based on ^{10}Be data are shown with grey circles, the reconstructed HMF based on geomagnetic data is shown in red squares with 90% confidence interval error bars and OMNI data points are shown with yellow triangles with 90% confidence interval error bars. I use geomagnetic-based data and OMNI data as the data points in chi-square analysis.

The 2.36 ± 0.05 nT added to the mean field was obtained by averaging over the deviation from the mean field in OMNI *in situ* measurements. However, this deviation (shown in Figure 5 as OMNI $B_{toroidal}$) shows a linear correlation with the mean field (or with CMEs, alternatively); previously noticed by a number of studies. Connick et al. (2009) reported a strong linear relation between open and toroidal flux density based on OMNI data although they found no evidence that changes in the toroidal flux had a significant contribution to the observed low magnetic field intensity in the recent prolonged minimum. Bieber and Rust (1995) estimated the net azimuthal flux per cycle as the source of overwinding imposed on the Parker field. Smith and Phillips (1997) investigated how CMEs lead to the overwinding of the HMF, analyzing disturbed and undisturbed solar wind data from ISEE3 concluding that the transient disturbances like CMEs upstream shocks can wind the HMF outside the Parker spiral (Parker, 1958). The increase in the toroidal field, as well as with other solar wind processes, might be associated with the portion of CMEs that open immediately after release (Owens et al., 2007). Near-Sun reconnection of the CMEs with open field lines can stimulate turbulent processes that cause the magnetic field to deviate from its spiral shape in the presence of disturbances in the solar wind.

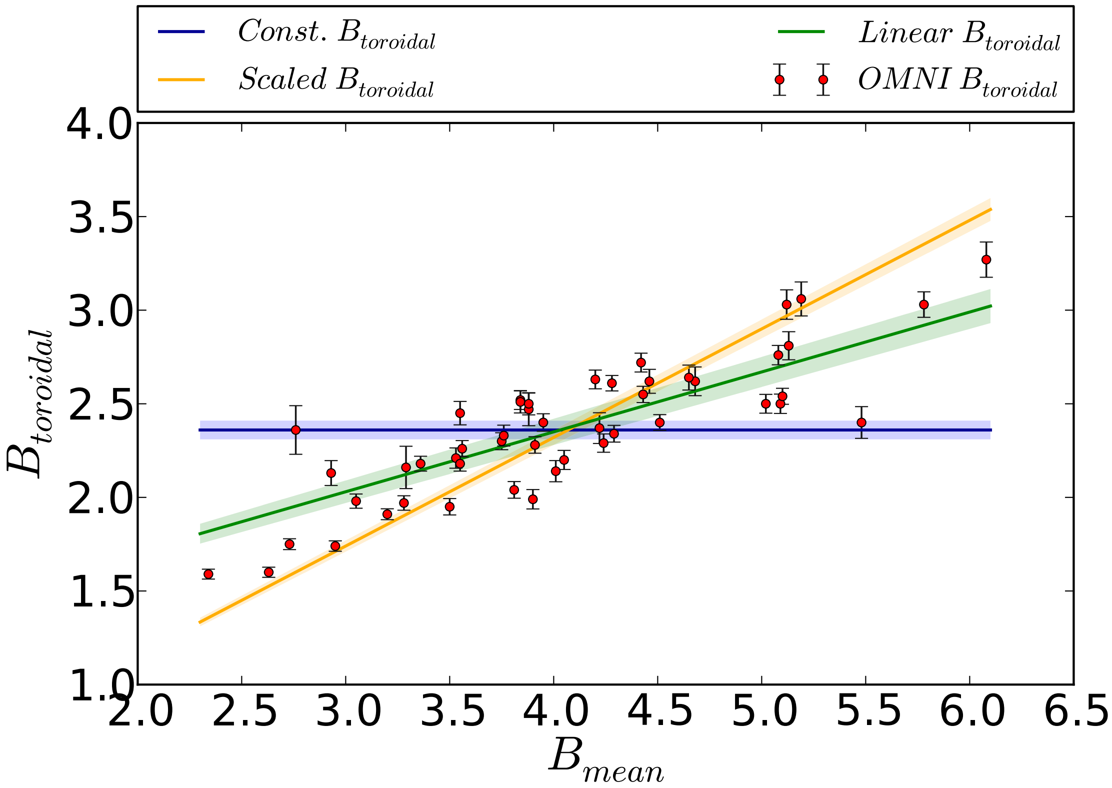

Figure 3.5 The constant toroidal field (dark blue line), obtained by averaging over the toroidal component from OMNI data (red circles with error bars), is compared to the toroidal field obtained by scaling to the mean field ($B_{toroidal} = (0.58 \pm 0.01) \times B_{mean}$, orange line) and finding a linear fit with nonzero intercept ($B_{toroidal} = (0.32 \pm 0.01) \times B_{mean} + 1.07 \pm 0.03$, green line).

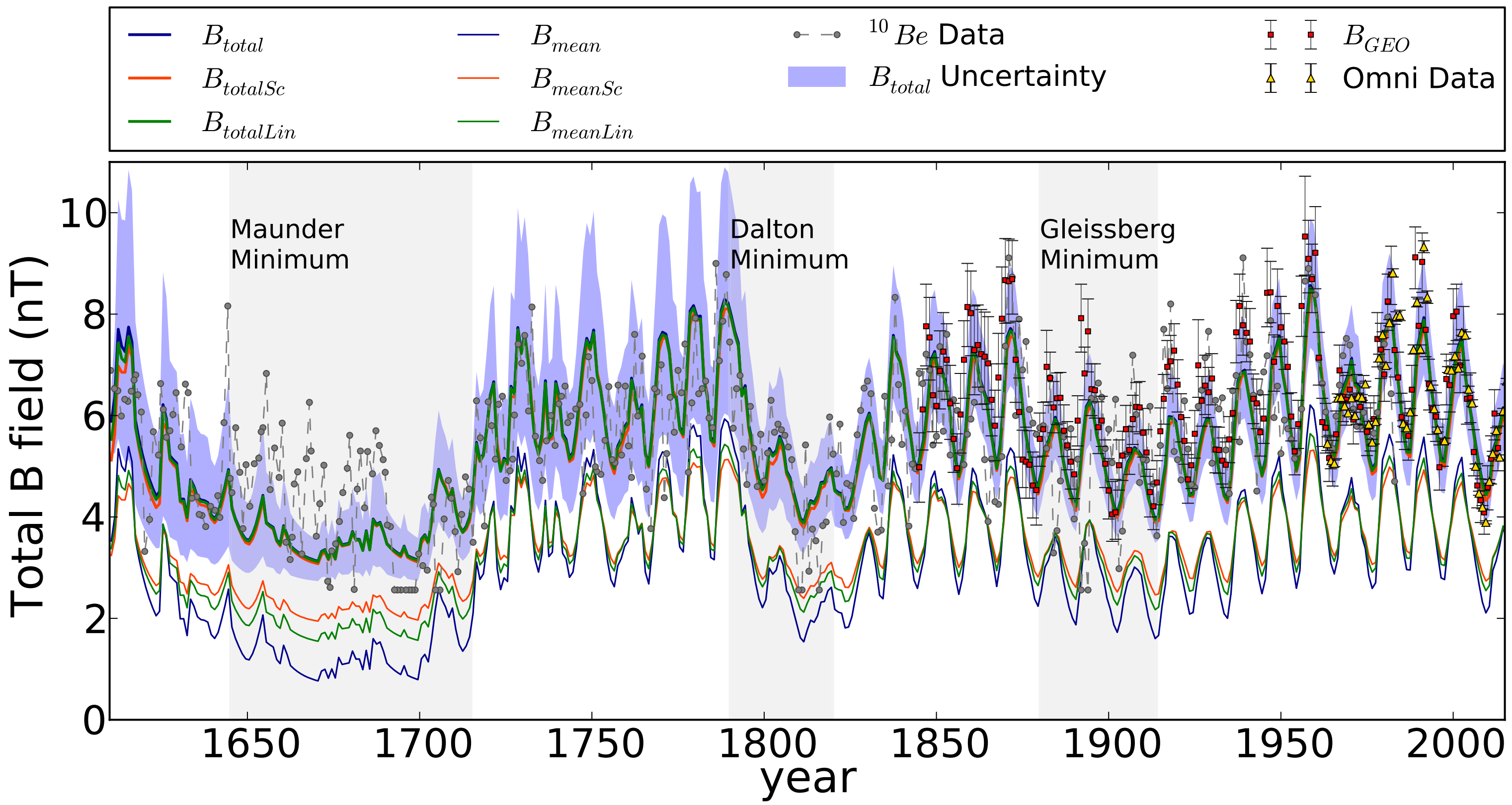

Figure 3.6 The simulated HMF (B_{total}) is shown in dark blue with 90% confidence interval uncertainty region (shown in blue), found by adding a constant toroidal field to the predicted mean field. The total field and mean field obtained by scaled (linear) toroidal component are shown in orange (green) lines. As can be seen the total fields show very good agreement between these cases although the mean fields demonstrate different levels of variability. The HMF estimates based on ^{10}Be data are shown with grey circles, the reconstructed HMF based on geomagnetic data is shown in red squares with 90% confidence interval error bars and OMNI data points are shown with yellow triangles with 90% confidence interval error bars.

I applied a chi-square analysis to find a linear relation between the toroidal component and the mean field from OMNI data once with zero intercept and once with nonzero intercept (Figure 3.5). The obtained toroidal fields are then applied to find the three timscale parameters and the floor flux that minimize chi-square, shown in Table 3.1. These results are interesting because the obtained timescale values, particularly for the case with a constant toroidal field, are remarkably close to those used in previous studies for example Smith et al. (2013) and Goelzer et al. (2013). The total fields obtained by applying a constant toroidal field (B_{total}, thick dark blue line), scaling the toroidal field to the mean field ($B_{totalSc}$, thick orange line), and deducing a linear relation between the toroidal and the mean field ($B_{totalLin}$, thick green line) are shown in Figure 3.6. Although the total fields are remarkably consistent, the mean fields show different levels of variability between these cases (thin dark blue, orange, and green lines in Figure 3.6). The chi-square analysis changes free parameters to obtain the best fit to the observational and reconstructed data (Table 3.1). The remarkable consistency between the total fields for these three cases shows that assuming a variant toroidal field decreases variations on the mean fields. As a result, three different sets of parameters were obtained without significantly changing the predicted total fields. Moreover, the fact that the reduced chi-square is minimized at ~ 0 to $(29.82 \pm 34) \times 10^{13}$ Wb floor flux, corresponding to ~ 0 to 1.49 nT magnetic field at 1 AU is suggesting that the evolution of the HMF can be modeled with a floor in the magnetic field limited to values ≤ 1.49 nT. The minimum value for the predicted HMF at 1 AU in the historic record obtained here is 3.13 ± 0.35 nT; showing that even in the deepest phases of the Maunder minimum the total magnetic field retains values higher than this, without requiring a floor field in the HMF any higher than 1.49 nT.

3.4 Discussion

It is beneficial to obtain the reduced χ^2 value for parameters used in Smith et al. (2013) and Goelzer et al. (2013) once using old yearly sunspot record and once using the newly released sunspot group number, in order to investigate the influence of the new sunspot record as well as comparing these model results with the results obtained in this study (3.1). In Section 3.3 I presented values for conversion, loss, and interchange reconnection timescales and the floor flux obtained by chi-square analysis, assuming the toroidal field to be constant or changing linearly with the mean field. Those results are shown in Table 3.1 along with the attributed reduced chi-square. The reduced chi-square is calculated using reconstructed magnetic field time series based on geomagnetic data and *in situ* measurements from OMNI. As can be seen in Table 3.1 the reduced χ^2 for the case where new sunspot group record is used is smaller than the case where an old sunspot record is used, suggesting a meaningful better match. Figure 3.7 compares the results from this study and the results of Smith et al. (2013) and Goelzer et al. (2013) (using the old and new sunspot numbers).

Table 3.1. Reduced χ^2 values and parameters found for cases investigated in this study using different toroidal field components and for the two cases with parameters from Smith et al. (2013) using the old and new sunspot numbers.

Method	$B_{toroidal}$	τ_c (years)	τ_l (years)	τ_{ic} (days)	ϕ_{flr} $\times 10^{13}$ Wb	$r\chi^2$
chi-square	2.36 ± 0.05	3.07 ± 0.03	5.91 ± 0.06	24.00 ± 0.18	zero	$24.32^{+31.24}_{+47.75}$
chi-square	$(0.58 \pm 0.01) \times B_{mean}$	2.12 ± 0.02	4.88 ± 0.04	12.97 ± 0.10	29.82 ± 0.34	$27.27^{+15.81}_{+59.63}$
chi-square	$(0.32 \pm 0.01) \times B_{mean} + 1.07 \pm 0.03$	3.05 ± 0.03	5.85 ± 0.06	17.89 ± 0.14	19.52 ± 0.41	$25.01^{+55.69}_{+30.68}$
Smith et al. (2013) (old SSN)	2.36 ± 0.05	2.5	6.0	20.0	No Floor	39.38
Smith et al. (2013) (new SSN)	2.36 ± 0.05	2.5	6.0	20.0	No Floor	27.23

The green line in Figure 3.7 shows the predicted field obtained by using CME rates scaled to sunspot numbers using $f = (\frac{8}{200}) \times (\textit{old sunspot number})$ and parameters used in Smith et al. (2013) and Goelzer et al. (2013). The purple line shows the predicted field obtained by using $f = (0.019 \pm 0.002) \times (\textit{new sunspot number}) + 0.37 \pm 0.13$ with the same parameters. The green line shows reasonable agreement with the OMNI data during the space age, in spite of the underestimation before the modern era (Compared to ^{10}Be-based data and geomagnetic-based data). As can be seen in this figure using the new sunspot record (purple line) improves the mentioned underestimation in the predicted field before the space age. My results from this work, assuming a constant 2.36 ± 0.05 nT toroidal field, is shown with blue line.

Figure 3.7 shows that the total HMF for the case investigated in this study (blue line) is relatively consistent with the case where I used new sunspot numbers with parameters from Smith et al. (2013), except for more pronounced maximum values in my case. This makes sense since the higher value for the interchange reconnection timescale (used in this study) reinforces an increase in the strength of HMF during solar maxima. Additionally, the notable discrepancy in the solar maxima between the green line (using old sunspot record) and purple and blue lines (using new sunspot record) after 1947 is attributed to a correction in all sunspot numbers after that date as is explained in Appendix B.

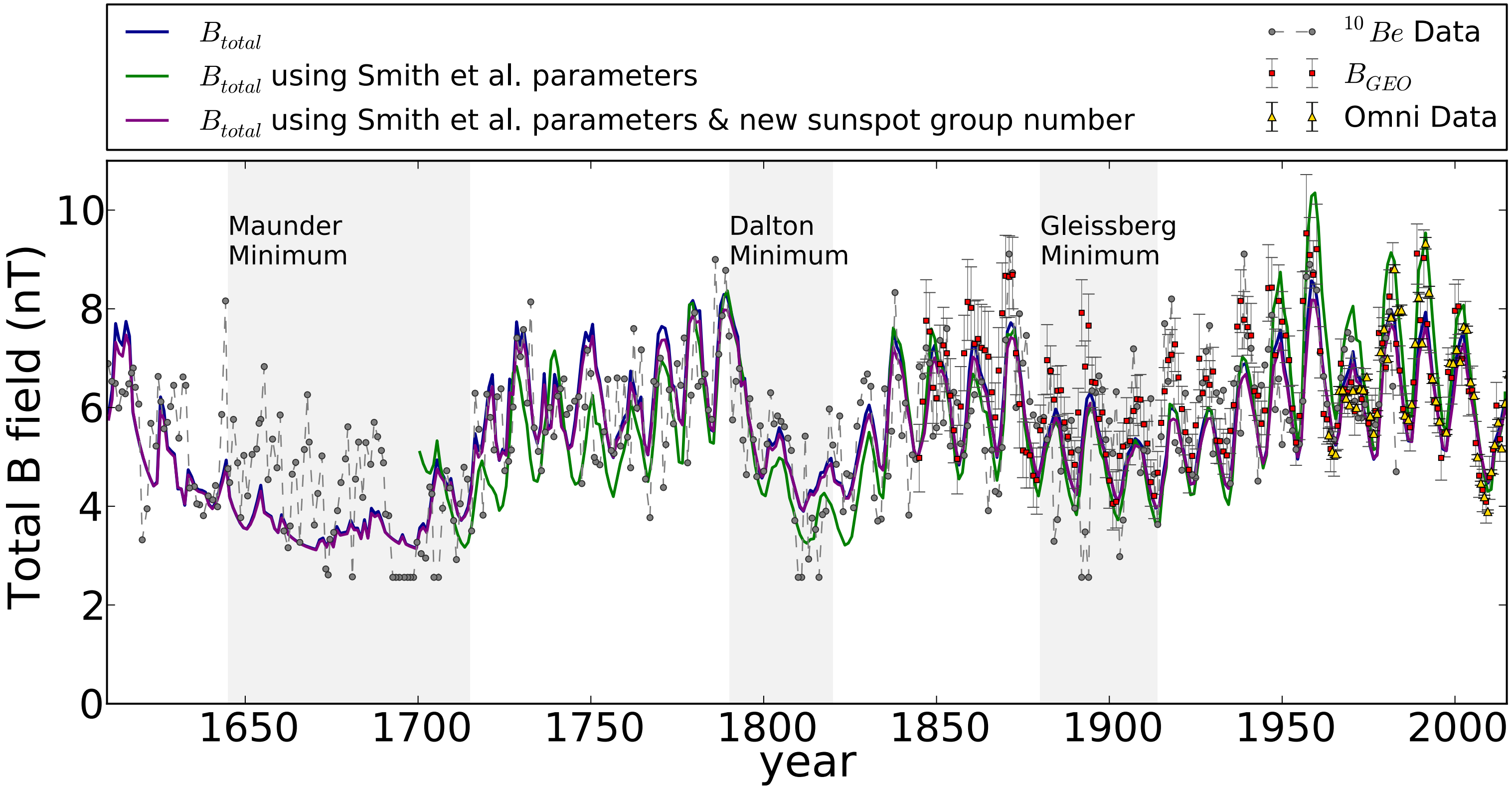

Figure 3.7 The simulated HMF using parameters found in this study (blue) is compared to the simulated HMF obtained by parameters used in Smith et al. (2013) and Goelzer et al. (2013), shown in green (purple) using old (new) sunspot number. The error bars used for geomagnetic data and OMNI data show 90% confidence interval.

I have shown that there is reasonable agreement between the predicted HMF based on the Schwadron et al. (2010b) model (Section 3.2.2) and the reconstructed data (based on the cosmogenic ^{10}Be and geomagnetic data) and observational data (OMNI data). However, Figure 3.4 shows that the magnitude of the variability of the HMF strength in the ^{10}Be data is greater than that of the model calculations (and geomagnetic-based data). As discussed below, this is likely due to statistical variability and systematic deviations in the cosmogenic data. Note also that the variability of the predicted field is less pronounced and is accompanied by underestimation of the strength of the HMF during the Maunder Minimum. In the case of the sunspot number, there are up to a factor of two uncertainties prior to 1870 (Figure 4 of Owens et al. 2016), which will introduce uncertainties of the same magnitude into the model estimates that may be responsible for the underestimates during the Grand Minima. The algorithm relating the CME rate to the sunspot number can be a source of the discrepancy between the model and reconstructed ^{10}Be-based data. Moreover, the flux excess (reported by Owens et al. 2008 and investigated by Lockwood et al. 2009 and Owens et al. 2013) created by the inversions of HMF can be a source of overestimation of the observed data at 1 AU. All these uncertainties are discussed further below.

Uncertainty 1. ^{10}Be**:** Experimental data show the standard error of annual estimates of the ^{10}Be concentration in polar ice-cores is $\sim 20\%$ McCracken and Beer (2015). There are numerous causes for this variability other than the time-dependent production rate: fluctuations in the small number of ^{10}Be atoms in each annual sample; latitudinal and temporal variations in the terrestrial magnetic field; and climate influences that affect transport, deposition, and sequestration. Heikkilä et al. (2013) have stressed that seasonal variations in fluxes and dating uncertainty can lead to spurious peaks in the ^{10}Be ice core records. More recently, McCracken and Beer (2015) have demonstrated that the energetic particles generated in large solar flares and CME-driven shocks have resulted in $1-2$ nT underestimates in the HMF field strength in the vicinity of some sunspot maxima.

While general agreement between ^{10}Be measurements from Greenland and Antarctic cores has been established (e.g., Caballero-Lopez et al. 2004; McCracken et al. 2004; Usoskin et al. 2003), there are undoubtedly both long- and short-term effects due to meteorological and climatic differences that may not be in-phase within a hemisphere, or between the two hemispheres. To minimize such long- term effects, Steinhilber et al. (2012) used principal component analysis to determine the cosmic-ray production signal. McCracken and Beer (2015) used that production signal to minimize the long-term (> 22 year) climate and other system effects in the estimates of the HMF that I have used. To gauge the effectiveness of this procedure, Figure 3.8 shows a comparison between the variability of ^{10}Be measurements in Greenland used in this study ($\sim$ 1 year averages of Dye3 and NGRIP corrected for climate change) (McCracken and Beer, 2015) and measurements from Antarctica ($\sim$ 8 year resolution from South Pole) (Bard et al., 1997). These measurements show consistency in the secular variability, particularly during the Maunder Minimum. However, discrepancies associated with individual peaks could indicate global and regional climate influences or local meteorological effects.

The underestimate of the model compared to the observational results is most pronounced in the first half of the Maunder Minimum, 1645-1680. This could be the consequence of similar climate effects in all four of the cores used by Steinhilber et al. (2012), possibly resulting in higher observational estimates for the strength of the HMF. The lack of short-term model variability compared to observational results during the Maunder Minimum may result from climate impacts, such as changes in the North Atlantic Oscillation (NAO) climate mode that influences the rates of snow accumulation over parts of Greenland. For example an increase in the snow accumulation would cause a decrease in ^{10}Be concentration, resulting in higher values of HMF. As higher resolution ^{10}Be datasets become available from Antarctic ice cores, it will become possible to determine the source of discrepancies between model and ^{10}Be-based estimates of HMF on Schwabe cycle timescales. Combining paleoclimate records of ^{10}Be and other cosmogenic radionuclides (e.g., ^{36}Cl and ^{26}Al from ice cores and ^{14}C from tree rings) and comparing records from the Arctic and Antarctica can also help distinguish

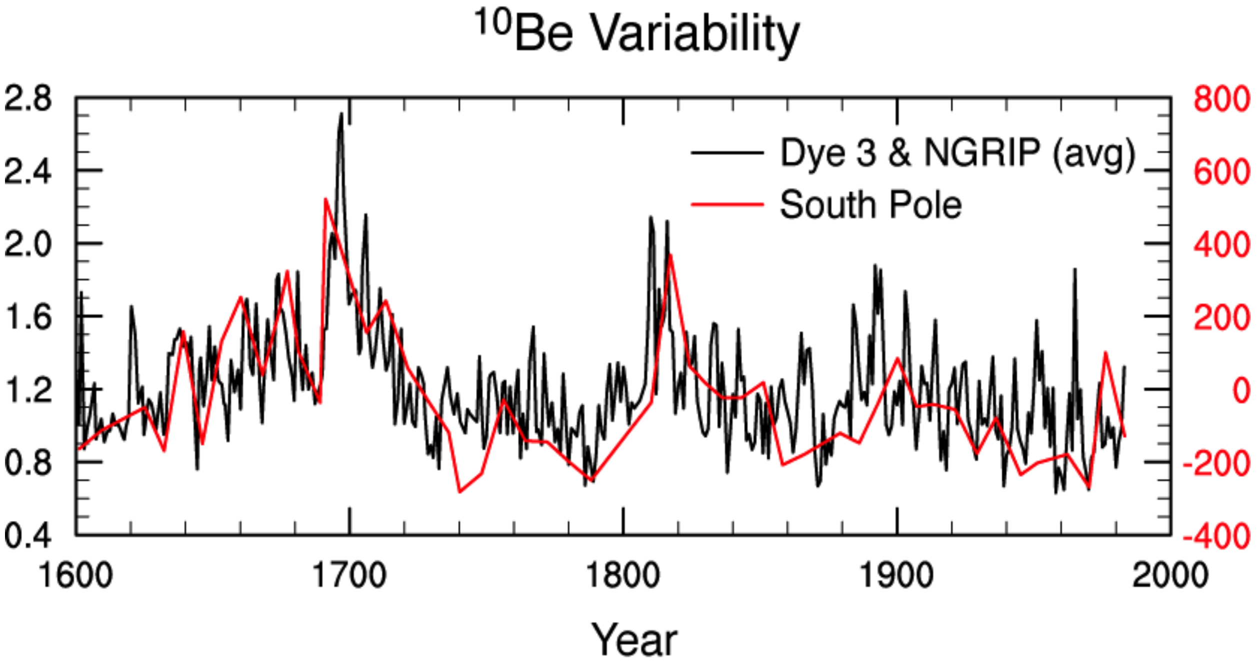

Figure 3.8 Black lines represent the ratio between the average of the Dye 3 and North GRIP ^{10}Be concentrations (adjusted to remove long-term climate effects) and the average for the interval 1944-1987 from Steinhilber et al. (2012) (McCracken and Beer, 2015). Red lines represent variations from the mean (in parts per million) using $\sin 8$ year resolution measurements of ^{10}Be from the South Pole core (Bard et al., 1997).

the cosmic ray production signals from climate effects.

Uncertainty 2. The sunspot record: There is an ongoing debate on sunspot records and methods to reconstruct them from original sources (Lockwood et al., 2016; Owens et al., 2016). The low sunspot number during the Maunder period has been controversial. In a recent paper, Vaquero et al. (2015) generated a database of reliable sunspot observation around the Maunder minimum (1637-1715). However, in this work, I needed to use a data set that covers the Maunder period and persists to the present day so it can be compared to CME rate data. The sunspot record (new sunspot group number released by SILSO) that I used in this study meets both these criteria. The method based on Svalgaard and Schatten (2016) backboning is discussed at length in Appendix B. The sunspot group number is corrected to remove the discrepancy between sunspot number and sunspot group number before 1850, which leads to more pronounced group numbers for the Maunder period. However, Lockwood et al. (2016) have shown that the backboning method results in an accumulative overestimation of the sunspot group numbers going back in time. Therefore, a comparison between sunspot group numbers and their effect on the modeled HMF may need to be revisited in future work.

Uncertainty 3. Obtaining the CME rate from Sunspot numbers: I applied chi-square to find a linear relationship (Equation 3.5) to derive CME rates from sunspot numbers. The uncertainties associated with the slope and intercept of this linear relationship are calculated using Equation 3.9. The CME rates used in this study are corrected to remove the effect of the LASCO image cadence after August 2010 as suggested by Wang and Colaninno (2014). The uncertainty shown as the blue shaded area in Figure 3.2 is attributed to both sunspot number uncertainties and the uncertainties of the linear relationship and is the major source of uncertainty of the predicted HMF shown in Figure 3.4 in blue shaded area. However, there are other sources of uncertainty such as the uncertainty of the toroidal field and the uncertainty of the timescales obtained by Equation 3.9. Another potential source of uncertainty is the assumption that almost half of CMEs open immediately after release (D = 0.5).

Uncertainty 4. Inverted HMF: Owens et al. (2008) reported the flux excess that increases with heliospheric radial distance. It was investigated in two subsequent papers (Lockwood et al., 2009), which attributed it to kinematic effects noting that the seed for such effects can be interchange reconnection in the corona. Owens et al. (2013) showed that the inverted HMF, created by interchange reconnection beneath the source surface (as shown in Figure 3.9), can cause a magnetic flux excess in 1 AU *in situ* observations. They showed that such inversions in the HMF will become aligned, on average, with the Parker spiral. Therefore, the decomposition of the HMF into a mean field and non-Parker component does not remove the influence of HMF inversions. However, averaging the radial field over 1 day intervals may indirectly address the issue since HMF inversions appear in clusters over intervals smaller than one day. Owens et al. (2013) used an automated data analysis method

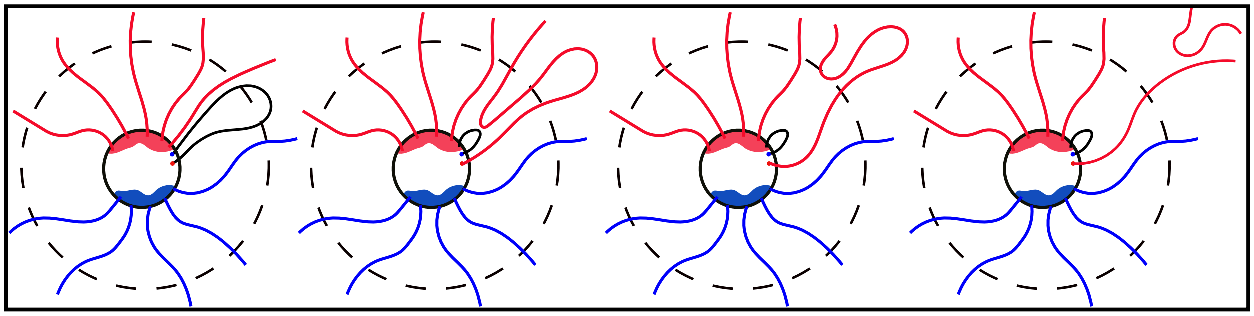

Figure 3.9 HMF inversions can be created when the switched-back field segment is dragged out beyond the Alfvén surface by the solar wind after magnetic reconnection occurs between an open field line and a closed field line within a CME or a part of a flux rope (Owens et al., 2013).

and found that HMF inversions can cause an overestimation of *in situ* measured field no greater than 10% of the observed values for the field. This effect can be an important source for the discrepancy observed between my model results and *in situ* measurements of HMF.

3.5 Summary and Conclusion

In this study I employed the theory of Schwadron et al. (2010b) (Section 3.2.2) to model the generation of HMF back to 1610 using the new release of the sunspot group number by SILSO. This model describes the evolution of the heliospheric magnetic flux including the closed flux from CMEs and the balance provided by conversion, loss and interchange reconnection of magnetic flux. Smith et al. (2013) and Goelzer et al. (2013) had previously used the same method using the same fixed parameters accounting for the timescales associated with conversion, loss and interchange reconnection of the magnetic flux back to 1963 and 1749. I took a step further by employing a chi-square analysis method to find the set of parameters that yields the closest agreement between the predicted results from my model and reconstructed geomagnetic-based HMF and observed OMNI data.

I found that the following parameters minimize the chi-square: $\tau_c = 3.07 \pm 0.03$ years, $\tau_l = 5.91 \pm 0.06$ years, and $\tau_{ic} = 24.00 \pm 0.18$ days, and $\phi_{flr} = (-0.19 \pm 0.54) \times 10^{13}$ Wb, which is statistically consistent with zero, assuming a constant toroidal field of $2.36 \pm$

0.05 nT (parameters obtained by assuming a variant toroidal field are shown in Table 3.1). In this study I obtained single values for the timescales and the floor flux over centuries, although these values might change locally over solar cycles. For example, the reduction in the interplanetary magnetic field that we saw in the transition of cycle 23 - 24 indicates that some decrease in the loss timescale may occur locally, potentially driven by large changes in solar wind parameters (e.g., reductions in solar wind density and flux).

I investigated results based on the sunspot number data set, scaling factor, and timescale parameters used in Smith et al. (2013) and Goelzer et al. (2013), presented both in Table 3.1 and Figure 3.7. As can be seen in Figure 3.7, the results from Smith et al. (2013) and Goelzer et al. (2013) show a remarkable agreement with the observational and reconstructed HMF data during the space age, in spite of a significant underestimation of the field prior to it. Using the SILSO new release of sunspot group numbers for their case compensates some of the underestimation of the field before the modern era. Reduced chi-square values in Table 3.1 and Figure 3.7 show a better agreement between model results in this work and reconstructed HMF data (geomagnetic-based) and observational data (OMNI).

My results suggest a floor ≤ 1.49 nT is required in order to successfully model the HMF even during the least active phases of the sun. Besideds this evidently small floor, the heliomagnetic field is kept from decaying drastically at grand minima (namely the Maunder period) by the hysteresis associated with the large disconnection or loss timescale ($\sim 6-10$ years) for ambient heliospheric magnetic flux. This hysteresis causes the field to rise sharply with the increase of sunspot numbers, but to fall slowly in the transition toward solar minima. This predicted hysteresis also finds support in the conclusion by McCracken and Beer (2014) that the mean HMF decreased in an approximately monotonic manner over the first five Schwabe cycles at the commencements of both the Maunder and Spoerer Minima, followed by rapid recoveries at the ends of those Grand Minima.

Furthermore, I briefly investigated the possible sources for the discrepancy between the predicted HMF and the observed and reconstructed data in Section 3.4. The possible sources include (1) climate variability, the production of energetic particles by solar events, and variability in ^{10}Be-based data; (2) the uncertainty of the sunspot numbers during the Maunder Minimum; (3) variability in CME rate deduced from sunspot number; (4) the magnetic flux excess attributed to inverted HMF.

Thus I incorporated the recently derived Long-term Solar Observations SILSO with the Schwadron et al. (2010b) field model (Section 3.2.2) to elucidate how the HMF evolved back through the Maunder Minimum. The results show HMF evolution during periods of extremely low activity. These results may be important in the context of the recent extended minimum of cycle 23 - 24 and the extremely small maximum of cycle 24, both indicative of unusually low solar activity that may persist in coming years.

As a result, we have observed the highest fluxes of galactic cosmic rays (GCRs) in the space age, and relatively few solar energetic particle (SEP) events. In the next two chapters (Study 2), we investigate the deep space radiation environment resulting from the unprecedented decline reported in the strength of solar cycles. In Chapter 4 we review concepts associated with the radiation environment and investigate the expectation of fewer occurrences of SEP events through the current phase of low solar activity. We investigate the radiation effects from the SEP event of September 2017 and show that after a long paucity of solar activity, this event was a caution for the possible hazard. This work is a part of a more inclusive study published in Space Weather [Schwadron2018]. In Chapter 5 we investigate the effect of GCRs on the space radiation environment. We apply past secular minima conditions to the coming solar cycle to find extreme scenarios for a modern secular minimum and the resulting radiation environment. This work will be submitted for publication in Space Weather in the near future.

CHAPTER 4

An Example of Radiation Risk from Solar Energetic Particles, September 2017 Event (Study 2)

4.1 Intorduction

Galactic cosmic rays (GCRs) and solar energetic particles (SEPs) comprise most of deep space radiation environment and challenge the success of human space missions beyond the magnetic shielding of the Earth. Solar flares and Shock waves, driven by coronal mass ejections (CMEs), can produce SEPs. As a result, SEP events are highly sporadic and difficult to predict. SEPs are associated with short-term or acute radiation effects ranging from fatigue and sickness to in-flight death (Cucinotta et al., 2015). Predictions of Radiation from REleASE, EMMREM, and Data Incorporating the CRaTER, COSTEP, and other SEP measurements (PREDICCS) http://prediccs.sr.unh.edu is an online system that provides a reliable near-real-time probability of SEPs (Schwadron et al., 2012; Joyce et al., 2013; Quinn et al., 2017).

GCRs are energetic charged particles, likely accelerated in supernova explosions. They consist of protons, heavier ions and a small fraction of electrons. Most of these ions are filtered at the interface between the heliosphere and the interstellar medium. The remaining ions enter the heliosphere at a constant rate, although, since they are controlled by the heliospheric magnetic field (HMF) (Parker, 1965; Jokipii, 1991), solar cycles affect their flux in the inner heliosphere. GCRs are typically much more energetic and thus more penetrating than SEPs. However, they are much lower in fluxes, hence need more time to build doses. As a result, they are associated with long-term effects that pose a threat for the space mission crew, particularly in long space missions (for example Cucinotta et al., 2001; Schwadron et al., 2014). In this chapter, I briefly investigate the SEP event of the September 2017, reporting results from Schwadron et al. (2018). In chapter 5, our main focus will be on radiation from the GCRs and their long-term effects.

In order to design exploration missions in the inner heliosphere, both short-term and long-term effects of the radiation have been investigated [for example Cucinotta et al. (2001); Cucinotta and Durante (2006); Durante and Cucinotta (2008); Cucinotta et al. (2010); Cucinotta (2014); Cucinotta et al. (2015); NRC (2008, 2012, etc.). Ground radiation limits for radiation workers were the base for NCRP (2000) recommendations for excessive 3% cancer fatality risk dose limits. These limits are calculated based on effective dose, which accounts for tissue weightings. 1 Sv effective dose is defined as the weighted equivalent of 1 J of radiation energy absorbed by 1 kg of tissue. Based on a 3% risk of exposure-induced death (REID), NRC (2008) established the dose limits: 620 mSv limit for a 30-year old male and 470 mSv limit for a 30-year old female. The 3% REID accounts for the deaths shifted to earlier ages due to radiation exposure, which is more limiting than the excess risk of cancer fatality. These dose limits were implemented by Schwadron et al. (2014) to obtain allowable days for mission durations in the coming solar cycles.

However, these exposure limits are subject to uncertainties mainly due to extrapolating cancer risk data from high to low dose rates, transferring risk across different populations, uncertainties in epidemiology data, and most importantly, the lack of knowledge on risks from heavy ions and secondary radiation in space (Cucinotta et al., 2010). Therefore, NASA permissible exposure limits (PELs) based on NCRP recommendations (NCRP, 2000) and 3% REID (NRC, 2008) must be implemented with an upper bound of 95% confidence level. The Human Integration Design Handbook [2014] applied the 95% confidence level and reported effective dose limits for a 1-year mission for male and female astronauts (See National Aeronautics and Space Administration, 2014, table 6.8-5).

4.2 Cosmic Ray Telescope for the Effects of Radiation

The Cosmic Ray Telescope for the Effects of Radiation (CRaTER) (Spence et al., 2010), on board of the Lunar Reconnaissance Orbiter (LRO) (Tooley et al., 2010), aims to investigate the lunar radiation environment. CRaTER consists of three pairs of silicon detectors, each pair including one thin (odd-numbered) and one thick (even-numbered) detector, labeled D1 through D6 (Spence et al., 2010) (Figure 4.1). Two pieces of tissue equivalent plastic (TEP) are located between these pairs of detectors. All these components are stacked along an axis perpendicular to the lunar surface, with the first pair of detectors (D1-D2) facing zenith, and the third pair (D5-D6), facing nadir.

When CRaTER is in its typical orientation, energetic particles originating from the zenith pass through (1) 0.81 mm(0.22 g/cm^2) Al endcap, (2) D1-D2 detectors, (3) tissue-equivalent plastic (TEP) of thickness 54 mm (6.09 g/cm^2), (4) D3-D4 detectors, (5) 27 mm (3.04 g/cm^2) TEP, (6) D5-D6 detectors, and (7) 0.81 mm (0.22 g/cm^2) Al endcap. Further details on CRaTER can be found in (Spence et al., 2010). Significant energy loss occurs within the TEP. Therefore, D3-D4 are the most shielded detectors within the instrument.

The energy loss within the TEP allows us to differentiate between particles coming from the Moon and GCRs from deep space at energies below a few hundred MeV/nuc. As a particle traverses the detector stack, it loses energy, primarily within the TEP. Lower-energy particles deposit more energy in a detector than higher-energy particles. As a result, a coincident event that is registered in both D4 and D6 (both thick detectors) typically deposits a greater amount of energy in D4 than in D6 if it originates from the direction of the Moon. Conversely, if the particle originates from deep space, it will deposit a greater amount of energy in D6 than in D4, although at high energies, signals in the two detectors are indistinguishable.

The CRaTER microdosimeter is behind about ~ 4.4 g/cm^2 equivalent aluminum, which shields against protons below ~ 55 MeV. Mazur et al. (2011) discussed the first 6 months of mission data from the microdosimeter, and Mazur et al. (2015) updated the microdosimeter data from the start of the LRO mission through the end of 2014.

Silicon detectors measure deposited energy of incident energetic particles above 7 keV. The deposited energy divided by the path length of the incident particles is the Linear Energy Transfer (LET). CRaTER is designed to cover the full range of LET expected by the SEPs and GCRs: there is an overlap between the detectable LET ranges in each detector pair, which is corrected by taking the deposited energy in the thin detector as the contributor. For the purpose this chapter, we project the dose rates (observed at mean altitude h) to the lunar surface by multiplying it with a correction factor $\frac{1}{1+\sqrt{1-(\frac{R_m}{R_m+h})^2}}$, which accounts for the changing solid angle blocked by the Moon (R_m is the lunar radius). Furthermore, we correct for the difference in energy deposition in water/tissue versus silicon, using a multiplicative factor of 1.33. For a thorough discussion on calculation of the dose rates and correction factors see Schwadron et al. (2012).

4.3 The SEP Hazard During Periods of Weak Activity

Schwadron et al. (2014) studied the probability of SEP events using PREDICCS (Schwadron et al., 2012). They found that the probability of reaching the 30 day blood-forming organ dose limit of 25 cGy-equivalent behind 10 g/cm^2 aluminum shielding was insignificant over timescales of 30 days to 1 year (NRC, 2008).

While the cycle 24 conditions indicate a low probability for an extreme event, the recent 10 September 2017 SEP event demonstrates that large events can arise with little warning. Figure 4.2 shows the dose rates in the D1-D2, D3-D4, and D5-D6 detectors and CRaTER microdosimeter; the $>$ 1.5 year lull in activity in 2016-2017 is obvious. The September 2017 event was one of the largest of the CRaTER mission and was rivaled only by the March 13 2012 SEP event in terms of the most shielded D3-D4 and microdosimeter dose rates.

The September 2017 event had an unusually hard spectrum, with large fluxes above 400MeV, and large dose rates in the most shielded CRaTER detectors. Figure 4.3 shows the accumulated dose during the event as a function of location and shielding in the CRaTER detector stack accumulated during the event along with the PREDICCS doses modeled through the event into 1 g/cm^2 H2O, a proxy for a lens or skin dose.

In Figure 4.3, I combined CRaTER observations (yellow triangles) with data from PREDICCS (red points). The blue line and shaded uncertainty region represents a power law fit to the PREDICCS data. The functional form of accumulated dose versus shielding plotted in Figure 4.3 allows us to estimate the effective shielding (in g/cm^2) for each of the CRaTER detector pairs. The shielding estimates are roughly consistent with the average shielding provided by the TEP, endcaps, and the side-shielding that encircles all six detectors. These effective shielding depths will be useful in estimating the effects of shielding and the attenuation of dose within materials of varying thickness. These CRaTER shielding estimates for detector pairs are roughly consistent with the shielding associated with the TEP and endcaps. However, radiation penetrates CRaTER from all directions not blocked by the Moon. For example, the endcap provides 0.22 g/cm^2 Al shielding. However, we find effective D1-D2 shielding of 0.37 ± 0.02 g/cm^2, which is in excess of the endcap shielding due to extra mass around the detector pair and increased shielding from side-penetrating radiation.

An important question is the degree to which the September 2017 event could have significant health effects for astronauts. We find from Figure 4.3 that the lens and skin dose on the lunar surface would approach the 30 day limits (100 cGy skin dose and 150 cGy lens dose) (Cucinotta et al., 2010; NRC, 2008; NCRP, 2000). However, even moderate shielding (> 1 g/cm^2 Al shielding) would reduce the radiation dose below these limits. A question is whether the dose would approach radiation limits during an extravehicular activity, typically lasting $\sim$ 3 hours. At the peak skin/lens dose rate of 5.8 ± 0.3 cGy/h behind 0.3 g/cm^2 Al shielding, an astronaut would collect 17.4 ± 0.9 cGy dose within 3 hours, which is significantly lower than lens/skin dose limits. This dose and dose rate would be approximately doubled in free space, also below the 30 day limits. Both the accumulated doses during the September 2017 event and the maximum dose rate are significantly smaller than those in extreme SEP events, such as the August 1972 event. For example, the skin dose and maximum skin dose rate behind thin shielding (Al 0.3 g/cm^2) during the August 1972 event was 3215 cGy and 980.90 cGy/h (Hu et al., 2009), more than a decade larger than observed in the September 2017 event.

The precise biological effects of SEP radiation remains an area of active research (e.g. Cucinotta and Durante, 2006; Cucinotta et al., 2010; Schwadron et al., 2014). It is clear that the September 2017 event is dangerous, with doses that are large but not conspicuously above limits defined by the radiation biology community. An event of this kind represents an example in which astronauts would ideally be located behind the safety of spacecraft shielding. As such, advance warning for such events remains an imperative.

The detailed evolution of the SEP events in September 2017 are shown in Figure 4.4. These include two X-class flares that started each of the major events on 6 and 10 September. Note that the multiple eruptions of the same active region at the Sun created an energetic particle seed population that was subsequently accelerated in the 10 September event, similar to twin-CME scenarios studied by Li et al. (2012) and Lugaz et al. (2017).

4.4 Conclusion

I conclude this chapter by noting that the accumulated dose in the September 2017 SEP event approached 30-day limits for low shielding thickness. The analysis demonstrates that the hard spectrum substantiated a radiation hazard. The fact that the event arose during a period of relatively quiet solar activity, while not uncommon for the declining phase, suggests that these events may be difficult to predict. September 2017 event sets an example of the hazard caused by isolated SEP events, besides the high GCR radiation risk through the current phase of low solar activity. In Chapter 5, we investigate the possibility of a worsening radiation environment associated with high fluxes of the GCRs assuming that the present decline in the solar activity will persist and worsen in the coming years. We calculate time series for the dose rates and permissible mission durations (PMDs) for a Dalton-like and a Gleissberg-like solar cycle 25. This work will be submitted for publication in Space

Weather in the near future.

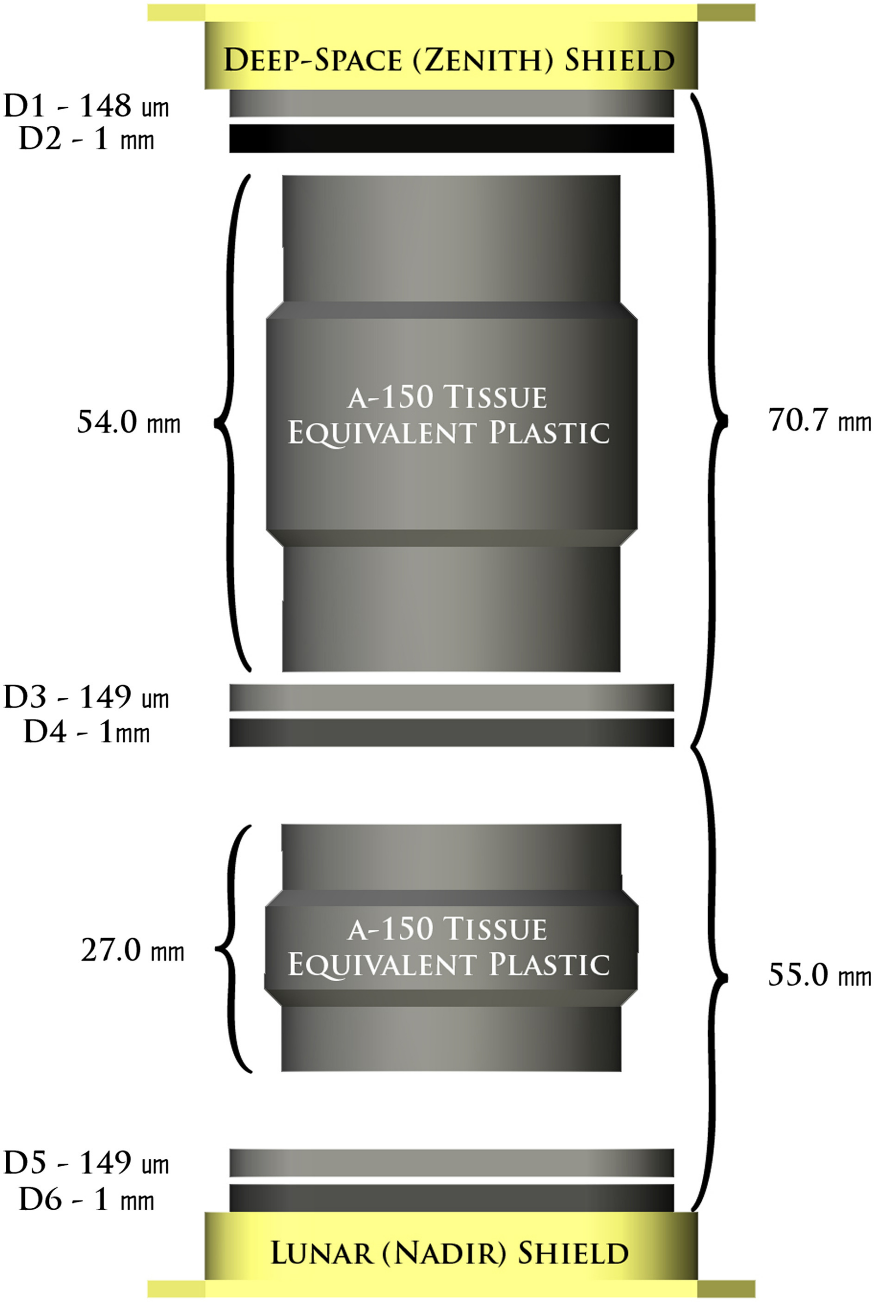

Figure 4.1 The Cosmic Ray Telescope for the Effects of Radiation instrument consists of a stack of three pairs of thin and thick silicon detectors separated by tissue-equivalent plastic. Shown here is the configuration of these detectors with D1-D2 facing zenith and D5-D6 facing in the nadir direction.

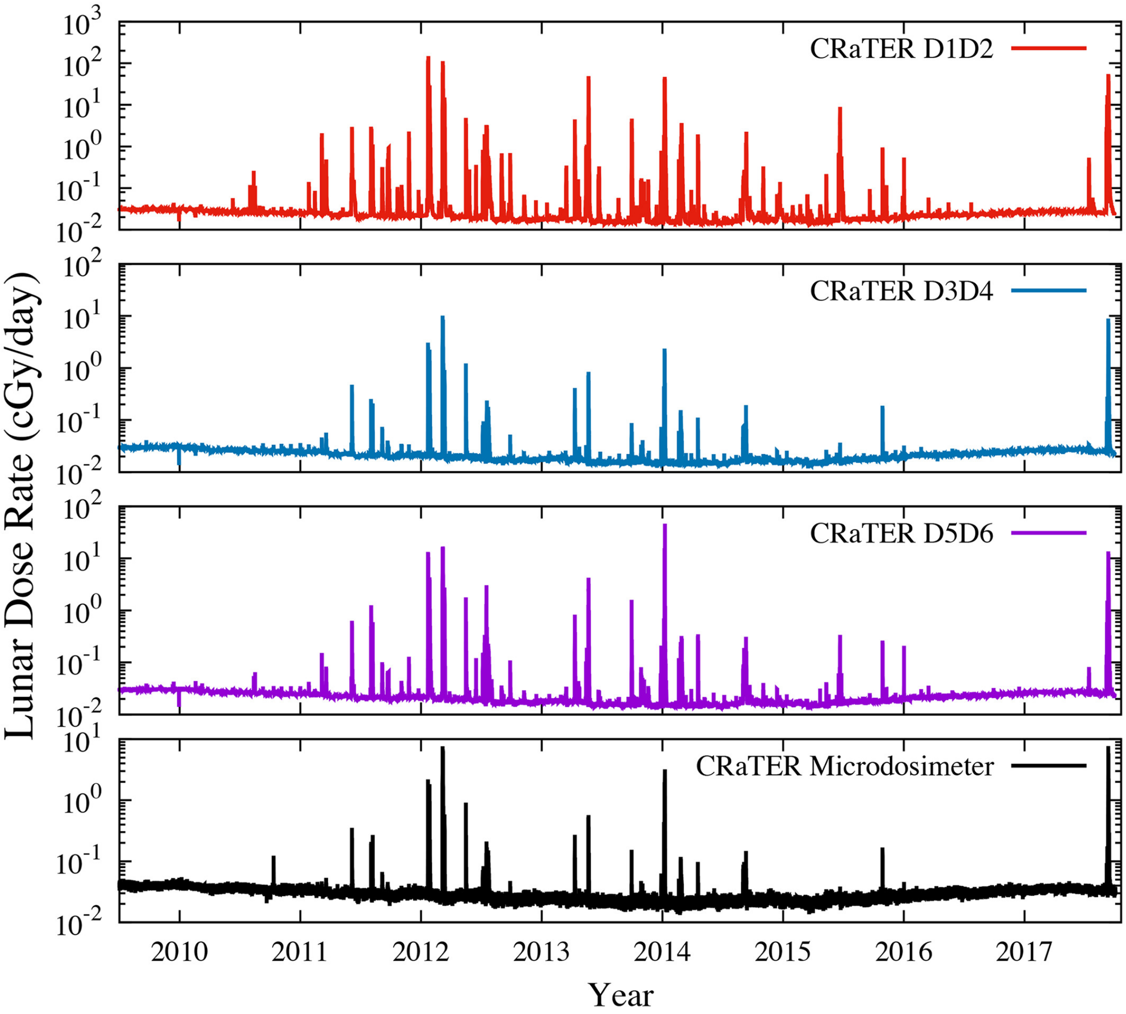

Figure 4.2 Dose rates in the three thin-thick detector pairs (D1-D2, D3-D4, and D5-D6) and the microdosimeter within the Cosmic Ray Telescope for the Effects of Radiation (CRaTER). All dose rates have been geometrically corrected for exposure on the lunar surface and corrected for doses in H2O as opposed to Si (Schwadron et al., 2012).

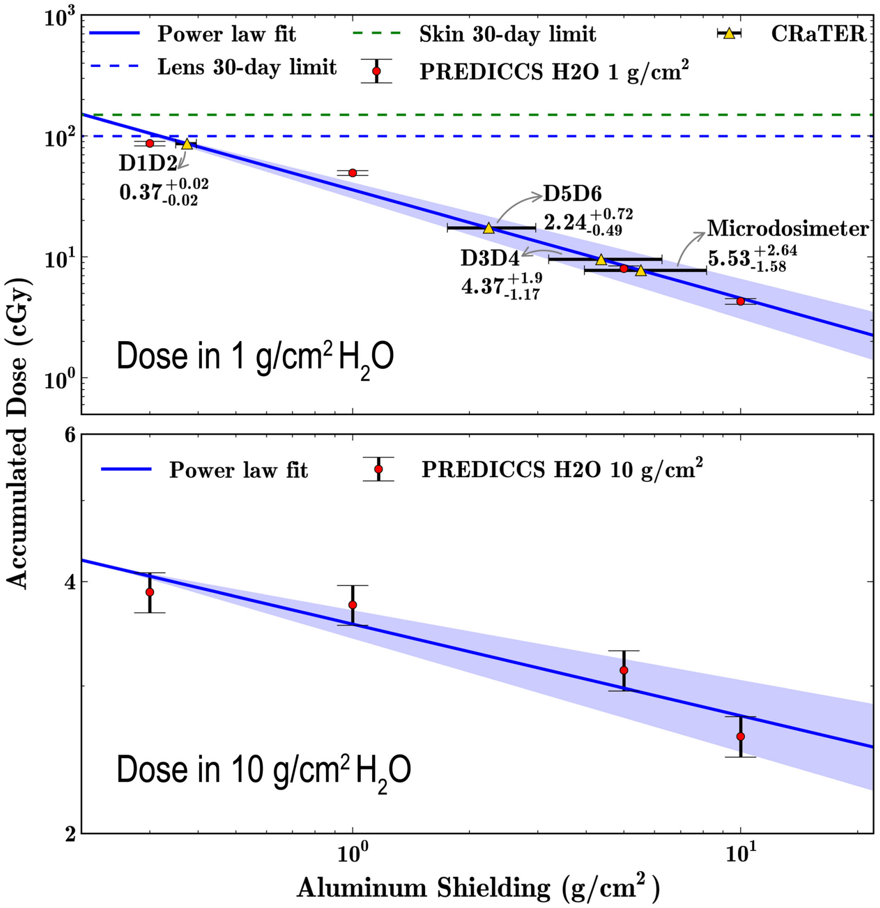

Figure 4.3 Accumulated doses on the lunar surface during the September 2017 solar energetic particle event behind different amounts of Al shielding. Red data points show Predictions of Radiation from REleASE, EMMREM, and Data Incorporating the CRaTER, COSTEP, and other SEP measurements (PREDICCS) data including uncertainties. The blue line and shaded uncertainty region shows power law fit to the PREDICCS data, $D = D_0(ss_0)^\gamma$, where D is dose, s is Al shielding thickness, and $s_0 = 1$ g/cm^2. The fits have the following coefficients: (top) $D_0 = 35.91 \pm 5.45$ cGy, $\gamma = 0.90 \pm 0.10$, (bottom) $D_0 = 3.56 \pm 0.14$ cGy, $\gamma = 0.11 \pm 0.03$. In the top panel, we find the accumulated doses for D1-D2, D3-D4, and D5-D6 and the intersection with the power law fit to estimate the effective shielding for each of these Cosmic Ray Telescope for the Effects of Radiation (CRaTER) thin-thick detector pairs. The numbers and uncertainties next to the thin-thick detector pairs indicate effective Al shielding depth (in g/cm^2). In the bottom panel, we show PREDICCS data and the power law fit for doses in 10 g/cm^2 H2O. Note that CRaTER detector pair dose rates are comparable to doses in the lens and skin (~ 1 g/cm^2 of H2O as a proxy). However, the tissue-equivalent plastic between D1-D2 and D3-D4 is ~ 6.09 g/cm^2 and therefore not sufficiently thick to evaluate the large internal mass (~ 10 g/cm^2 of H2O as a proxy) associated with organ and blood-forming organ doses. Therefore, the lower panel includes only PREDICCS data and the power law fit but does not contain CRaTER data.

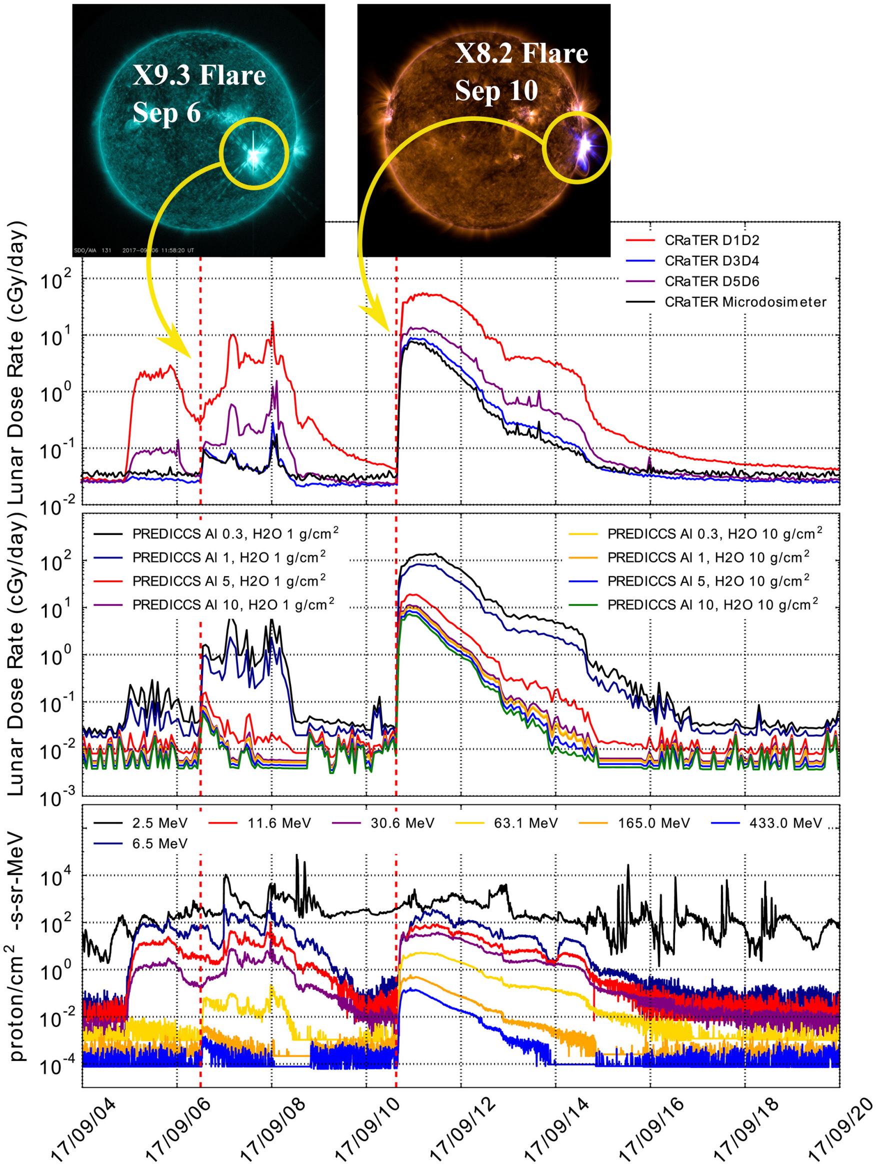

Figure 4.4 Large X-class flares began each of the major events observed in September 2017. The first row includes observations of the erupting active region observed by the Solar Dynamics Observatory (SDO), courtesy of NASA/SDO and the Atmospheric Imaging Assembly (AIA), Extreme Ultraviolet Variability Experiment (EVE), and Helioseismic and Magnetic Imager (HMI) science teams. The first row, left panel solar image of the 6 September X9.3 flare (11:58 UT) is from telescope AIA 131. The first row, right panel image of the 10 September X8.2 flare (16:06) is a combination of wavelengths that includes AIA 193. Dose rates on the lunar surface from Cosmic Ray Telescope for the Effects of Radiation (CRaTER) (second panel) and Predictions of Radiation from REleASE, EMMREM, and Data Incorporating the CRaTER, COSTEP, and other SEP measurements (PREDICCS) (third panel) are shown throughout both events. Note that dose rates in free space are approximately 2 times those on the lunar surface. In the fourth panel, we show energetic particle differential fluxes from GOES.

CHAPTER 5

Characterization of the Space Radiation Environment Through a Modern Secular Minimum (Study 2)

5.1 Introduction

To design successful and safe missions for the coming years, it is important to predict solar activity and the resulting radiation environment. The current cycle is believed to be the beginning of an era of persistent decline in solar activity, that is a secular (grand) minimum (See Section 5.5). Smith et al. (2014) predicted the HMF and solar wind proton flux until 2025 using Schwadron and McComas (2008) and Schwadron et al. (2010b) theories, assuming that the coming decade would resemble the Dalton or the Gleissberg minimum. In the case of a deep grand minimum the HMF becomes very small, the solar wind gets less and less dense, and the size of the heliosphere shrinks significantly. Also, the lower number of coronal mass ejections leads to fewer irregularities to inhibit the GCR diffusion, which in turn leads to higher rates of GCRs and worsening radiation hazards.

In this chapter, I use the lower bound of the 95% confidence level for 3% risk of exposure-induced death (REID) limits to find the most conservative permissible mission durations (PMD) in interplanetary space for probable cases of a Dalton (or Gleissberg)-like minimum. In Section 5.2, I denote coincident conditions applied to the Cosmic Ray Telescope for the Effects of Radiation (CRaTER) data used in this chapter. In Sections 5.3 and 5.4, I give an overview of the GCRs and the modulation potential they undergo as they reach the inner heliosphere. In Section 5.5, I discuss solar activity predictions that lead us to consider scenarios for a modern secular minimum. These scenarios and what they imply for the modulation of the GCRs are discussed in Section 5.7. In Section 5.8 I describe the radiation risks based on these scenarios and the limits they impose on space explorations.

5.2 CRaTER Data

In chapter 4, I described the Cosmic Ray Telescope for the Effects of Radiation (CRaTER) and reviewed its data acquisition. CRaTER aims to investigate the lunar radiation environment. It consists of three pairs of silicon detectors, each pair including one thin (odd-numbered) and one thick (even-numbered) detector. Two pieces of tissue equivalent plastic (TEP) are located between these pairs of detectors (See Chapter 4 for more details). For the purposes of this chapter, I apply a triple coincidence condition so that each observed event must trigger detectors D2, D4, and D6. An additional constraint is for the deposited energy in D6 to be greater than in D4 and the deposited energy in D4 to be greater than in D2; this guarantees capturing incident particles from free space and excludes lunar albedo ions from the observed dose rates. Figure 5.1 shows the effect of these conditions on dose rates observed by CRaTER's first pair of detectors.

5.3 Galactic Cosmic Rays

More than 90% of the low energy GCRs ($<$ 100 MeV) is filtered by the slowed solar wind in the heliospheric interface with the local interstellar medium (LISM) (Florinski et al., 2003). We are highly uncertain about the physics of this interface, the shielding it provides, and how it changes with variations in the solar wind. It most certainly decreases with a decrease in solar wind pressure and the size of the heliosphere. The modified LISM due to the Sun's motion around the center of the galaxy may cause drastic changes in the heliosphere and the radiation environment in the inner heliosphere. A two-dimensional model of the heliosphere-interstellar cloud interaction (Zank and Frisch, 1999) showed that changes in the LISM density lead to drastic changes in the size of the heliosphere. Scherer et al. (2002) demonstrated that these changes affect cosmic ray fluxes. We currently have a limited

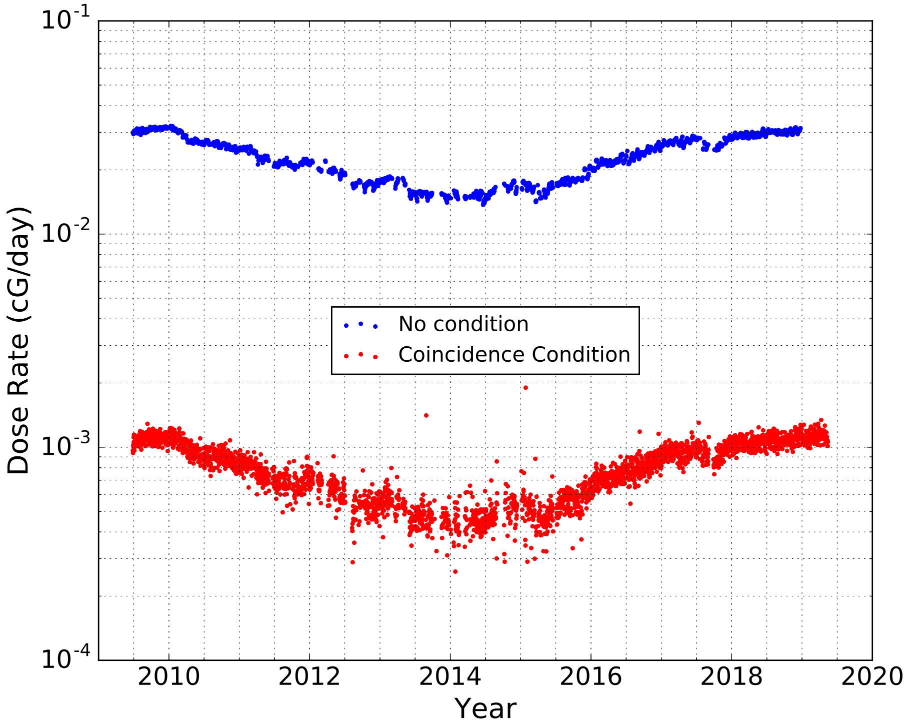

Figure 5.1 Comparing dose rates measured by D1-D2 detector pair with and without coincidence conditions. Blue circles represent CRaTER D1-D2 detector pair dose rates with no coincidence conditions. Red circles represent D1-D2 detector pair dose rates using the triple coincidence $D6 > D4 > D2$ condition.

understanding of the LISM and its interaction with the heliosphere. Studying observations provided by Interstellar Boundary Explorer (IBEX) (McComas et al., 2009), Voyager 1 and 2 (Stone et al., 2005; Richardson et al., 2008), and in the future by the Interstellar Mapping and Acceleration Probe (IMAP) (McComas et al., 2018) will be helpful in obtaining a deeper understanding of the LISM environment, its interaction with the heliosphere, and its effects on the radiation environment of the inner heliosphere.

Radionuclides, such as ^{10}Be, are created by collisions between GCRs and atmospheric atoms and provide a long-term proxy for cosmic ray fluxes. The deposited and sequestered ^{10}Be atoms in the polar ice cores provide a record of GCRs that extends back to 10s of thousands of years. Variations in the ^{10}Be data can be caused by 1) changes in the flux of energetic particles from outside the heliosphere, due to Sun's motion around the center of the galaxy; 2) changes in the interaction region between the heliosphere and the LISM; 3) changes in the HMF as a result of the solar activity; and 4) climatic changes on Earth, which affect the deposition of ^{10}Be atoms concentration in the ice cores.

A reconstruction of annual values of the HMF since 1428 based on ^{10}Be records was reported by McCracken (2007); McCracken and Beer (2015). There is a noticeable agreement between ^{10}Be reconstructed HMF and reconstructed HMF based on sunspot records (for example Rahmanifard et al., 2017; Owens et al., 2016, 2017, etc.) and geomagnetic data (for example Lockwood et al., 2013b,a, 2014b,a; Owens et al., 2016) . This agreement suggests a steady anti-correlation between the Sun's activity and ^{10}Be flux, which demonstrates that the incoming flux entering the heliosphere and the filtration it has undergone in the boundary of the heliosphere have remained relatively unchanged in the last few centuries.

5.4 Modulation Potential

After being filtered by the shielding of the outer heliosphere, the residual GCRs are modulated by the HMF in the heliosphere. Therefore, they are subject to 11-year solar cycles, first noticed by Forbush [1954]. The 22-year Hale cycles also affect the modulation of the GCRs. When the field lines in the northern hemisphere of the sun are directed outward ($A > 0$, the second half of even cycles), the curvature of the field causes ions to drift down over the poles and outward near the equatorial current sheet. During these even $A > 0$ cycles, we observed a broad peak in the flux of positively charged GCRs such as GCR protons. Conversely, during the minimum of odd cycles ($A < 0$), ions travel into the heliosphere along the current sheet, where they encounter the irregularities in the current sheet and CMEs, convecting them out. As a result, access of positively charged GCRs to the inner heliosphere is more restricted during odd $A < 0$ cycles as compared to even $A > 0$ cycles. This leads to a sharp peak during odd $A < 0$ cycles in the GCR fluxes of positively charged GCRs (for example see Webber and Lockwood, 1988). These alternate flat and sharp peaks are demonstrated in Figure 5.2.

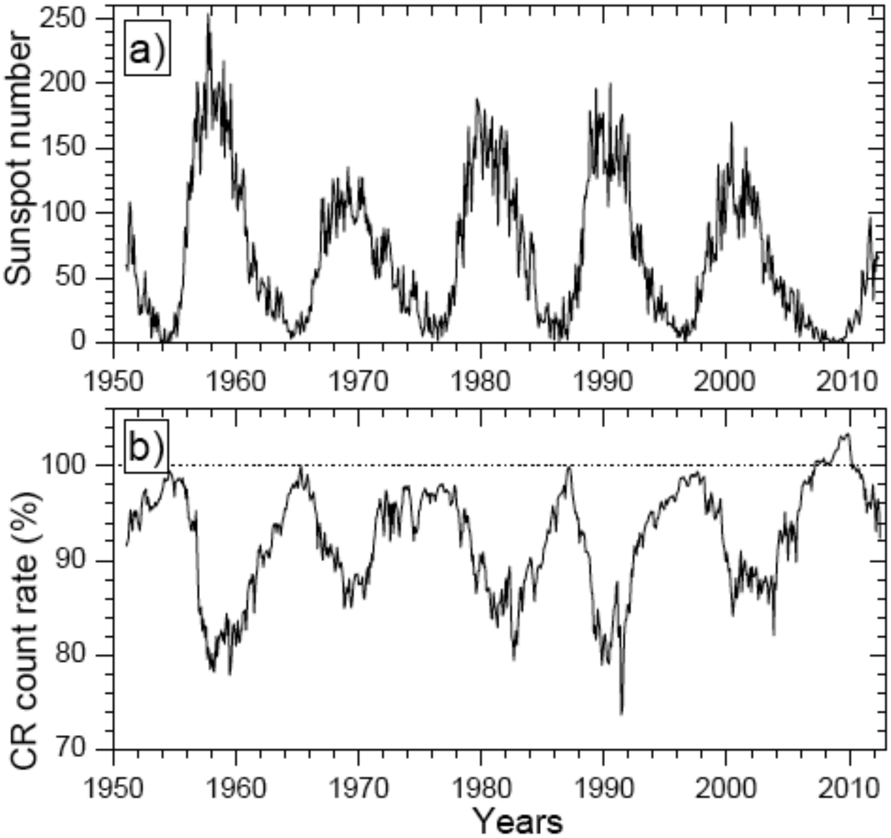

Figure 5.2 Cyclic variations of GCRs count rates (panel b) versus sunspot numbers (panel a) since 1951. In panel b, the count rate of a polar neutron monitor is shown in percentage, with 100% showing neutron monitor count rate from May 1965. Alternate sharp and flat peaks are evident for $A < 0$ and $A > 0$ cycles respectively. This figure is adopted from Usoskin (2013).

The transport of GCRs in the interplanetary medium, and more generally any energetic particle independent of the source, can be described by a Boltzmann equation:

$$\frac{dF(\mathbf{r},\mathbf{p},t)}{dt} = \frac{\partial F(\mathbf{r},\mathbf{p},t)}{\partial t} + [\frac{\mathbf{p}}{\gamma m}.\nabla]F(\mathbf{r},\mathbf{p},t) + [\mathbf{a}(\mathbf{r},\mathbf{p},t).\nabla_p]F(\mathbf{r},\mathbf{p},t), \tag{5.1}$$

where $F(\mathbf{r},\mathbf{p},t)$ is the distribution function, defined as the total number of particles around $\mathbf{r}$ in the volume $d^3\mathbf{r}$ and with momenta around $\mathbf{p}$ in the range $d^3\mathbf{p}$. The following assumptions dictate the transport of energetic particles in the solar wind:

1. The Lorentz force is the only force acting on the energetic particles, gravity will be

ignored.

2. The Lorentz force under consideration is the mean (or average) magnetic field observed by the energetic particles; thus we are ignoring turbulence effects in this analysis (so that $\nabla.\mathbf{a} = 0$, This condition is automatically true of all conservative forces, such as gravity or the Lorentz force.).
3. The Solar wind plasma is assumed to be infinitely conductive $\sigma = \infty$ (flux freezing).
4. The energetic particles may have high velocity, so a relativistic treatment of these particles is necessary.
5. The energetic particles are considered test particles in the system (i.e. their total energy and momentum do not affect the solar wind plasma, nor is there any self-induced electromagnetic effects on the Solar wind plasma)
6. The Solar wind plasma is non-relativistic.
7. The Solar wind mean flow velocity is independent of time on time-scales comparable to the transport time.

Distribution function of the energetic particles is nearly isotropic and can be considered a superposition of a mean phase-space distribution function that is independent of the vector momentum, $F_0(\mathbf{r}, p, t) = \frac{1}{4\pi} \oint_{4\pi} F(\mathbf{r}, \mathbf{p}, t)\, d\Omega_p$ (but depends on the scalar momentum), and a much smaller term that contains the vector dependence on $\mathbf{p}$, $F_1(\mathbf{r}, \mathbf{p}, t)$ so that we can write:

$$F(\mathbf{r}, \mathbf{p}, t) = F_0(\mathbf{r}, p, t) + F_1(\mathbf{r}, \mathbf{p}, t) \tag{5.2}$$

and whenever a time or spatial derivative of F_1 exists and a similar time or spatial derivative of F_0 exists, we will ignore the time or spatial derivative of F_1 in the treatment of the transport equation.

The rate of change of the phase-space distribution function can be approximated by the 1-dimensional Fokker-Planck term, in the frame of reference of the background plasma:

$$\frac{dF(\mathbf{r},\mathbf{p},t)}{dt} = \frac{F_0 - F}{\tau_c} + \frac{1}{p^2}\frac{\partial}{\partial p}[p^2\mathbf{D}_p\frac{\partial F}{\partial p}]. \tag{5.3}$$

In Equation 5.2 we use the fact that, in the Solar wind plasma, collisions between energetic particles and plasma particles are rare, so that the changes in the phase-space distribution function come from energetic particles scattering off the background mean magnetic field in the Solar wind plasma, with a timescale τ_c. As these collisions are inefficient at changing particle energy, but very efficient at changing particle direction, this is a good approximation. Also, $\mathbf{D}_p$ is the diffusion coefficient of momentum diffusion.

We skip going through the mathematic derivations and jump to the final form of the Boltzmann equation, also known as Parker transport equation, that describes the transport of energetic particles in the inner heliosphere:

$$\begin{aligned}\frac{\partial F_0}{\partial t} &+ (\mathbf{V}_{SW}.\nabla)F_0 + \frac{p}{3}(\nabla.\mathbf{V}_{SW})\frac{\partial F_0}{\partial p}\\ &+ \nabla.[-\frac{\tau_c p^2}{3m^2}(\frac{1}{\tau_c^2\Omega_c^2}\nabla + \mathbf{b}(\mathbf{b}.\nabla))F_0 + \frac{p^2}{3m}\frac{1}{q}(\nabla F_0 \times \frac{\mathbf{B}}{B^2})] = \frac{1}{p^2}\frac{\partial}{\partial p}[p^2\mathbf{D}_p\frac{\partial F}{\partial p}],\end{aligned} \tag{5.4}$$

where $\Omega_c = qB/m$ is the gyrofrequency and $\mathbf{b} = \mathbf{B}/B$ is the direction of the magnetic field. We define the spatial diffusion tensor, κ, and the drift velocity, $\mathbf{V}_d$ as:

$$\kappa = \frac{\tau_c p^2}{3m^2}(\frac{1}{\tau_c^2\Omega_c^2}\mathbf{I} + \mathbf{bb}) \tag{5.5}$$

$$\mathbf{V}_d = \frac{p^2}{3m}\frac{1}{q}(\nabla \times \frac{\mathbf{B}}{B^2}) \tag{5.6}$$

Now we can rewrite Equation 5.4 in its final form:

$$\frac{\partial F_0}{\partial t} + (\mathbf{V}_{SW}.\nabla)F_0 + \frac{p}{3}(\nabla.\mathbf{V}_{SW})\frac{\partial F_0}{\partial p} + (\mathbf{V}_d.\nabla)F_0 = \nabla.(\kappa.\nabla F_0) + \frac{1}{p^2}\frac{\partial}{\partial p}[p^2\mathbf{D}_p\frac{\partial F}{\partial p}], \quad (5.7)$$

The second term on the left (Equation 5.7) shows the convection of the distribution function with the solar wind, at velocity $\mathbf{V}_{SW}(r)$, the third term shows the adiabatic deceleration or acceleration of the distribution function due to changing bulk flow velocity, and the forth term demonstrates the particle drift in the Solar wind magnetic field. The summation of all these terms in addition to the time variations of the distribution function (first term on the left) equals to the sum of the spatial and momentum diffusion, on the right.

It is useful to picture visually how these 4 effects operate on energetic particles in space.

- Diffusion, convection, and drift just change the number density of energetic particles without changing the particle energy
- Adiabatic deceleration changes the particle energy as well as the number density.
- Diffusion is the inward movement of energetic particles from high to low density regions
- Convection is the push against inward moving particles due to the solar wind ram pressure
- Adiabatic deceleration is the cooling of energetic particles moving with a plasma that itself is expanding (and thus cooling).
- Drift is the movement of particles in the magnetic field, for example due to the carvature or gradient of the HMF.

Solving the Parker equation for the transport of the GCRs is complex and requires 3D time-dependent self-consistent modelling. However, this problem can be simplified in many ways. Assuming an azimuthal symmetry (for time-scales longer than the solar-rotation period) and quasi-steady changes simplify the approach into a 2D quasi-steady problem.

Assuming a spherically symmetric heliosphere further simplifies it to a 1D problem, for rough estimates. This assumption neglects the drift of the particles due to the curvature of the field lines, but it is useful for long-term studies. Further assumptions, such as a constant solar-wind speed, roughly a power-law GCR energy spectrum, and slow spatial changes of the GCR density, lead to an analytical solution using the force field approximation (Gleeson and Axford, 1967, 1968; Gleeson and Urch, 1971).

In this approach, the transport of GCRs in the interplanetary medium is described by a modulation potential, which is related to the rigidity ($P = pc/q$, where p is the particle momentum, and q is the particle charge) of GCRs. Gleeson and Axford (1968) showed that, for a diffusion coefficient separable into radially and rigidity-dependent components, if $\Phi << T$, the modulation pontential can be described as $\Phi = \frac{\alpha T}{3} \int_r^{R_b} dr \frac{V_{SW}(r,t)}{\kappa(r,E,t)}$. In this equation, E is total energy of the energetic particle, T is its kinetic energy, α is a dimensionless function of T, and R_b is the modulation boundary. They showed that, in this case, the modulation potential approximately corresponds to the energy lost by GCR particles traveling from the LISM to the inner heliosphere, so that $f(r, T, t) = f(\infty, T + \Phi, 0)$. They concluded that $\kappa = \kappa_1(r,t)\beta\kappa_2(P,t)$ is the most likely assumption to describe variations in the intensity of ions observed from 1963 to 1966 and electrons observed from 1965 to 1966, with $\kappa_2(P,t) = P$, in their rigidity range of interest.

Badhwar and O'Neill (1994) provided a species-dependent model to determine the GCR flux over time using stationary solutions of the Fokker-Planck equation. The High-charge (Z) and Energy (HZE) Transport code (HZETRN) uses a one-dimensional Boltzmann transport equation to solve analytically for the GCRs' interaction with materials (Wilson and Badavi, 1986; Cucinotta, 1993; Wilson et al., 2003; Nealy et al., 2007). As CRaTER was at early stages of its mission, an investigation of the radiation from GCRs during the prolonged minimum of solar cycle 23 showed that the weak modulation of GCRs could lead to the highest dose rates in a 25-year period between 1984 and 2009 (Schwadron et al., 2010a). To further explore this era of low solar activity and its elevated radiation from GCRs, Schwadron et al. (2010c) developed the Earth-Moon-Mars Radiation Exposure Module (EMMREM). EMMREM uses a three-layer version of HZETRN 2005 to obtain the GCR dose and other relevant quantities describing the radiation environment (Schwadron et al., 2010c; Townsend et al., 2011).

An agreement between EMMREM results and CRaTER observations was reported by Schwadron et al. (2012). They compared dose rates predicted for the modulation potential from various sources including observations of neutrons using McMurdo data, the Advanced Composition Explorer (ACE) Cosmic Ray Isotope Spectrometer (CRIS), and in situ measurements of the HMF from the OMNI dataset. OMNI compiles a set of data including near-Earth solar wind and magnetic field parameters from multiple sources. Schwadron et al. (2012) found an almost quadratic fit between the HMF and the modulation potential, compatible with the slab turbulence model of cosmic ray diffusion (le Roux et al., 1999). Fitting the modulation potential based on ACE data to the HMF reported by OMNI, Schwadron et al. (2012) inferred $\phi \propto |B|^{1.87}$. Using this power law, Schwadron et al. (2014) showed a correlation between the modulation potential and the mean solar magnetic field:

$$\phi = \phi_1(\frac{V_{SW}}{V_1})(\frac{|\mathbf{B}|}{B_1})^{\gamma} \tag{5.8}$$

where $V_1 = 400km/s$ is a reference solar wind speed, $B_1 = 1nT$ is a reference magnetic field, $\phi_1 = 33.2MV$ is a reference modulation potential, and $\gamma = 1.87$.

To find these parameters, Schwadron et al. (2014) investigated the correlation between the modulation potential from ACE data (O'Neill, 2006) and CRaTER measurements (Joyce et al., 2014) with HMF and V_{SW} from OMNI data. However, as can be seen in Fig. A1 of Schwadron et al. (2014) a departure is noticed from the correlation in Equation 5.8 during the solar maximum. They suggested that this departure could be attributed to globally merged interaction regions (GMIRs). GMIRs are large magnetic structures, which occur due to the pileup of interplanetary coronal mass ejections (ICMEs) in the outer heliosphere. They occur more frequently during phases of high solar activity and play a role in modulating

GCRs McDonald and Burlaga (1997).

In this study, I apply the same methodology using updated CRaTER measurements (2009-2019) to find a new correlation between the modulation potential from CRaTER and the HMF intensity (Figure 5.3). This modulation potential is obtained using dose rates measured by CRaTER applying a coincidence condition to remove side-penetration particles (See Section 5.2). The HMF predictions were obtained from a sunspot-based model at 1 AU (Rahmanifard et al., 2017), in monthly resolution, and monthly global solar wind speed values were adopted from Owens et al. (2017). I used a least square minimization method to find the slope $a = 3.20 \pm 0.10$ and intercept $b = -2.23 \pm 0.07$ of a linear fit to available data points. As can be seen in Figure 5.3, the departure from the correlation in the solar maximum, described in Schwadron et al. (2014) is also evident here, associated with the years 2013 and 2014, when ϕ increases without a significant increase in B.

Additionally, in Figure 5.3, I have used gray circles shaded from the darkest, for the year 2009, to the lightest, 2018, to show the sequence of time. This color code reveals a trend in variations of the modulation potential with HMF, suggesting a hysteresis. Such hysteresis might be associated with Hale cycles, as we are currently in the second half of an even cycle ($A > 0$). At this time the curvature of the field leads ions to drift in from the poles of the Sun, where they avoid being scattered by irregularities near the current sheet, and therefore, their flux is enhanced over a broader period than in peaked odd $A < 0$ cycles. As a result, while B is increasing, ϕ does not increase as much, remains constant, or even decreases. Moreover, this hysteresis is also influenced by the remains of the HMF large scale structures at the edge of the heliosphere, from a past solar maximum, still modulating the GCRs even after the Sun has started its declining phase.

5.5 Predictions of Solar Activity

Space weather forecasting relies on predictions of solar activity as it affects our space environment drastically. First attempts to predict solar activity using modeling techniques date

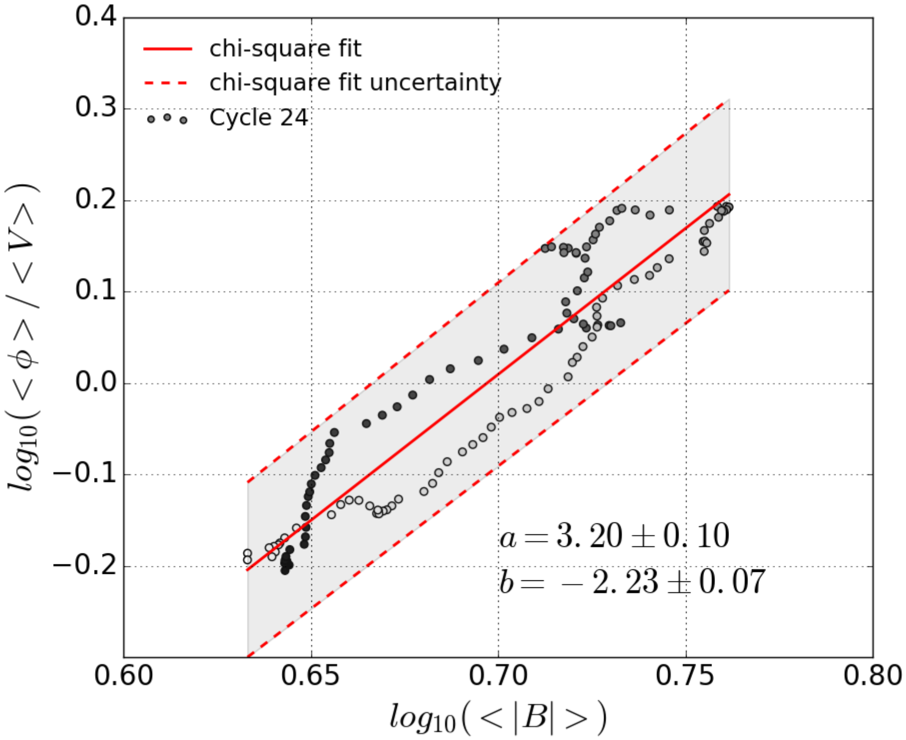

Figure 5.3 The correlation between the modulation potential, the HMF strength, and global solar wind speed is shown using data points with gray circles. Using a color code that varies from dark (2009) to light (2018) reveals a hysteresis behavior. I have used the modulation potential from CRaTER measurements (de Wet et al., 2019), HMF intensity from Rahmani-fard et al. (2017), and global solar wind speed from Owens et al. (2017). A chi-square scheme was used to find a linear fit (red solid line), with a slope ($a = 3.20 \pm 0.10$) and an intercept ($b = -2.23 \pm 0.07$).

back to solar cycle 21 (McIntosh et al., 1979; Brown, 1986, see). Pesnell (2016) compared and categorized models predicting solar cycle 24 concluding that more reliable forecasts of solar activity require more advanced models based on data directly related to the solar magnetic field. Contrasting predictions of solar cycle 24 ranging from unprecedentedly low to unprecedentedly high amplitudes show that we are far from a consensus (For a thorough list of these models see Pesnell, 2014, 2016, and the references therein).

Upton and Hathaway (2018) predicted a cycle 25, slightly weaker than cycle 24 (5% weaker). Wang (2017) and Jiang and Cao (2018) also predicted cycle 25 to be comparable to cycle 24. There are a number of studies predicting cycle 25 to be slightly stronger (for example Cameron et al., 2016; Helal and Galal, 2013; Yoshida, 2014). This might be the case since historically odd cycles are shown to display higher amplitudes than their adjacent even cycles. On the other hand, there are studies suggesting that next solar cycles will have much smaller amplitudes and lead us into deeper phases of a secular solar minimum Shepherd et al. (2014).

The Solar Cycle 25 Prediction Panel has predicted that the next cycle is similar to the current cycle, starts in late 2019 or 2020, peaks in 2023-2026 and ranges in amplitude from 95 to 130 averaged daily sunspot numbers. While the predicted situation is most similar to the beginning of the Gleissberg period, in terms of the transition from an even cycle to an odd one with close amplitudes, there are still doubts about the length and amplitude of the next solar cycle. As we are reassuming human deep space explorations, there is a need to consider scenarios close to deeper secular minima such as the Dalton minimum.

An expectation of the current low solar activity resembling the Dalton or Gleissberg minimum was previously reported (Smith et al., 2014). I updated their Figure 2 to show how realistic this expectation has been so far. In Figure 5.4 I show monthly averaged sunspot numbers from the Dalton and Gleissberg era (top panels) and compare them with the current cycle's observed sunspot numbers (bottom panels). In the bottom left, cycle 5 (blue) is overlaid on cycle 24 (black) persisting into cycle 6 to show a possible Dalton-like condition. The bottom right panel demonstrates the same idea with cycles 12 and 13 for a possible Gleissberg-like secular minimum. As can be seen in this figure cycle 24 is stronger than cycle 5 but slightly weaker than cycle 12, likely suggesting that the next solar cycle will probably show a level of activity between what was observed for the Dalton and Gleissberg eras.

5.6 Extreme Scenarios for a Modern Minimum

Using a Dalton-like cycle 25 (Figure 5.4) as an estimate for the deepest expected solar phase we might be experiencing in the coming decade, we can estimate an extreme scenario for

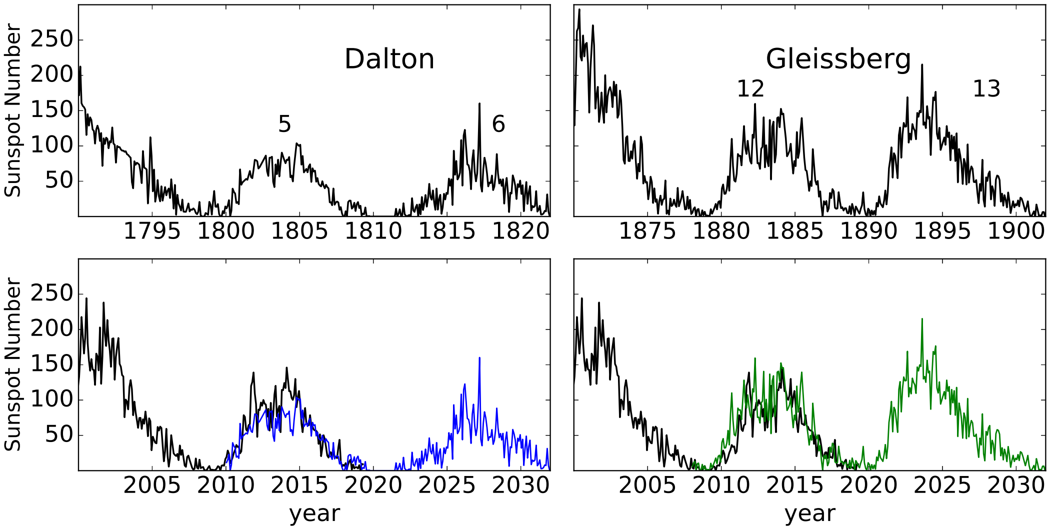

Figure 5.4 The recent decline in solar activity is compared to previous secular minima. The top left panel shows cycles 5 and 6 (Dalton period), and in the bottom left these two cycles are laid over the current cycle. The top right panel shows cycles 12 and 13 (Gleissberg period). In the bottom right, these two cycles are laid over cycle 24.

the radiation environment. A Gleissberg-like cycle 25 obtains a less alarming and probably more realistic condition. To investigate how these conditions affect deep space radiation environment, I first apply the correlation acquired in Section 5.4 to find the modulation potential using B (the HMF intensity) and V_{SW} (global solar wind). The HMF intensity was obtained from Rahmanifard et al. (2017) for sunspot numbers adopted from cycle 6 (for a Dalton-like minimum) and cycle 13 (for a Gleissberg-like minimum); V_{SW} was adopted from the Owens et al. (2017) reconstruction of the global solar wind speed for those cycles.

I applied the same slope and intercept found in the aforementioned correlation for the next solar cycle, assuming a Dalton-like or a Gleissberg-like minimum (Figure 5.5, panel a), which caused the modulation potential to decrease to values as low as $223.0 \pm 43.14 MV$ (See Figure 5.6, panel c). However, it is evident from the hysteretic shape of cycle 24 shown in Figure 5.3 that not all phases of the cycle share the same slope. As can be seen in this figure, the slope decreases significantly as the cycle proceeds to a minimum. This might suggest that in the last phases of a solar cycle ϕ does not vary significantly with the decreasing HMF intensity, somewhat suggesting a floor in the modulation potential.

BON14 model has an embedded floor in the modulation potential at 420 MV, associated with characteristics of the local interstellar spectrum (O'Neill et al., 2015). de Wet et al. (2019) have used the BON14 model to obtain modulation potential and PMD all the way back to 1749, showing a floor in PMD values resulting from a floor in the modulation potential. I have implemented this floor in my predicted correlation between the modulation potential and HMF for a possible Dalton-like or Gleissberg-like minimum (Figure 5.5, panel b). This floor prevents the modulation potential from decreasing indefinitely with a weakening solar magnetic field.

In order to implement this floor, the modulation potential obtained based on Figure 5.5 (panel a) was raised so that the minimum value of ϕ reached a floor of 420 MV as predicted by the BON14 model. Increasing all ϕ values would have resulted in a discontinuity in the modulation potential values between observed values to this day and the predicted values in Figure 5.6 (panel d). In order to avoid that, I assumed that the modulation potential does not vary significantly during the first year of the expected cycle 25, resulting in a smooth transition between the two cycles in spite of different correlation patterns.

The absolute value of the modulation parameter in the BON14 model is based on arbitrarily chosen constants, so it is not significant. The values of ϕ in this model demonstrate the degree of modulation of the GCRs based on their choice of parameters. The aforementioned floor in the modulation parameter is imposed by their set of local interstellar (LIS) parameters describing the flux of GCR ions at 100 AU, where the modulation of them is negligible. This set of initial parameters is obtained using satellite and balloon missions covering cycles 20 to 24. Since most of this period falls into the modern solar maximum, it is plausible that this set of parameters does not accurately describe the condition at a deep solar minimum, such as the Dalton period.

As mentioned previously, the existence of a floor can be justified by the seemmingly constant flux of the GCRs into the heliosphere at different phases of solar activity. However, the value of the floor in modulation potential during solar minimum specified in the BON14 model is based on the observed relationship between sunspot number and GCR flux in the modern era. The trend of weakening peak sunspot number associated with the solar maxima observed over the last 60 years indicates we could be moving into another grand minimum scenario. Since the floor in modulation potential present in the BON14 model has yet to be tested in a grand minimum scenario, it is possible that a persistent steep increase in the level of dose rates observed by CRaTER may lead to values smaller than 420 MV. According to the correlation between HMF, solar wind speed, and solar modulation potential described in Section 4, the value obtained for modulation potential based on CRaTER observations is expected to fall below the predicted floor if the current solar cycle persists into another prolonged deep minimum leading us to grand minimum-like condition. If this is the case, the LIS modulation parameters within the BON14 model should be revised to account for the newly observed floor in modulation potential. Alternatively, as we are experiencing the second half of an even solar cycle, the flux of GCRs might end up in a flat peak, adhering to the floor predicted by LIS parameters used in the current version of the BON model.

In Figure 5.6, I show the HMF intensity, global solar wind speed, and modulation potential since 1975, covering solar cycles 21-24 (black line) and extending to possible low solar activity scenarios for cycle 25 (green and blue for Gleissberg-like and Dalton-like cases respectively). In panel (a) I show the HMF intensity adopted from Rahmanifard et al. (2017) who used sunspot reconstructed data as a proxy for the frequency of CMEs (as the source of closed magnetic flux) to reconstruct a time series for the HMF based on the Schwadron et al. (2010b) theory. In panel (b) I show reconstructed global solar wind based on the Magnetohydrodynamics Algorithm outside a Sphere (MAS) model, which compares global MHD solutions to observed photospheric magnetograms (Owens et al., 2017).

In Figure 5.6, panels (c) and (d) present the modulation potential through the space age from BON14 model (black line), observed by CRaTER (red line), and for expected scenarios of a Gleissberg or Dalton-like cycle 25 (green and blue lines respectively with shaded uncertainty regions). The predicted modulation potential for cycle 25 shown in panel (c) is obtained by applying the correlation from Figure 5.5 (panel a). As can be seen, the modulation potential falls below the 420.0 MV floor embedded in BON14 model during the minimum phases of a Gleissberg-like cycle 25 and throughout the whole cycle for a Dalton-like cycle. Implementing a 420.0 MV floor in the modulation potential raises these values, leading to more effective modulation of the GCRs in the next solar cycle as shown in panel (d). However, the Dalton-like case shown in panel (d) still exhibits unprecedentedly low modulation in the solar maximum and throughout the cycle.

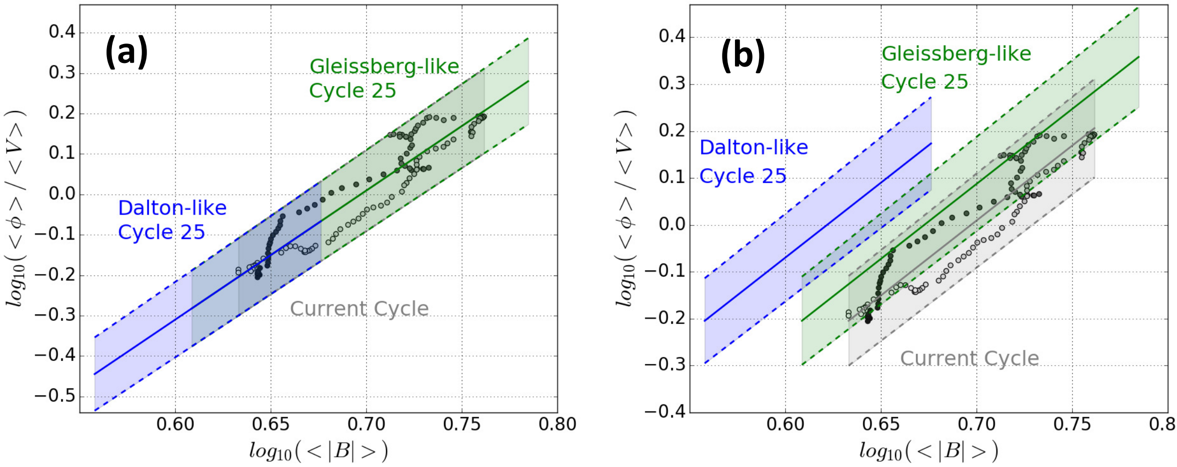

Figure 5.5 **Panel (a)** The correlation acquired from cycle 24 is applied to two possible scenarios for cycle 25. The HMF strength for a Dalton-like and a Gleissberg-like cycle 25 is calculated to find the modulation potential for these scenarios using the same slope and intercept from Figure 5.3. I used blue (green) lines and shaded uncertainty regions to show Dalton (Gleissberg) cases. **Panel (b)** The same slope from Figure 5.3 and panel (a) is applied to the speculated Dalton (Gleissberg)-like solar cycle 25, applying the floor from BON14 ($\phi = 420.0$ MV).

5.7 Conservative Radiation Risks Based on Extreme Scenarios

A modulation potential-based response function was generated for CRaTER instrument using the MNCP6 model (de Wet et al., 2019). de Wet et al. (2019) passed the geometry of the instrument to a Monte Carlo transport code for various boundary condition fluxes associated with specific values of modulation potential and assembled the results into a response function. They used this response function to produce a modulation potential data set based on CRaTER observations. As mentioned in Section 5.2, dose rates observed in the third pair of CRaTER detectors with a triple coincidence condition have been employed to create this modulation potential record since 2009. The resulting modulation potential record is shown in Figure 5.6, panels (c) and (d), in red.

Employing the CRaTER response function, We can use my predicted modulation potential for an expected declining solar cycle 25 to predict the worst-case radiation environment in deep space. We used this method to predict D5-D6 dose rates with a triple coincidence condition for the coming years (Figure 5.7). Additionally, we investigated the risks of a worsening radiation environment caused by a declining solar activity for future human space explorations. The risk model used in de Wet et al. (2019) includes the HZETRN code for male and female phantoms (known as MAX and FAX) in a spherical spacecraft exposed to a radiation environment associated with specific values of the modulation potential. They produced tables of effective dose rates for male and female anatomies behind Aluminum shielding ranging from 0.1 to 40 g/cm^2 for a modulation potential varying from 420 MV to 1400 MV. We employed their results to find the 3% REID at 95% confidence level for 45-year-old astronauts, behind 20 g/cm^2 Aluminum shielding, and the resulting PMD for expected scenarios for cycle 25.

Figure 5.7 shows the modulation potential for a speculated modern minimum similar to the Dalton minimum (blue) or the Gleissberg minimum (green). In the top left panel, the modulation potential is presented based on a correlation shown in Figure 5.5 (panel a), assuming the same slope and intercept for cycle 25 as was observed for cycle 24. This assumption, when combined with a drastic decrease in the level of solar activity similar to what happened during the Dalton period, leads to a radical decrease in the modulation potential. As shown in the bottom left panel, such a decrease in the modulation of the GCRs leads to a further increase of the radiation hazard from the already unprecedentedly high radiation risks. A shallow solar maximum similar to the one from cycle 6 will not be able to effectively moderate such a radiation environment.

A Gleissberg-like condition will not lead to a situation as dramatic. Particularly, a solar maximum similar to the observed maximum of cycle 13 will recover the radiation environment by lowering dose rates to values smaller than the dose rates observed during the solar maximum of cycle 24. PMD values, based on a 3% REID at 95% confidence level, for these conditions, are presented in Figure 5.8 for 45-year-old astronauts (top left for male, bottom left for female) behind 20 g/cm^2 Al Shielding. A Dalton-like scenario lowers the PMD throughout the cycle so that the minimum PMD will be as low as $197.0^{+18.8}_{-18.2}$ days for male and $153.4^{+14.8}_{-14.2}$ days for female astronauts, while the maximum PMD will be slightly higher. For a Gleissberg-like scenario, both minimum and maximum PMD are significantly higher.

The right panels in Figure 5.7 and Figure 5.8 are allocated to possible scenarios for cycle 25 using a correlation illustrated in Figure 5.5 (panel b). I raised the modulation potential obtained based on Figure 5.5 (panel a) so that the minimum value of the modulation potential reached a floor of 420 MV. The resulting modulation potential and dose rates are shown in the top right and bottom right panels of Figure 5.7, respectively. The predicted dose rates for this case are significantly reduced compared to the previous case. Therefore, the predicted PMD values both for male and female astronauts exhibit a noticeable increase, but they remain low for a Dalton-like cycle. Minimum and maximum values for the modulation potential and PMD time series presented in Figure 5.7 and Figure 5.8 are summarized in Table 5.1).

Based on previously observed trends, odd cycles likely exhibit higher levels of activity than their adjacent even cycles. Therefore, cycle 25 is expected to be slightly stronger than cycle 24, resembling the solar cycle transition from cycle 12 to cycle 13 (during the Gleissberg period). However, cycle 24 had a smaller amplitude than cycle 12. This reinforces speculations that cycle 25 will likely lead us to a deeper phase of a modern secular minimum -

perhaps something between the Gleissberg and the Dalton minimum. Furthermore, assuming a constant flux of GCRs passing through the heliospheric interface leads to a floor in the modulation potential. The amount of shielding provided by the heliospheric interface likely decreases during extremely deep phases of grand (secular) minima. The BON14 model only relies on data from cycles 20-24 to obtain LIS parameters, during which we have mostly experienced a secular maximum; these values likely fail in accurately describing a deep minimum phase. Therefore, we expect the next solar cycle, if deeper than cycle 24, to lie somewhere between these extreme cases.

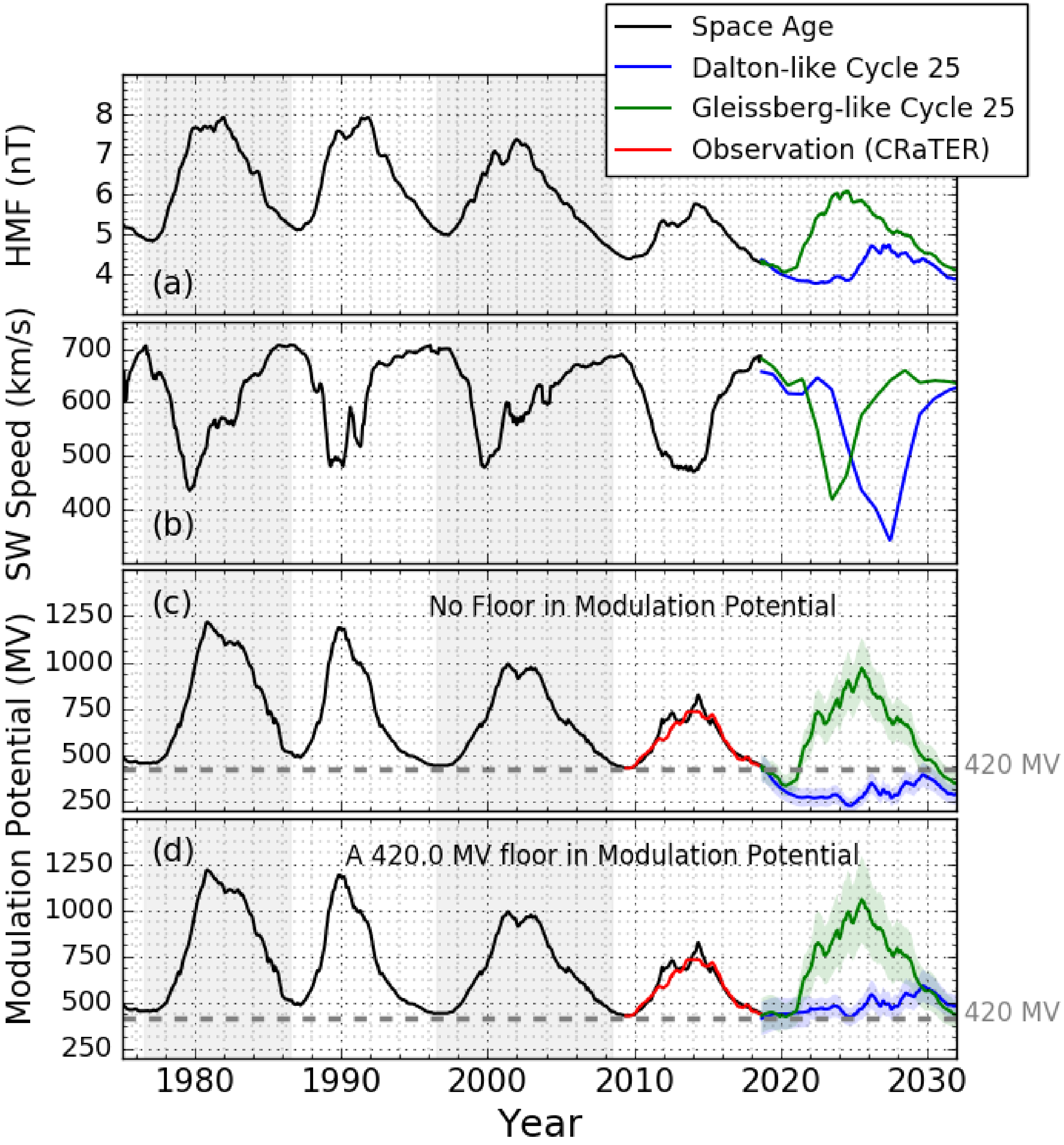

Figure 5.6 Panel (a) shows the HMF intensity through the space age (black) and extending to a speculated cycle 25 (blue and green for Dalton-like and Gleissberg-like cases respectively). Panel (b) shows the global solar wind speed from Owens et al. (2017) using the same color code. Panels (c) and (d) show the modulation potential from BON14 through space age (black) and the modulation potential from CRaTER measurements in cycle 24 (red). The modulation potential for a Dalton-like and a Gleissberg-like cycle 25 based on the correlation from this work (Figure 4a) is shown in Panel (c). Panel (d) shows the modulation potential for these two cases applying the floor in modulation potential from BON14 (using correlations in Figure 4b).

Table 5.1. Minimum and maximum values obtained for the modulation potential and permissible missions duration (PMD) based on a Dalton-like and a Gleissberg-like cycle 25. For the case without a floor, we have applied the correlation obtained for cycle 24 to expected cycle 25 scenarios. For the case with the floor, we have applied the same correlation and raised all modulation values so that the minimum values reach the 420 MV floor in BON14 model.

	Cycle 25 resembling	Modulation min.	Potential (MV) max.	PMD, min.	Male (days) max.	PMD, min.	Female (days) max.
Without	Dalton	223.0 ± 43.14	433.0 ± 72.96	$197.0^{+18.8}_{-18.2}$	$297.2^{+38.7}_{-37.1}$	$139.0^{+13.0}_{-12.6}$	$153.4^{+14.8}_{-14.2}$
Floor	Gleissberg	330.1 ± 58.09	969.2 ± 166.1	$245.7^{+28.5}_{-27.2}$	$619.6^{+117.4}_{-110.0}$	$172.9^{+20.0}_{-19.0}$	$434.8^{+80.3}_{-75.8}$
With	Dalton	420.0 ± 71.45	591.9 ± 87.65	$290.4^{+37.7}_{-35.9}$	$383.2^{+50.5}_{-48.2}$	$204.3^{+26.6}_{-25.2}$	$221.8^{+22.7}_{-22.0}$
Floor	Gleissberg	420.0 ± 71.45	1059.0 ± 235.0	$290.4^{+37.7}_{-35.9}$	$682.1^{+174.0}_{-159.1}$	$204.3^{+26.6}_{-25.2}$	$477.4^{+120.1}_{-109.0}$

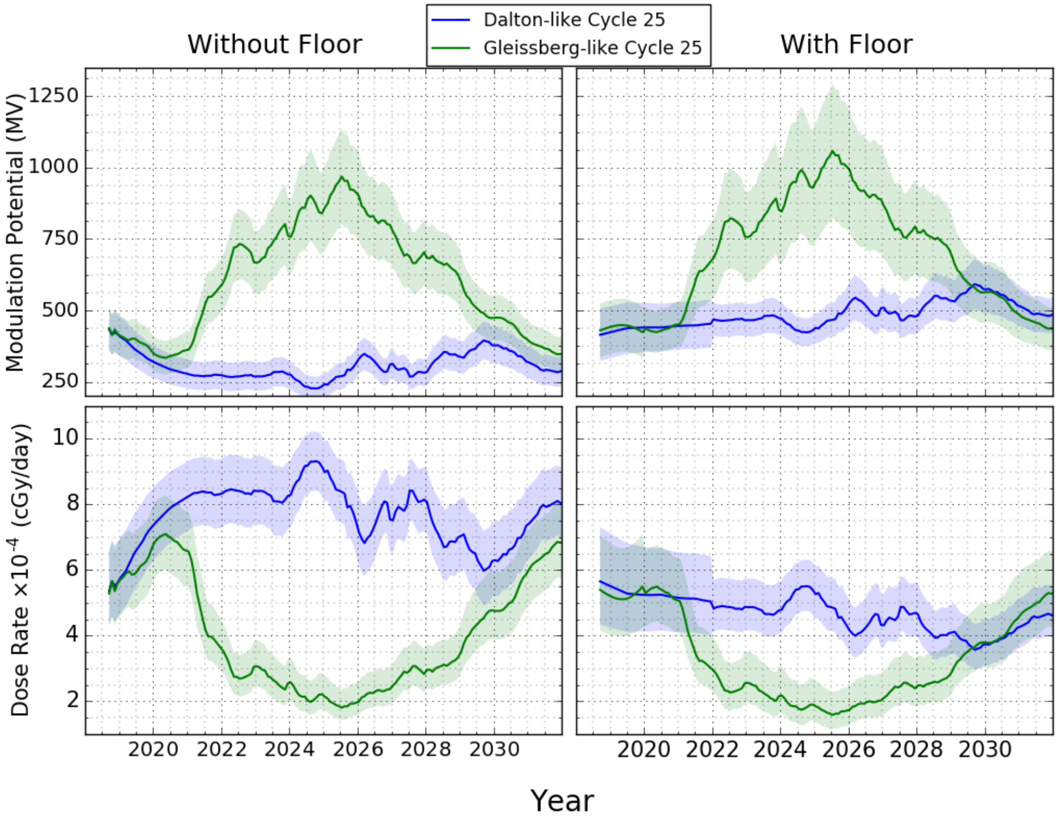

Figure 5.7 Top Panels show the modulation potential for possible cases of a Dalton-like cycle 25 and a Gleissberg-like cycle 25 once using the correlation obtained from Figure 4a (without a floor, top left), and once using the correlation obtained in Figure 4b (with the floor, top right). Bottom panels present dose rates expected to be observed by CRaTER D5-D6 pair of detectors with a triple coincidence condition for these cases.

5.8 Summary and Conclusion

The minimum magnetic field has been in decline through the last few solar cycles. A protracted solar minimum in cycle 23-24 and a brief, weak solar maximum in cycle 24 may provide an indication of future conditions. Therefore, we consider the possibility of a worsening radiation environment associated with high fluxes of galactic cosmic rays that are increasing even more rapidly than our previous estimates.

In this study, I employed the HMF and solar wind speed to find dose rates throughout the space era. I also obtained the HMF based on Rahmanifard et al. (2017) work, by assuming

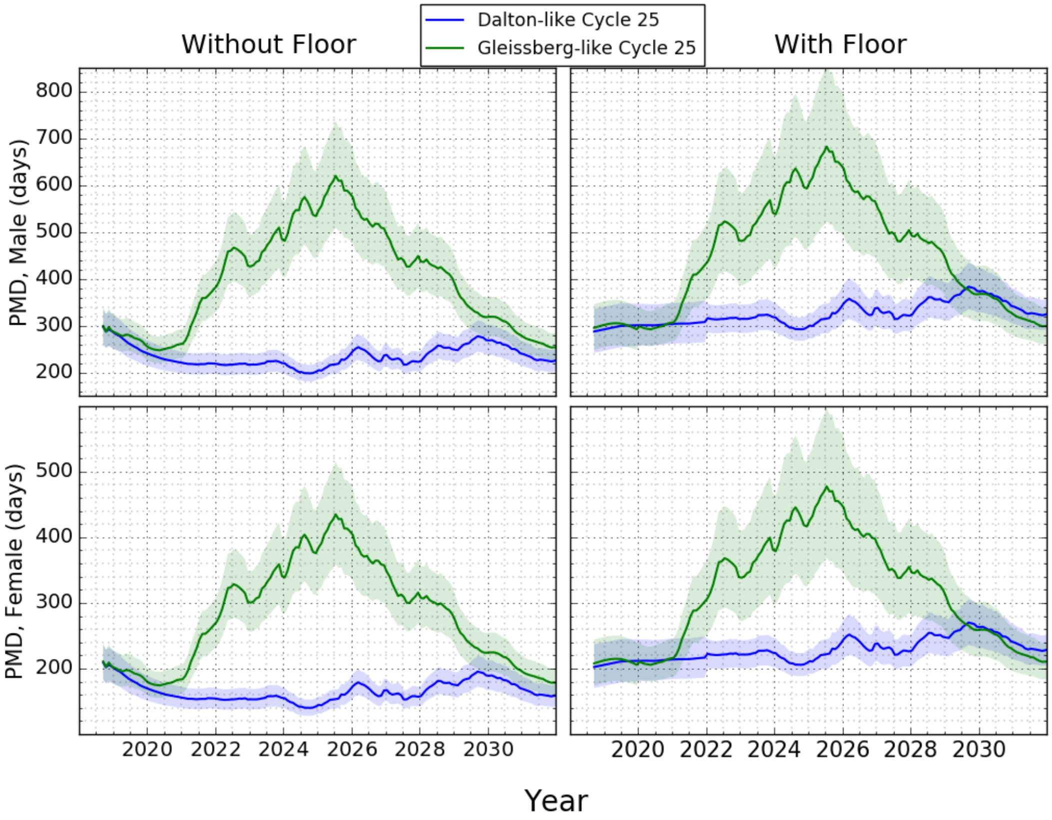

Figure 5.8 Predicted PMD for possible cases of a Dalton-like cycle 25 and a Gleissberg-like cycle 25 once no floor in the modulation potential (top left, 45-year-old male astronaut; bottom left, 45-year-old female astronaut), and once assuming a floor of 420.0 MV embedded in the BON14 holds in the deepest phases of solar activity (top right, 45-year-old male astronaut; bottom right, 45-year-old female astronaut.

that the present unusually low solar activity will persist and worsen in the coming years. I used sunspot numbers from Gleissberg and Dalton periods to update the correlation between the HMF and the modulation potential from Schwadron et al. (2014) based on CRaTER data. I applied it to HMF and global solar wind speed expected for Gleissberg-like and Dalton-like cycle 25 to find the modulation potential for these scenarios.

We used the de Wet et al. (2019) risk model to find dose rates and the resulting permissible mission durations (PMD) from the modulation potential in the previous step. The PMD time series were calculated for 45-year-old astronauts, behind a 20 g/cm^2 nominal spacecraft shielding, based on a 3% REID at 95% confidence level. For a Dalton-like cycle 25, we obtained a minimum PMD of $197.0^{+18.8}_{-18.2}$ days for male and $139.0^{+13.0}_{-12.6}$ days female astronauts.

For a Gleissberg-like cycle 25, we found a minimum PMD of $245.7^{+28.5}_{-27.2}$ days for male and $172.9^{+20.0}_{-19.0}$ days for female astronauts. When incorporating the 420.0 MV floor, similar values are obtained for both Dalton-like and Gleissberg-like cycles: $290.4^{+37.7}_{-35.9}$ days for male and $204.3^{+26.6}_{-25.2}$ days for female astronauts.

The heliospheric interface, which filters the majority of the GCRs is notably affected by solar activity but also by the LISM conditions. Our Sun, on its journey through the Milky Way Galaxy, might have encountered different environments: from hotter, more dilute bubbles to denser and colder clouds than the VLISM that we are currently experiencing. Frisch (2006) has studied the significance of our galactic environment for the heliosphere and earth. In order to investigate the interstellar boundary condition, which drastically affects our space environment, Interstellar Boundary Explorer (IBEX) was launched in 2008.

In the next two chapters, we turn our attention to the effect of solar cycles on the filtration of the interstellar neutral (ISN) atoms. Particularly, we study the effect of radiation pressure on rise and decline of the ISN H signal observed by IBEX over different phases of solar activity. However, due to a technical complexity that will be discussed in Chapter 6, we focus on the longitudinal shift of the signal rather than its intensity. I show that this longitudinal shift is a worthwhile effect, which demonstrates the ISN H signal variations with solar activity. The temporal and spatial variations of the radiation pressure complicate the analysis of ISN H flow. However, throughout Chapter 6, we assume that an effective radiation parameter, appropriately averaged over the last phases of an ISN H atom journey, can address the effect of the radiation pressure on the ISN H trajectory. The justification for this assumption is provided in Chapter 7.

CHAPTER 6

Radiation Pressure from Interstellar Hydrogen Observed by IBEX Through Solar Cycle 24 (Study 3)

6.1 Introduction

The very local interstellar medium (VLISM) is a dilute, partially ionized gas consisting of neutral atoms, such as H, He, C, Ne, and a plasma part consisting of electrons, protons and heavier ions. The relative motion of the Sun with respect to the VLISM at a speed of $\sim$ 25 km/s, reported by several studies, causes an inflow of the interstellar neutral (ISN) atoms into the inner heliosphere, unimpeded by the solar magnetic field. However, the distribution function of these ISN atoms is modified by the Sun's gravity and, for H atoms, by radiation pressure as well. Also, ISN atoms are depleted via ionization processes both at the heliospheric interface and after they enter the heliosphere.

The $\sim$ 25 km/s inflow speed mentioned earlier is obtained by direct neutral gas observations with Ulysses (Witte, 2004; Bzowski et al., 2014; Wood et al., 2015); UV backscattering observations from SOHO (Vallerga et al., 2004) and neutral gas observations with IBEX (McComas et al., 2009; Fuselier et al., 2009) for ISN He (e.g., Bzowski et al., 2015; Schwadron et al., 2015; McComas et al., 2015b). Other studies investigated ISN He parameters, including the temperature, density and flow direction (Gloeckler et al., 2004; Lallement and Bertin, 1992; Linsky et al., 1993; Möbius et al., 2004, the latter study provides a thorough discussion of methods to investigate VLISM parameters using ISN He). A similar set of studies was conducted to find the parameters associated with ISN H. The density of ISN H at the termination shock needed to slow down the solar wind from the values measured by

Ulysses at ~ 5 AU to the values reported by Voyager upstream of the termination shock was estimated as 0.09 cm^{-3} (Richardson et al., 2008). Based on the pickup ion production rate observed by Ulysses (Gloeckler and Geiss, 2001), the density of ISN H at the termination shock was estimated to be ~ 0.087 cm^{-3} (Bzowski et al., 2008). Another study based on the Lyα radiation transport using Cassini and Voyager 1 data reported values between 0.085 cm^{-3} and 0.095 cm^{-3} for this parameter (Pryor et al., 2008). The Lyα absorption line and its re-emission by the ISN H known as helioglow, measured by SOHO/SWAN, was used to find the flow direction of ISN H (Lallement et al., 2005, 2010). Müller et al. (2008) used various global heliosphere models to show that the termination shock location agrees between these models within reasonable errors.

Far away from the heliospheric interface, the ionized and neutral parts of the VLISM are highly coupled through charge exchange and elastic collisions. Once the interstellar plasma meets the obstacle created by the heliosphere, it is diverted, decelerated (possibly through a bow wave rather than a bow shock; see McComas et al., 2012; Zank et al., 2013) and heated. Along with this interaction, the VLISM magnetic field is draped around the heliosphere. On the other hand, the neutral part of the VLISM, not affected by the magnetic field of the heliosphere, moves toward the Sun without substantial changes. In the outer heliosheath, the space between the bow shock (or bow wave) and the heliopause, charge exchange continues, and two new ion and neutral populations are created as a result. The former neutral particles become ionized and start interacting with the plasma part of the VLISM, which causes them to be deflected and thermalized (Frisch et al., 2009). Protons of the outer heliosheath, are neutralized and decouple from the ISM magnetic field, while maintaining their kinematic properties before the collision to create a new population: the so-called "secondary population" as opposed to the "primary population". This secondary population is hotter and slower than the primary flow and piles up to form the hydrogen wall (for a more detailed discussion see Frisch et al., 2009). In turn, the creation of the secondary population leads to selective filtration of the primary population, which leaves a distribuation that is faster and cooler.

The ionization processes that occur further inside the heliopause, including photoionization, charge exchange, and electron impact ionization, lead to further loss of the neutral particles (e.g., Bzowski et al., 2013b; Bochsler et al., 2014). For the case of ISN H, charge exchange and photoionization are the dominant processes. Both scale with $1/r^2$ since the charge exchange is proportional to the solar wind flux and photoionization scales with the solar UV photon intensity. While the radiation force decelerates the ISN H flow, these loss processes reduce the flow. As a result, the ISN H density decreases and its energy does not increase as much or not at all as they approach 1 AU, where we observe them with the IBEX-Lo neutral atom camera. An important selection effect due to ionization causes faster atoms to be more likely to survive to 1 AU. This effect causes an effective ~ 2 km/s increase in the ISN H flow speed (Bzowski et al., 1997).

The low flux of ISN H is not the only barrier in detecting the signal with IBEX. After passing the IBEX-Lo collimator the incident neutral atoms hit a diamond-like carbon surface that is coated with a mono-layer of water. Here, they either are converted to negative ions or sputter negative ions. The conversion surface, which is key to detecting the ISN neutral atoms (Wurz et al., 1997, 2008; Fuselier et al., 2009), presents a challenge when it comes to separating ISN H from He atoms. While the low-energy ISN H atoms are expected to be converted at the surface to H^- ions and form a broad but faint signal in the first two energy steps, the much more abundant and energetic ISN He atoms sputter H^- ions from the conversion surface, which flood the first four energy steps (see Figure 1 from Möbius et al., 2012). As a result, it is extremely challenging to extract the ISN H signal from the more abundant ISN He, specifically during years of high solar activity when the H signal drops off dramatically. The radiation force, however, shifts the peak longitude of the ISN H signal so it does not coincide with other neutral atom peaks, making ISN H detectable in spite of the interference by the sputter products of ISN He.

The first direct detection of ISN H was reported by Möbius et al. (2009). Saul et al.

(2012) provided a first quantitative analysis of the first two years of IBEX observations, revealing an offset in the signal both in longitude and latitude over time. They developed two techniques to distinguish the ISN H signal from the sputtered ISN He: 1) determine and subtract ISN He by modeling the observed spectrum as the sum of ISN He and the residual ISN H component (the so-called subtraction method) 2) use the He signal from a higher energy step as a proxy to extract the ISN H signal. The resulting ISN H signal was shown to be consistent with a radiation pressure that exceeds the gravitational force. It is noteworthy that this is even the case for 2009-2010, i.e. during low solar activity. As the solar activity rose, the ISN H signal was found to fall near background levels in 2012 (Saul et al., 2013). Saul et al. (2013) also reported an increasing longitudinal offset with increasing solar activity in the first four years of IBEX observations. During the most active phases of cycle 24 the signal almost disappeared, partially due to switching to a lower post-acceleration voltage in the summer of 2012, which resulted in even lower counting statistics (McComas et al., 2014). The most recent IBEX observations of ISN H showed a signal recovery in consecutive seasons of 2017-2018 as we approach another solar minimum (Galli et al., 2019). The longitude offset of the ISN H signal peak appeared to be overshadowed by the uncertainties associated with the strong ISN He signal in their analysis.

Early attempts to model interstellar neutral atoms were inspired by the backscattered solar Lyα measurements resulting in so-called cold gas models (Fahr, 1968; Blum and Fahr, 1970; Axford, 1972; Vasyliunas and Siscoe, 1976). These models assume the distribution function of the interstellar neutral gas has a central velocity and zero temperature. The cold gas model was generalized to include the gravitational force and ionization processes. The next step in modeling the interstellar neutral gas allowed consideration of a drifting Maxwellian distribution at infinity with a finite temperature. A class of hot-gas models also took into account solar gravitation and radiation pressure as well as ionization losses (Fahr, 1971, 1979; Thomas, 1978; Meier, 1977; Wu and Judge, 1979). While classical hot gas models adequately predict general estimates of ISN H flow, additional improvements consider important effects: 1) modification of the interstellar gas distribution when entering the heliosphere through the interface region (Baranov and Malama, 1993; Izmodenov, 2001; Katushkina et al., 2015; Izmodenov and Alexashov, 2015); 2) latitudinal asymmetries in solar parameters (Bzowski et al., 2002; Mccomas et al., 2003; McComas et al., 2006, 2008); 3) solar cycle variability (Bzowski and Rucinski, 1995; Bzowski et al., 1997, 2003; Pryor et al., 2003; Izmodenov, 2004; Bzowski et al., 2008; Tarnopolski and Bzowski, 2009).

In this work, we concentrate on a quantitative determination of the effect of radiation pressure on ISN H and on the longitudinal shift of the ISN H peak over almost a full solar cycle. A reported discrepancy in the ratio of ISN H counts in the lowest two energy channels between all available models and the observed signals (further explained in Section 6.7) compelled me to focus my study of the longitudinal shift of ISN H on the lowest energy step. I fit a Gaussian to the peak of the ISN H signal observed by IBEX (Galli et al., 2019) for each season to find its longitude. Using the analytical Full Integration Model (aFINM, further explained in Section 6.3), I find an effective parameter μ for each season to match the observed peak longitude. I aim to show variations in the peak longitude and, as a result, variations in parameter μ with solar activity. I briefly discuss the basis for the existing models in Section 6.2, with focus on the trajectories of the ISN H atoms. In Section 6.3, the resulting distribution function and its essential parameters are reviewed along with a brief history on the current models that are specialized to predict the ISN flux observed by IBEX. In Section 6.4, I describe the IBEX-Lo detector and its energy channel response to the ISN H signal. The data used in this study and its retrieval methods are presented in Section 6.5. The observed temporal shift in the ISN H signal and the predicted parameter μ based on that shift is presented in Section 6.6 and discussed in Section 6.7. The justification for the use of a stationary model in the complex case of ISN H is relegated to Chapter 7. Concluding remarks are provided in Section 6.8.

6.2 ISN H Trajectory

ISN atoms have the same bulk speed, and their mean energy scales with their mass. The Sun's gravitational field and ionization processes modify the distribution function of the ISN gas as it flows through the heliosphere and lead to characteristic trajectories for the neutral atoms. Figure 6.1 shows a schematic diagram of the trajectory of the ISN atoms. For ISN He, Ne, and O, the attractive gravitational field bends the trajectories toward the Sun (green line in Figure 6.1). For ISN H, this characteristic trajectory is further modified by radiation pressure. The radiation pressure is an outward force in the radial direction exerted on the ISN H atoms due to resonant absorption and re-emission of Lyα. The radially outward moving solar Lyα photons impart their momentum onto the ISN H atoms, through resonant absorptions. The re-emission, on the other hand, occurs in a random direction so that the combination of successive absorptions and re-emissions give rise to the radiation pressure that points radially outward. The effece of radiation pressure on ISN H results in a possibly repulsive net force ($\mathbf{F}_{net}$) if $\mathbf{F}_{rad} > \mathbf{F}_g$, which bends the trajectory away from the Sun.

$$\mathbf{F}_{net} = \mathbf{F}_g + \mathbf{F}_{rad} = (1 - \mu)\mathbf{F}_g, \tag{6.1}$$

where μ is a dimensionless parameter describing the ratio of the radiation pressure force to the gravitational force ($\mu = |\mathbf{F}_{rad}|/|\mathbf{F}_g|$), which is a function of time, heliolatitude and radial velocity. In Chapter 7, I investigate variations of μ with time and radial velocity of the ISN H atoms and their effect on the ISN H signal.

As shown in Figure 6.1, a repulsive net force results in ISN H atom trajectories bent outward from the Sun, which reach their perihelion at larger ecliptic longitude and thus are observed by IBEX in later orbits, increasing the peak longitude (λ_{peak}). An attractive net force in this case ($\mathbf{F}_{rad} < \mathbf{F}_g$) moves the trajectory's perihelion toward earlier IBEX orbits, decreasing λ_{peak}, although still at larger values than found for ISN He and O due to a weaker net force acting on ISN H.

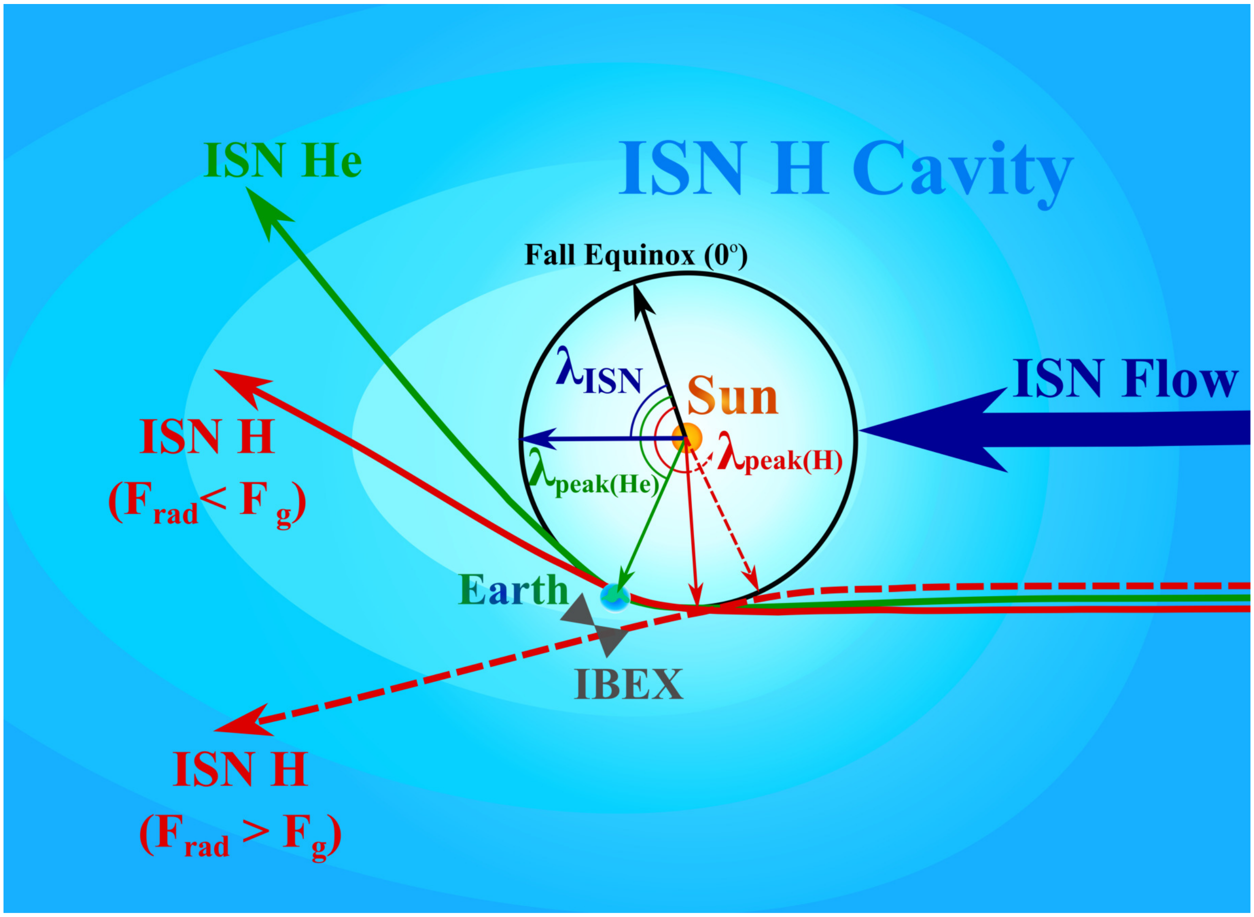

Figure 6.1 Schematic view of the trajectory of the ISN atoms, adapted from (Möbius et al., 2012). The thick blue line represents the trajectory of all ISN atoms. The green line represents the trajectory of ISN He atoms. The red lines indicate the trajectory of ISN H atoms in the case of a net attractive ($\mathbf{F}_{rad} < \mathbf{F}_g$) and repulsive ($\mathbf{F}_{rad} > \mathbf{F}_g$) force.

6.3 ISN H Distribution Function

Modeling interstellar neutral atoms observed by IBEX has played a major role in understanding the nature of the VLISM and how it interacts with the heliosphere. An analytical model of the interstellar gas was presented by Lee et al. (2012, 2015), which was basically the classical hot model tailored to model IBEX observations. Lee et al. (2012) developed an analytic model for the ISN flow based on the invariance of the distribution function along hyperbolic trajectories, assuming a stationary and axisymmetric flow. Assuming constant radiation pressure and ionization rates allows the use of the analytic relations in this model with some modification.

An attempt to combine the Lee et al. (2012) work with numerical methods to integrate over energy steps (using an empirical energy response function), collimator (using the collimator response function) and spin sector led to the analytic Full INtegration Model (aFINM). Schwadron et al. (2013) developed this model to simulate the ISN H count rates observed by IBEX. They performed a chi-square analysis to find μ as well as the characteristic parameters of the ISN H bulk flow (vector velocity and temperature) for the years 2009 to 2011. Schwadron et al. (2015, 2016a) modified the same model to successfully predict count rates for He and O and they obtained consistent bulk flow parameters for these ISN species.

The Warsaw Test Particle Model (WTPM) was developed to simulate ISN He (Bzowski et al., 2012), in which they determined a secondary population of the ISN He is necessary to fully account for the observations. The WTPM was optimized and adjusted to predict the flux of interstellar atoms observed by IBEX-Lo considering both primary and secondary populations for the ISN He (Bzowski et al., 2015; Sokół et al., 2015; Swaczyna et al., 2015). The WTPM was subsequently adapted to simulate the IBEX ISN H signal as a superposition of contributing signals from the primary and secondary populations of ISN H (Kowalska-leszczynska et al., 2018; Galli et al., 2019). A combination of a global kinetic-MHD model of the heliospheric interface and a 3D time-dependent kinetic model (based on classical hot model) of the ISN H distribution (Izmodenov and Alexashov, 2015) inside the heliosphere was used to find the ISN H flux at 1 AU observed by IBEX (Katushkina et al., 2015).

Lee et al. (2012) only considered the primary population, although the model can be expanded to secondary populations in a straightforward way, assuming they are represented by a Maxwellian distribution function. In this study, I used aFINM for a distribution function consisting of two Maxwellian functions associated with the primary and secondary H populations: where n_i, T_i, and $\mathbf{V}_i$ are the ISN H density, temperature, and bulk flow velocity for the primary or secondary population at heliospheric interface. $\mathbf{V}_\infty$ is the velocity vector of the ISN bulk flow far from the Sun. The bulk flow parameters for the primary population (see Table 6.1) were adopted from Bzowski et al. (2015) based on analysis of IBEX observations of the ISN He with the WTPM. They obtained these values for the velocity and temperature of the ISN He bulk flow parameters at the heliospheric interface, which was adopted here also for the primary ISN H. The ISN H density both for the primary and secondary populations were taken identical to those obtained by Bzowski et al. (2008), as well as the temperature and the speed for the secondary population. The inflow direction (longitude, λ, and latitude, ϕ) for the secondary ISN H, however, was adopted from Kubiak et al. (2016), which they found for the ISN He secondary population (For further details see Kowalska-leszczynska et al., 2018).

In this study I considered charge exchange and photoionization inside the heliosphere, which are the most dominant processes for the ISN H flow (Bzowski et al., 2013a). I used the Lindsay and Stebbings (2005) formula for the charge exchange cross section (For further details see Bzowski et al., 2013b). Using photoionization rates for H atoms from a model, described in Bzowski et al. (2013b), and charge exchange rates, obtained by applying solar wind proton density and speed based on Sokół et al. (2013), the total ionization rate β was calculated:

$$\beta = (\beta_{chex,1AU} + \beta_{ph,1AU})(\frac{r_E}{r})^2 \tag{6.2}$$

Both, the charge exchange rate ($\beta_{chex,1AU}$) and the photoionization rate ($\beta_{ph,1AU}$) at 1 AU are functions of time and heliolatitude. However, in our stationary model I applied values averaged over the last part of the trajectory for which the ionization rate was above $\sim 10\%$ of its values at 1 AU.

$$f = \sum_{i=prim,sec} f_i \tag{6.3}$$

$$f_i = n_i(2\pi k_B T_i/m)^{-3/2} \times \exp(- \mid \mathbf{V}_\infty - \mathbf{V}_i \mid^2 (2k_B T_i/m)^{-1}) \tag{6.4}$$

Table 6.1. Parameters associated with the ISN H distribution function (identical to those used by Kowalska-leszczynska et al., 2018).

	Primary	Secondary
n_i	0.030 cm^{-3}	0.054 cm^{-3}
T_i	7443 K	16300 K
V_i	25.784 km/s	18.744 km/s
λ_i	255.745°	251.57°
ϕ_i	5.169°	11.95°

6.4 Instrument Description

The IBEX-Lo instrument accepts neutral atoms from $\sim$ 10 eV to 2 keV (Fuselier et al., 2009). The incoming particles pass through a collimator (with a full width at half maximum of 7°) and then hit a conversion surface, where they are converted to negative ions and/or produce sputtered negative ions. Then they are selected based on their energy per charge by an electrostatic analyzer (ESA) with eight logarithmically spaced energy steps and accelerated by a post-acceleration voltage. The converted ISN H ions are predominantly observed in energy step (E-Step) 1 (15 eV center energy) and 2 (29 eV center energy), while the ISN He sputter products are distributed over the first four E-Steps (Möbius et al., 2012, Figure 1), with similar detection efficiencies in E-Steps 1-3 and starkly reduced in E-Step 4. The energy response function for each of the energy steps for different species is obtained empirically as a normalized transmission function, $T(E)$, based on its central energy (E_c) and a FWHM $\Delta E/E = 0.7$ (Fuselier et al., 2009), resulting in respective maximum and minimum energies (E_{Max} and E_{Min}), multiplied by a constant geometric factor for each E-Step and species:

$$T(E) = \exp(-4\ln 2\frac{(E/E_c - 1)^2}{\Delta_1^2}), \text{for} E \leq E_c \exp(-4\ln 2\frac{(E_c/E - 1)^2}{\Delta_2^2}), \text{for} E > E_c \tag{6.5}$$

This energy transmission function is from Schwadron et al. (2013), where $\Delta_1 = 2(1 -$

Table 6.2. H transmission function essential parameters for E-Step 1 and 2.

E-Step	E_c (eV)	E_{min} (eV)	E_{max} (eV)	G (cm^2 sr keV/keV) before PAC voltage change	G (cm^2 sr keV/keV) after PAC voltage change
1	15	11	21	$7.29 \times 10^{-6} \times 0.93$	$7.29 \times 10^{-6} \times 0.435$
2	29	20	41	$1.414 \times 10^{-5} \times 0.93$	$1.414 \times 10^{-5} \times 0.435$

E_{min}/E_c) and $\Delta_2 = 2(1 - E_c/E_{max})$. They fitted a Gaussian function to laboratory calibration data (see Schwadron et al., 2013; Park et al., 2016). The geometric factors are obtained by multiplying the absolute geometric factor, the energy resolution of the energy steps, and the conversion efficiencies (see Schwadron et al., 2009; Park et al., 2016). For H atoms, the geometric factor of the E-Step 2 is almost twice that of E-Step 1 (see Table 6.2), leading to higher count rates predicted for E-Step 2 than E-Step 1 (at least in model predictions, for the expected range of the parameter μ). These values are obtained based on calibration data for a neutral hydrogen beam in the laboratory.

Figure 6.2 shows the energy range of the ISN H distribution at 1 AU (for $\mu = 0.9$ and 1.1) along with the normalized transmission functions of the first two energy steps. Since the distribution peak of ISN H falls between the two energy channels, its signal is very sensitive to the variation of solar parameters and calibration coefficients of the instrument.

6.5 Data Selection

To separate ISN H from He, Schwadron et al. (2013) applied a subtraction method by using the ratios of the count rates for E-Step 1/ E-Step 3 and E-Step 2/ E-Step 3 at the peak of the primary interstellar He (ISN He) flow. They assumed the same fraction is still valid during later orbits, where the ISN H flow is dominant (and secondary He is still present), to subtract the sputtered H^- ions produced by the ISN He flow. To obtain more reliable H counts, Galli et al. (2019) used a bootstrap method to calculate the ISN He intensity from the H^- count rate in E-step 3 for each map pixel, based on the rationale that the ISN H

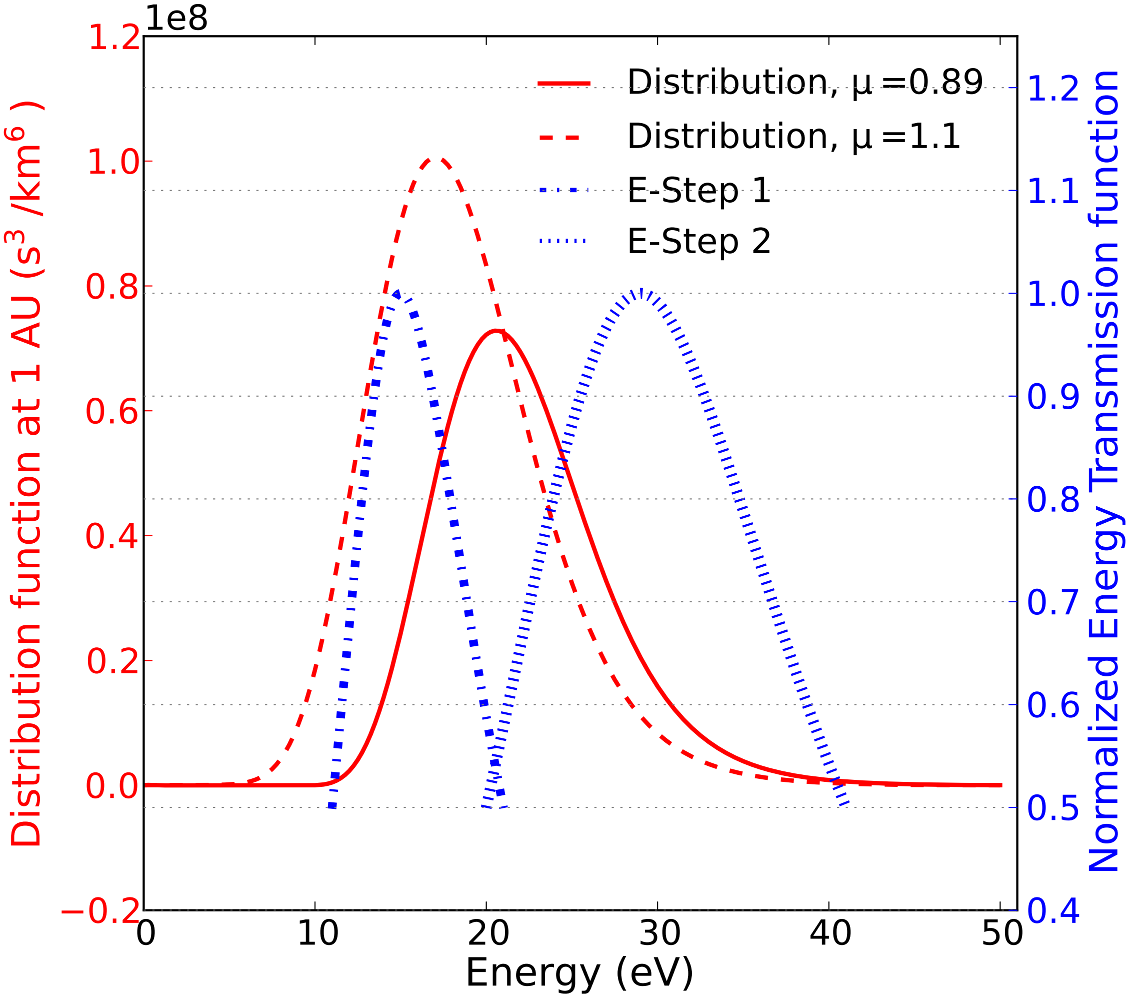

Figure 6.2 Distribution function of ISN H flow in IBEX-inertial frame at 1 AU (for orbit 23 in 2009) is shown in red solid line for $\mu = 0.89$ and in red dashed line for $\mu = 1.1$. The normalized energy transmission function for E-Step 1 is shown in blue dash-dotted line and for E-Step 2 in blue dotted line. As can be seen here, as μ increases the distribution function moves towards lower energies and the E-Step 1/ E-Step 2 ratio increases.

(with energies below 40 eV) does not contribute to the count rates from E-Step 3. Then they ascribed the excess H^- count rates registered in the first two energy steps to ISN H. For the conversion between the He intensity and the H^- count rates, they used conversion factors from laboratory calibration (so-called "H3-lab" approach) as well as factors derived from in-flight observations (the "H3-inflight" approach). In addition, they applied another bootstrap method ("H2O2-inflight"), where they calculated the ISN H intensity in the first two energy steps by using empirical $H^-/\ O^-$ ratios for sputtered H^- versus sputtered O^- count rates in each energy step. Lowering the post-acceleration voltage in 2012 resulted in lower sensitivity to Oxygen. As a result, the H2O2 method can only cover the years 2009-2012, for which O^- maps are available. These three methods were implemented by Galli et al. (2019) and confirmed that the basic findings of Saul et al. (2012, 2013) and Schwadron et al. (2013) regarding the ratio of ISN H measured in E-Step 2 and E-Step 1 do not depend on the retrieval method.

Using a statistical analysis, Galli et al. (2019) also showed that the differences between H3-inflight and H3-lab retrieved ISN H are negligible for E-Step 1. The differences between the H2O2-inflight retrievals and the first two approaches are larger, but still fall within the uncertainties. Using this analysis they demonstrated the coherence of their three approaches for E-Step 1. In this study, our focus is on the temporal shift in the ISN H distribution. Therefore, I used H3-inflight retrieved data for E-Step 1 ISN H fluxes, as it provides credible fluxes for almost an entire solar cycle.

6.6 Shift of the ISN H peak longitude over time

In this work I used the ISN H data released by Galli et al. (2019) (details in Section 6.5) at E-step 1, with one data point per orbit resolution, to find the ecliptic longitude at which the peak of the ISN H signal was observed (λ_{peak}). This λ_{peak} is calculated starting from the fall equinox as shown in Figure 6.1, where λ represents the ecliptic longitude of IBEX at the time of observation. To find λ_{peak} I fitted a Gaussian to the observations for each year using a chi-square technique. In this study I focused on spin sectors 14 and 15 corresponding to 84° and 90° (the center of the spin bins from the north ecliptic pole, NEP) $\pm 3°$, which show the peak of the distribution in latitude, to take advantage of the higher counts in these two spin sectors. Since the count rates reported for E-Step 1 are more distinguishable, typically one order of magnitude larger than E-Step 2, I concentrated on E-Step 1. Figure 6.3 shows an example of this analysis for the ISN H season in 2011.

I used our model (aFINM) to find the parameter μ for which both the model-predicted and observed ISN H signal peak at the same longitude. To this end I applied the same chi-square technique to fit a Gaussian to model predictions and find the peak longitude. I run this analysis with varying μ in iterations to reach the same peak longitude from observations for each season, obtaining an effective μ for that season. Figure 6.4, as an example, compares the signal observed with IBEX to our model predictions for the 2011 ISN H season. The green dots in this figure represent the ISN H count rates predicted for the IBEX-Lo observation using aFINM for the observation times list provided by Galli et al. (2019). The Gaussian, however, was fit to the black circles, which are averaged over the observation times for each orbit, to be compared with one data point per orbit data (red circles in this figure).

I repeated the same analysis for each year from 2009 to 2018, excluding 2015 and 2016 (see first two panels of Figure 6.5). In 2015 the solar activity is at its peak, resulting in the weakest ISN H signal with no statistically significant count rates. Due to a different energy stepping scheme of IBEX-Lo the ISN H could not be extracted in the way described for 2016 (see Galli et al., 2019, for more detailed explanations). Since there are too few data points for 2013 and 2014 with values above the background (Galli et al., 2017) to allow a chi-square analysis, I simply used the one highest data point as the peak of the signal for those two years. The cross signs with huge error bars in panel 1 and panel 2 of Figure 6.5 are used to differentiate between those two years and the rest of the years for which a chi-square analysis is performed.

In spite of substantial uncertainties and several years for which we have no or unreliable data, a possible correlation is evident in Figure 6.5. The peak longitude (top panel, blue circles and orange triangles with error bars) and in turn the predicted parameter μ (middle panel, red circles and green triangles with error bars) appear to increase for 2009 to 2012. The increase persists in 2013-2014 in accordance with the solar activity. Although the high radiation pressure and ionization rates lower the ISN H signal almost down to the background level, the very faint signal seems to have shifted towards larger peak longitudes for these two years. In 2017, after two years of absense of operational data, due to high radiation pressure and ionization rates in 2015 and a different energy stepping scheme of IBEX-Lo in 2016, the signal returns and shows a decreasing peak longitude in two consecutive seasons in accordance with the declining solar activity. In the middle panel of Figure 6.5, the $\mu_0 = \mu(v_r = 0)$ parameter from Kowalska-Leszczynska et al. (2018) (black line) demonstrates the same trend although with more pronounced variations between different phases of solar activity. To better illustrate the effect of the Lyα radiation on the observed shift in the peak longitude the total irradiance is also shown in the bottom panel of Figure 6.5.

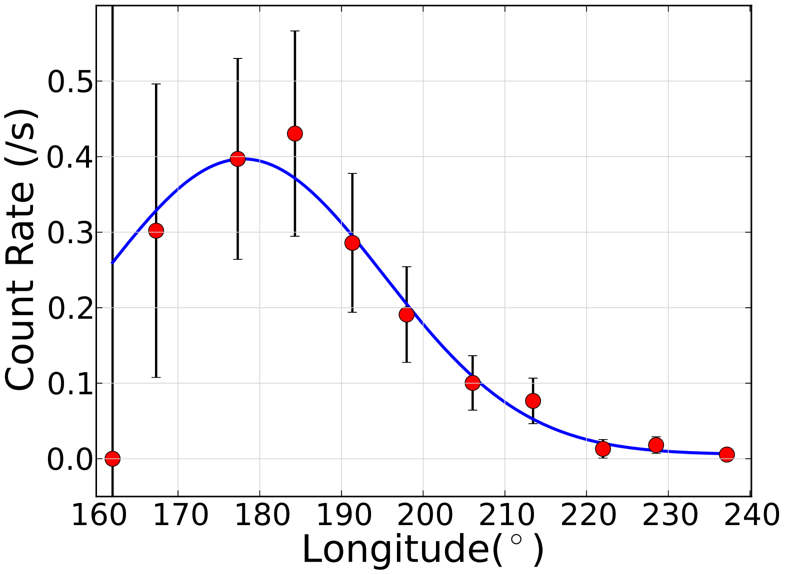

Figure 6.3 A Gaussian function fitted to ISN H observed count rates in IBEX-Lo E-Step 1 (spin sector 14) using a chi-square scheme for 2011.

6.7 Discussion

Early records of direct ISN H measurements showed an increase in the peak longitude from 2009 to 2012 as the solar activity was increasing (Saul et al., 2013). They fitted a Gaussian to accumulated counts per three hours in E-Step 1 to find the longitude of the peak flux for each year. Based on the physical model we expect this increase, since an increase in μ

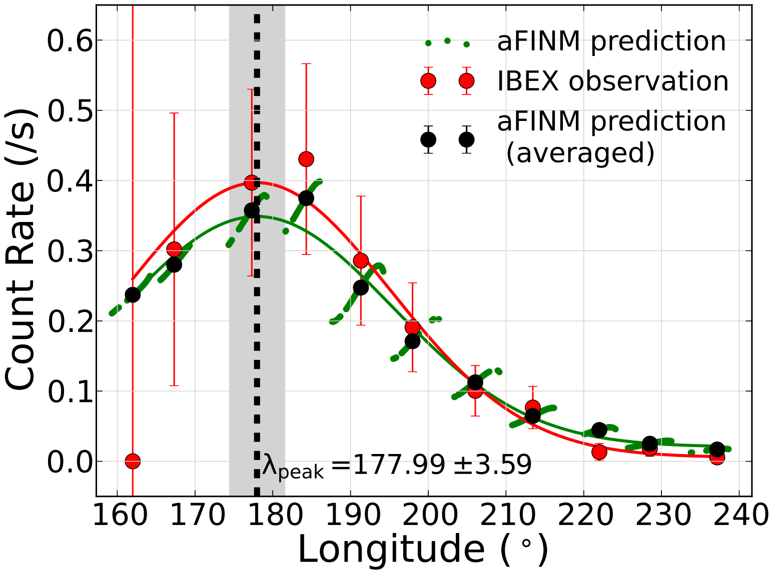

Figure 6.4 Model predictions based on aFINM for ISN H in 2011 is compared to observations (E-Step 1, spin sector 14). The green dots shows the ISN H count rates model predictions for the observation times list provided by Galli et al. (2019). The green line is a Gaussian fit to the black circles, which are aFINM predictions, averaged over the observation times. The red circles represent ISN H count rates observed by IBEX.

translates to either a weaker net attractive force ($\mu < 1$), which means the atoms are bent toward the Sun at larger λ_{peak} or a repulsive force ($\mu > 1$) that deflects the neutral atoms much earlier in their orbits (even larger λ_{peak}).

Despite expecting a shift in λ_{peak} with varying solar activity, a significant trend was not observed from 2009 to 2012 ISN H data by Galli et al. (2019), using H2O2 retrieved data. The lack of identifying the expected trends in the ISN H data can be attributed to high ISN He intensity, low ISN H intensity (particularly during years of high solar activity), and limited spatial resolution. In my analysis, I used H3-inflight retrieved data for E-Step 1, which covers almost an entire solar cycle and shows a more significant longitudinal shift for the ISN H peak. I used these data since our focus is on the evolution of the spatial distribution with solar activity. The H3-inflight data spanning almost a complete solar cycle enables us to investigate the longitudinal shift of the ISN H peak through varying phases of solar activity.

The parameter μ that I obtain in this analysis is based on finding the same peak longitude with IBEX-Lo observations as explained in Section 6.6. In this way we do not need to incorporate any physical model for the parameter μ and its dependence on time, radial speed, or helio-latitude. μ in this analysis is an input parameter in our model, which is stationary since our model only permits constant values. μ as found in this way may be taken as an effective μ for each observation season.

However, ISN H atoms are on their journey to the inner heliosphere for about 20 years and experience almost two full solar cycles. As a result, variations of the radiation pressure with time and radial speed can play an essential role during the journey of H atoms from outside the heliosphere to 1 AU, challenging stationary models. Tarnopolski and Bzowski (2009) compared the WTPM model predictions for ISN H density between a flat radiation profile (i.e., no radial speed dependence of μ) and a non-flat profile for equivalent Lyα intensities and showed that the differences are quite substantial at 1 AU. More recently, Kowalska-leszczynska et al. (2018) applied a newer model of the radiation profile (Kowalska-Leszczynska et al., 2018) and showed that the differences between the predictions of these two models are significant, concluding that the ISN H signal observed by IBEX is sensitve to radiation pressure variations with radial velocity.

This raises doubts if we need to account for an integral of the radiation pressure affecting the trajectory, but in Chapter 7 I justify the use of a stationary model, showing that the net force acting on ISN H atoms is negligible until the last few months of their travel. As a consequence, ISN H atoms travel on straight lines until they get close enough to the Sun. Then the hyperbolic characteristics of the trajectories become important, bending them inward or outward depending on the current phase of the solar activity as shown in Figure 6.6.This suggests that an effective parameter μ appropriately averaged over the last phases of their journey can address the effect of the radiation pressure on the ISN H trajectory. The absence of a time lag between the solar activity phase and variations in ISN H intensity reported by Galli et al. (2019) also confirms that the effect of radiation pressure and loss processes becomes most important close to the Sun, and an integration of these effects over the entire trajectory is not necessary[1].

The qualitative agreement between μ_0 from Kowalska-Leszczynska et al. (2018) and the effective μ obtained in this analysis (middle panel of Fig. 6.5) may indicate that these two parameters are tightly connected. To investigate this further, I illustrate μ_{eff} (from this study) along with μ_0, $\mu(v_r$=-25 km/s, minus sign means toward the Sun), and $\mu(v_r$=-35 km/s) based on Lyα profile (Kowalska-Leszczynska et al., 2018) in Figure 6.7. As can be seen in this figure, the best agreement is found between μ_{eff} and $\mu(v_r$=-35 km/s). However, it is very unlikely that the majority of ISN H atoms have an average radial velocity close to -35 km/s in the last phases of their journey. In particular, as detailed in Chapter 7, at small helio-radii, where the radiation pressure becomes important, the radial velocity decreases dramatically. For an ISN H atom, starting at 100 AU with ISN bulk velocity, the weighted average of v_r in the last six months of the travel is about -17.62 km/s. Since this value falls into the flat part of the radiation profile, as explained further in Chapter 7, μ_0 is a good approximation for the effective μ acting on the H atoms. In conclusion, the difference between the μ_{eff} obtained in this analysis and any μ from Lyα-based models is inherent and most probably associated with absolute calibration of Lyα line profiles.

There is an evident linear correlation between the total Lyα irradiance and the central irradiance of solar Lyα profile, and μ_0 as a result (see Figure 7 from Lemaire et al., 2015). To further investigate the effective parameter μ from my analysis, I illustrate its correlation with the total Lyα irradiance in Figure 6.8. The μ_0 in this figure was calculated based on the total Lyα irradiance averaged over the two Carrington cycles right before the ISN H season in that year, to provide the best estimate for the effective radiation pressure that ISN H atoms experience (see Chapter 7). The linear fit (purple line, $\mu_{eff} = (0.27 \pm 0.03) I_t + (0.03 \pm 0.10)$)

---

[1] The time lag between radiation pressure variations and resulting variations in the ISN H helioglow at $\sim$ 1 AU was shown to exist by Bzowski et al. (2002). However, they showed that it was at its minimum value in the upwind direction.

to μ_{eff} (blue circles with error bars for spin sector 14 and red circles with error bars for spin sector 15) is compared with μ_0 (green line, $\mu_0 = (0.35 \pm 0.001)I_t - (0.46 \pm 0.005)$). The green shaded area indicates the uncertainty region for μ_0 based on a 15% uncertainty estimated for observed Lyα line profiles (Lemaire et al., 2015; Kowalska-Leszczynska et al., 2018). The shaded uncertainty regions overlap for these two lines, indicating an agreement between μ_{eff} based on ISN H data observed by IBEX and μ_0 from Lyα data, despite the steeper slope for μ_0. This might suggest that during years of low solar activity when radiation pressure is less effective in decelerating ISN H atoms, atoms from the faster wing of the ISN H distribution are not decelerated enough to fall in the flat part of the Lyα line profile so that μ_{eff} deviates from μ_0. Another possible explanation is a systematic over-subtraction of ISN He in ISN H retrieval methods (Section 6.5), which shifts the peak longitude toward later orbits. This over-subtraction would affect the ISN H flux more dramatically during years of solar minimum since there is a wider overlap between ISN H and He signals in those years. The black dashed line in Figure 6.8 is obtained by fitting a line to μ_{eff} assuming the same slope as for μ_0 to find the intercept (-0.24 ± 0.01). The 0.22 ± 0.014 difference between the green line and dashed black line intercepts could be indicative of absolute calibration issues with Lyα line profiles.

Katushkina et al. (2015) found a qualitative difference between their predictions and IBEX data. They found that contrary to the IBEX data, their model results obtain higher rates for E-Step 2 than E-Step 1, in the expected range of radiation pressure and ionization rate. The same discrepancy has been reported for all existing models described in Section 6.3 in the expected range of radiation pressure and ionization rate (e.g. see Katushkina et al., 2015; Galli et al., 2019). Such discrepancy limits the analysis of the intensity of the ISN H signal although it does not affect the longitudinal shift of its peak. This discrepancy could be associated with a poorly known energy response function, uncertainties in the total irradiance data, over-subtraction of ISN He in E-Step 2 in data retrieval methods from previous work, or some physical aspects being neglected in our current models.

A chi-square analysis to obtain the best fit between model-predicted ratio of fluxes in the two energy channels with IBEX data showed that the most important parameter affecting this ratio is the radiation pressure (Katushkina et al., 2015). Also, as can be seen in Figure 6.2, since the distribution peak of the ISN H at 1 AU falls between the two lowest E-Steps, its signal is very sensitive to solar cycle variations. More specifically, variations in μ move the distribution function observed at 1 AU in energy, and thus change the flux ratio between E-Step 1 and E-Step 2. This suggests that this qualitative difference between model predictions and IBEX data could be related to the absolute calibration of the radiation pressure at least in part.

Another explanation for the remaining discrepancy might be a retrieval bias against ISN H in energy step 2 or an unexpected behaviour of the energy response function in-flight compared to laboratory calibration. As detailed in Section 6.5, Galli et al. (2019) have developed three different retrieval methods to derive ISN H intensity more accurately. Their obtained ratio between the two E-Steps confirms previous reports (Schwadron et al., 2013; Saul et al., 2013) and thus excludes over-subtraction of the ISN He in E-Step 2 as a possible explanation for the aforementioned discrepancy. However, a systematic over-subtraction of ISN He in both E-steps might still have caused the less noticeable variations of μ_{eff} in comparison with μ_0 (smaller slope of purple line compared to green line in Figure 6.8) by eliminating the actual peak for the years of low solar activity. This can be a plausible explanation since an over-subtraction of ISN He is expected to affect E-Step 2 more substantially than E-Step 1, leading to the previously mentioned discrepancy.

The poor knowledge of the IBEX-Lo response function for ISN H is likely due to a different behavior of IBEX-Lo in space than in laboratory calibrations at energies below 50 eV. At such low energies, surface science effects play a significant role in the scattering and ionization of particles. The conversion surface might have become chemically contaminated during launch, and this contamination has become permanent because it was burnt in by UV light early in the mission (Riedo et al., 2010) and/or because of chemical reactions with the surface (hydrazine). This has possibly led to a different surface coating on IBEX-Lo, which is stable over the years but deviates from laboratory conditions. In the future we plan to perform a comprehensive investigation of the energy channels, their associated response functions to the ISN H signal, and how improving them affects the ISN H count rates, including information from the in-flight performance in response to ISN H. In our future work we will also focus more on the latitudinal profile of the ISN H signal, as the narrower ISN He distribution cannot contaminate it (Galli et al., 2019).

Since the beginning of the IBEX mission, comparing models (briefly discussed in Section 6.3) against IBEX-Lo observed fluxes for the ISN H, He, and O was used to find the essential parameters associated with the ISN flow, most importantly for the ISN He flow, which is least affected by ionization losses due to its high ionization potential. For H atoms, the radiation pressure was also investigated in this way. Fitting aFINM to 2009-2011 data obtained a slightly increasing μ from 0.94 ± 0.04 in 2009 to 1.01 ± 0.05 in 2011 (Schwadron et al., 2013). A combination of the global heliospheric interface model and the ISN H distribution inside the heliosphere, limited to orbit 23 of IBEX (2009) obtained $\mu = 1.26^{+0.06}_{-0.076}$ (Katushkina et al., 2015). Although their obtained parameter was much larger than $\mu_0 = 0.89$, derived from the integrated solar Lyα irradiance, the first report of the direct detections of the ISN H had already predicted a parameter μ larger than unity for 2009-2010 (Saul et al., 2012).

Investigating variations in the ISN H intensities and its longitudinal shift throughout different phases of the solar cycle can certainly be beneficial in resolving the absolute calibration issue of the radiation pressure. In the present study, I focused on the longitudinal shift of the ISN H signal due to the aforementioned discrepancy between all existing models and the signal observed by IBEX. I created a methodology to find yearly estimates of effective radiation pressure. I found the effective parameter μ increasing from values as low as $0.94^{+0.12}_{-0.12}$ during the cycle 23 minimum (for spin sector 15 in 2010) to values as high as $1.29^{+0.04}_{-0.04}$ (for spin sector 14 in 2012) during the cycle 24 maximum and then decreasing again to $0.996^{+0.043}_{-0.040}$ (for spin sector 14 in 2017), averaging at 1.074 ± 0.038 through the full solar cycle. These results based on IBEX data demonstrate, for the first time, a qualitative agreement (as well as a quantitave agreement, within the uncertainties) with simulations of Ly profile based on the total irradiance observations. However, the parameter μ from our analysis averaged over cycle 24 is $\sim 21\%$ larger than an average of μ_0 from (Kowalska-Leszczynska et al., 2018) over the same time interval. The continuation of this type of analysis along with the ISN H observations with IBEX-Lo, particularly as we are heading toward a solar minimum in the next few years, will play an essential role in understanding the ISN H flow distribution function as well as the radiation pressure and ionization processes to which it is subjected.

6.8 Summary and Conclusion

While the ISN flow has been studied extensively through sophisticated modeling and comparing results with IBEX data, most of these studies have focused on ISN He. The radiation pressure, with its temporal and spatial variations, and more effective ionization processes complicate the analysis of ISN H flow. So far this problem has been addressed in a limited number of studies (Schwadron et al., 2013; Katushkina et al., 2015).

A new release of ISN H comprehensive maps observed by IBEX (Galli et al., 2019), which showed the reappearance of the signal after the solar maximum of cycle 24, motivated us to revise aFINM and to compare its results with IBEX observations throughout the past 10 years. Although the ongoing discrepancy in the ratio of the ISN H counts in the lowest two energy channels between all available models and the observations makes it difficult to gain information from the signal intensity, the longitudinal shift is still a reasonable indicator of the ISN H signal variations with solar activity.

Based on our current physical understanding of the ISN H flow, we expect a shift in the peak longitude that increases with solar activity. The expected shift, however, currently still carries large uncertainties. This could be most likely due to very low intensities of the ISN H, large uncertainties especially during years of high solar activity, poorly known response functions of the instrument for such low energy, over-subtraction of ISN He in both E-Step

1 and 2, or some of the physics of the problem being neglected in our current models. In spite of the large uncertainties, not only is the anticipated shift observed, but also the effect suggests that the radiation pressure generally exerts a larger force than gravity. The trend that we observe here and the fact that it agrees qualitatively with total irradiance intensities and the parameter μ obtained from an independent model indicate that a better-known response function of the instrument or higher resolution data could lead us to observe the predicted shift and even more confidently address the calibration issue with the absolute irradiance of solar Lyα fluxes. Further study of the IBEX data and the instrument response to H atoms will help to refine our understanding of solar radiation pressure and its effect on ISN H distributions.

The current anomalously low solar activity indicates that we may be entering a period of persistent decline in the heliospheric magnetic field (Rahmanifard et al., 2017). Selected for launch in 2024, the Interstellar Mapping and Acceleration Probe (IMAP) will provide an opportunity to track the interaction between the heliosphere and the VLISM through these years of unprecedentedly low solar activity (McComas et al., 2018). IMAP will address our ongoing issues with detecting the ISN H signal and its essential features including the expected peak longitude shift through: improving time resolution, increasing angular coverage, increasing sensitivity, and better suppressing the background (Schwadron et al., 2016b).

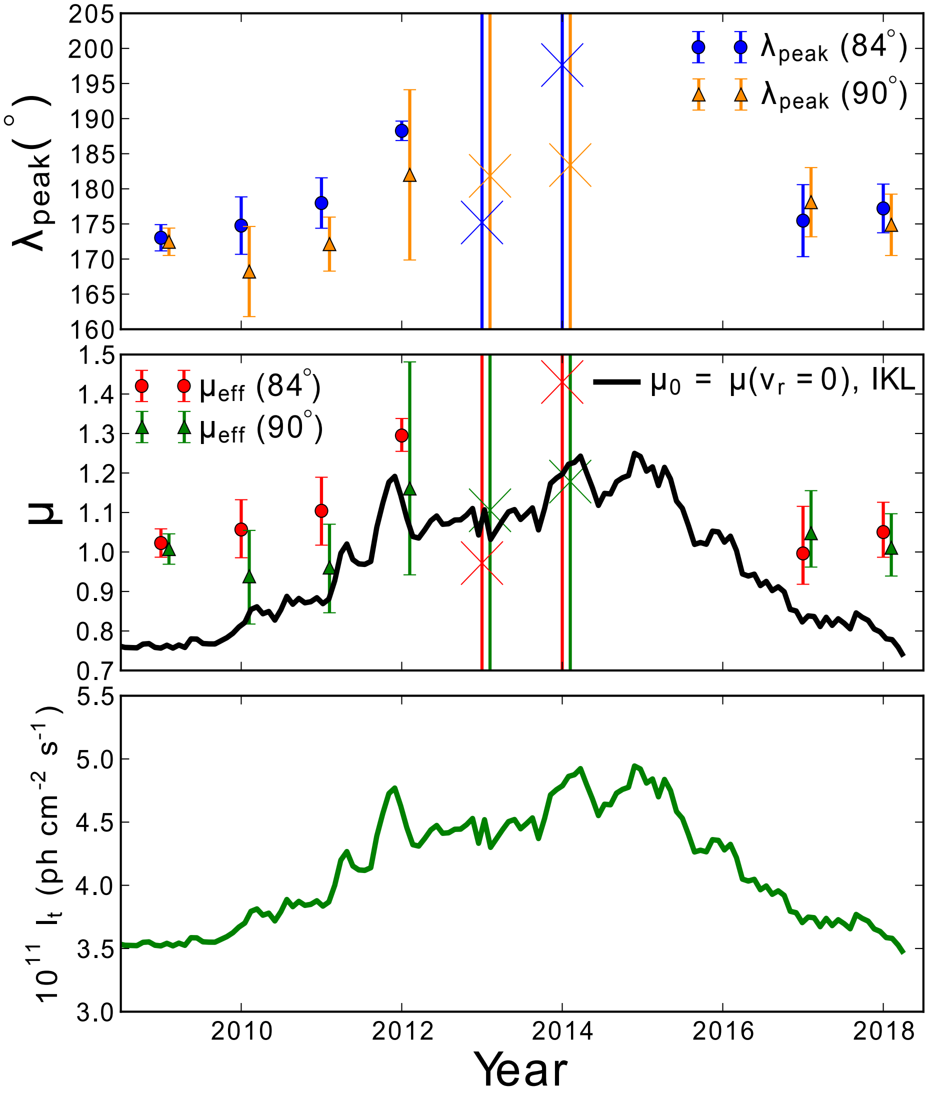

Figure 6.5 **Top panel** ISN H flow peak longitude obtained by fitting Gaussian functions to observed ISN H count rates. Blue circles (orange triangles) with error bars show the ISN H flow peak longitude for spin sector 14 (15) corresponding to a 6° bin with center of the bin at 84° (90°) from NEP. Cross signs belong to the 2013 and 2014 seasons, for which very few data points above the background are available. I excluded these years from our chi-square analysis and used the highest data point as the peak of the signal. **Middle panel** The parameter μ that yields the best agreement between ISN H peak longitude from observation (top panel) and aFINM predictions in red circles (green triangles) with error bars for spin sector 14 (15) is compared with μ_0 (corresponding to the center of profile) from the model (IKL) by Kowalska-Leszczynska et al. (2018), which is based on total irradiance (black line). **Bottom panel** Total irradiance from the composite solar Lyα flux data from LASP, integrated between 121 to 122 nm. Since the radial velocity of ISN H atoms close to 1 AU drop to values close to zero, μ_0 can be used as a proxy for the effective radiation pressure that these atoms experience.

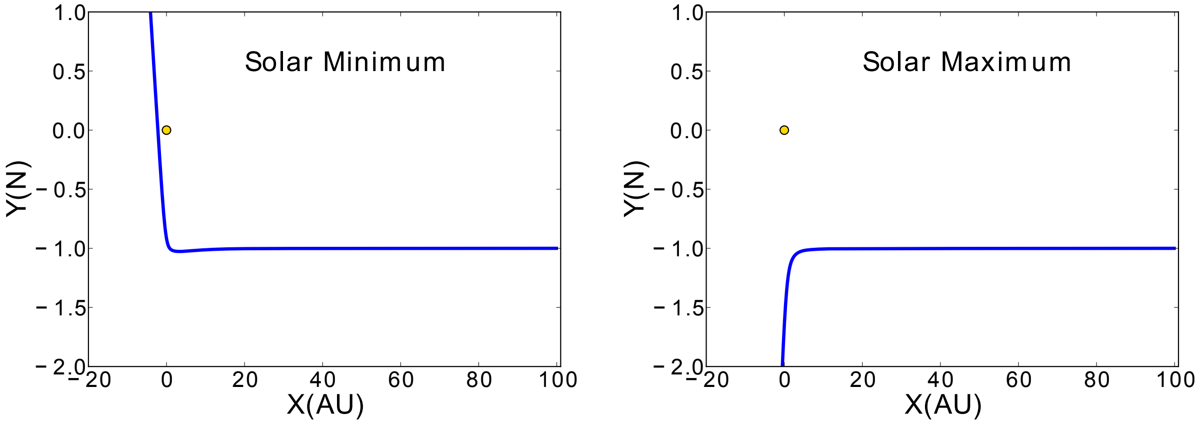

Figure 6.6 ISN H atoms trajectories are shown for two cases. The yellow circles in both panels represent the Sun. In both panels the H atom travels on a straight line far from the Sun. **Left** The H atom reaches 1 AU while the Sun is transiting to a solar minimum. As a result, the trajectory of the H atom can be approximated by a hyperbola that is bent inward, although it inclines a bit outward in the beginning. One should note that this outward inclination is practically negligible as the scales are not the same for X and Y axes. **Right** The H atom reaches 1 AU at solar maximum and bends outward as a result of the repulsive net force.

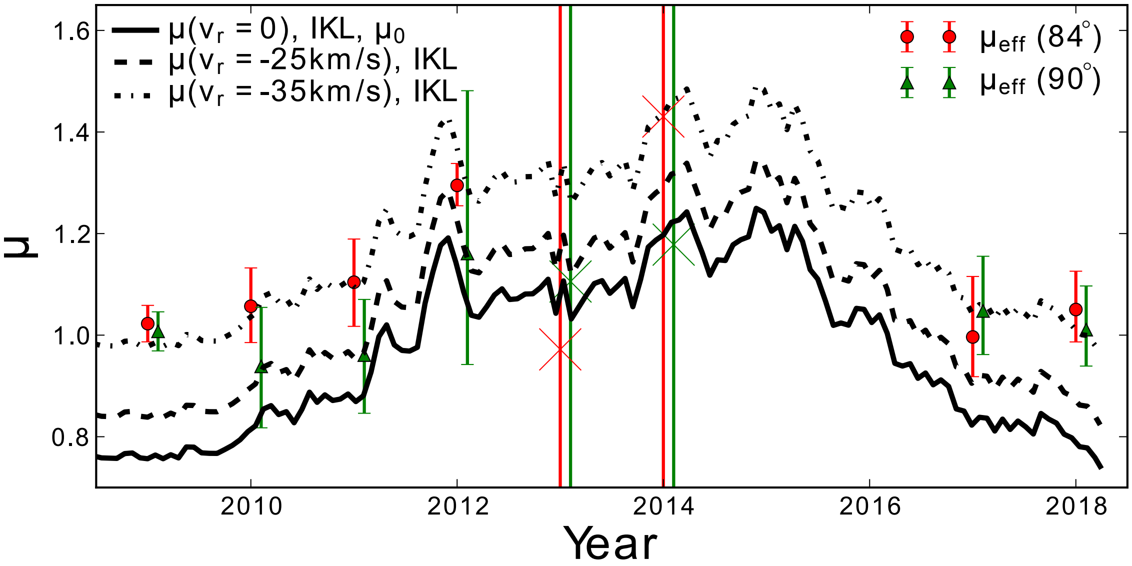

Figure 6.7 The (μ_{eff}) obtained from our analysis (red circles with error bars for spin sector 14 and green triangles with error bars for spin sector 15) is compared with μ_0, $\mu(v_r$=-25 km/s), and $\mu(v_r$=-35 km/s) from Kowalska-Leszczynska et al. (2018, IKL). While we expect a quantitative agreement between μ_{eff} and μ_0 from IKL (See Chapter **??**), μ_{eff} is closest to $\mu(v_r$=-35 km/s).

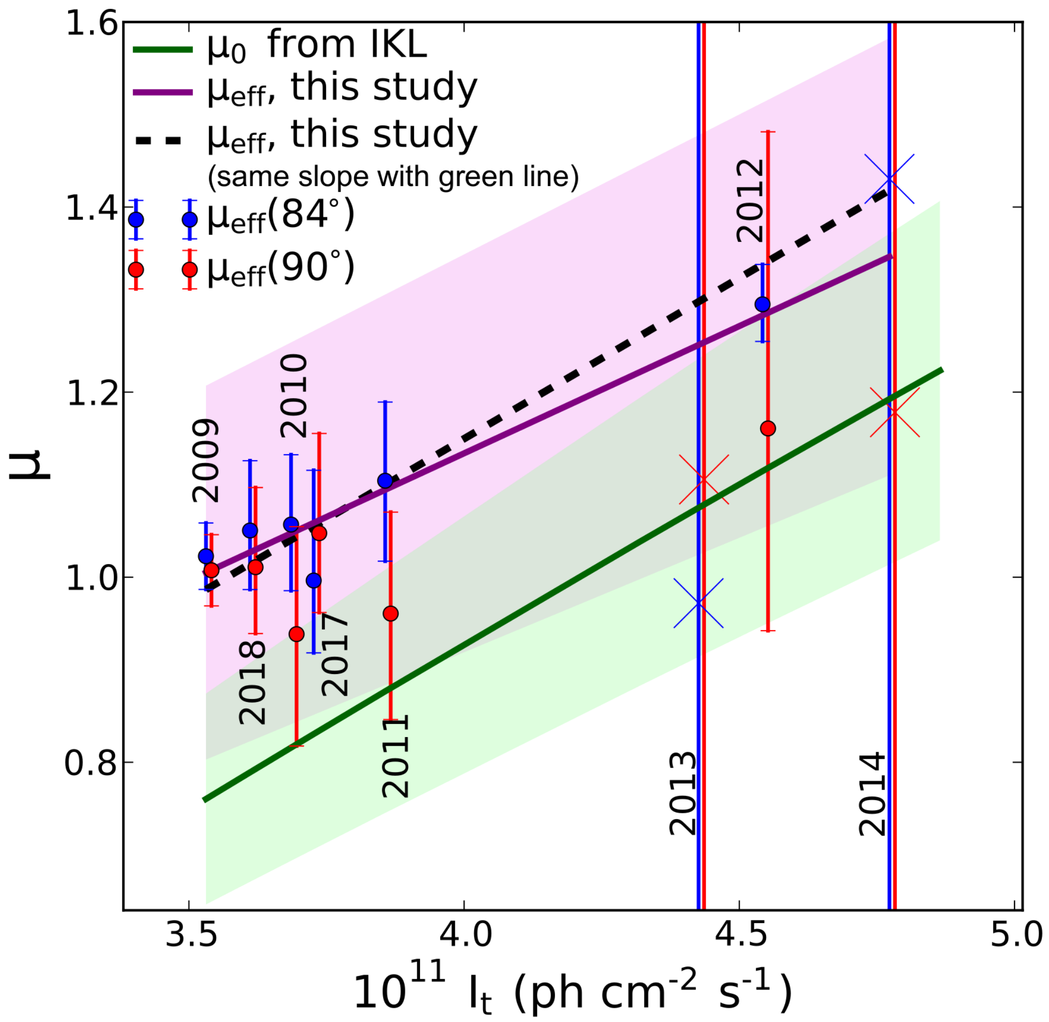

Figure 6.8 The (μ_{eff}) obtained from our analysis (blue circles with error bars for spin sector 14 and red circles with error bars for spin sector 15) versus total irradiance from LASP data, integrated between 121 to 122 nm and averaged over two Carrington cycle before the ISN H season for each year. The linear relationship between μ_0 from Kowalska-Leszczynska et al. (2018) (μ_0 from IKL) and total irradiance is shown by the green line with an estimated 15% uncertainty (green shaded area). The purple line shows a linear fit to all μ_{eff} points from our analysis for sectors 14 and 15 using a chi-square scheme, with the purple shaded region indicating the uncertainty. In addition to the evident non-zero slope of this line, which demonstrates a correlation between μ_{eff} and total irradiance and thus adds credibility to our analysis, the overlap of the uncertainty regions presents a quantitave agreement never reported previously based on IBEX data. However, the smaller slope of the purple line in comparison with the green line indicates that variations with total irradiance are less noticeable in μ_{eff} than in μ_0 from IKL. The black dashed line shows a linear fit to μ_{eff} points using the same slope from μ_0 (green line) to find the intercept using a chi-square scheme. The 0.22 ± 0.014 difference between intercepts of these two lines can be associated with the absolute calibration issue of Lyα line profiles.

CHAPTER 7

Variations of the Radiation Pressure with Time and Radial Velocity (Study 3)

The radiation pressure is an outward force in the radial direction exerted on the ISN H atoms due to resonant absorption and re-emission of solar Lyα. The radiation pressure roughly compensates for solar gravity, which prevents significant gravitational focusing of ISN H atoms. Therefore, a longitudinal shift of ISN H is reported with respect to ISN He. Moreover, the temporal variations of the radiation pressure at different stages of solar activity are expected to cause a signal shift for each season. The parameter ($\mu = \mid \mathbf{F}_{rad} \mid / \mid \mathbf{F}_g \mid$) is a function of time (t), radial speed (v_r) and heliolatitude (θ). The dependence of μ with respect to v_r reflects the shape of Lyα profile (Figure 7.1). An ISN H atom with a radial velocity v_r absorbs Lyα photons which match the $\lambda \sim 121.567$ nm after being Doppler shifted in the reference frame of the ISN H atom.

Previous estimations of μ based on ISN H IBEX observations yielded unexpectedly high values (Saul et al., 2013; Katushkina et al., 2015). To address these high values, Kowalska-Leszczynska et al. (2018) modeled the solar Lyα profile based on observations from SUMER/-SOHO (Lemaire et al., 2015). Their model predicts three functions featuring different elements of the profile. Their model consists of a kappa function featuring the main emission line produced in the chromosphere, a negative Gaussian function featuring the absorption in the transition region, and a linear function featuring the spectral background. Figure 7.2 shows the averaged radiation profile over one Carrington rotation (using total irradiance, integrated between 121 to 122 nm, from LASP) during ISN H observation season in 2009, 2012, and 2017. The profiles in this figure clearly show the distinction between the μ values at different phases of the solar activity.

The effects of using such a model on the ISN H IBEX observations and their interpretation were studied in a more recent paper (Kowalska-leszczynska et al., 2018). The integrated irradiance used in Kowalska-Leszczynska et al. (2018) is based on observations from SUMER/SOHO with daily resolution. However, proxies are used to fill the occasional gaps. UARS/SOLSTICE (Woods et al., 1995, 2000) data are used for the absolute calibration and observations from other sources are scaled to this calibration. An estimated $\sim 15\%$ uncertainty has been suggested for the total uncertainty of the observed profiles (Lemaire et al., 2015; Kowalska-Leszczynska et al., 2018). However, the absolute calibration of the integrated Lyα irradiance and its effect on the predicted Lyα radiation profile has remained an issue.

To investigate the effect of the radiation pressure on ISN H trajectories and their observed peak longitude at 1 AU, I used the Kowalska-Leszczynska et al. (2018) model. ISN H atoms are on their journey from the edge of the heliosphere to 1 AU for about 20 years. Thus, they are subject to temporal variations in the radiation pressure at different phases of the solar activity, which might potentially overcomplicate the analysis. However, the radiation force ($\mathbf{F}_{rad}$) is proportional to $1/r^2$ as the UV photons flux. Therefore, the net force acting on the ISN H atoms (Eq. 1) is almost zero (i.e. they travel on a straight line) until they get very close to 1 AU during the last few months of their journey. This means that a stationary model using μ values averaged over the last few months prior to the observation of ISN H atoms by IBEX can produce adequately accurate results.

Over the last few AU of the ISN H atoms trajectory, they are finally accelerated (or decelerated) by the attractive (or repulsive) net force. At this point, however, the radial speed of the particles drops to values close to zero, where they experience a parameter μ close to μ_0 with the least variations. The flat part in the center of the radiation profile (Figure 7.2) is the only part of the profile that ISN H atoms are effectively exposed to, and thus μ_0 is a good proxy for the effective μ, which also supports the use of a stationary model.

To better understand the effect of the radiation pressure on the ISN H trajectory I simulated the speed, trajectory, parameter μ, and the net force acting on an ISN H atom, which travels towards the inner heliosphere at a speed of 25 km/s at 100 AU. I used the Kowalska-Leszczynska et al. (2018) model for μ (considering its temporal and radial speed dependence). Assuming that this particle starts in 1998 at 100 AU, the parameter μ and as a result the force acting on this particle are shown in the middle panel of Figure 7.3. As can be seen for the last few AU (last two months) where the net force becomes substantial, the radial velocity component falls dramatically, and μ approaches μ_0 very closely (bottom panel of Figure 7.3). Therefore, the atom trajectory can be treated as a hyperbola with a constant μ_0. Because at this point solar minimum conditions are reached, the ISN H atom is deflected toward the Sun (top panel of Figure 7.3).

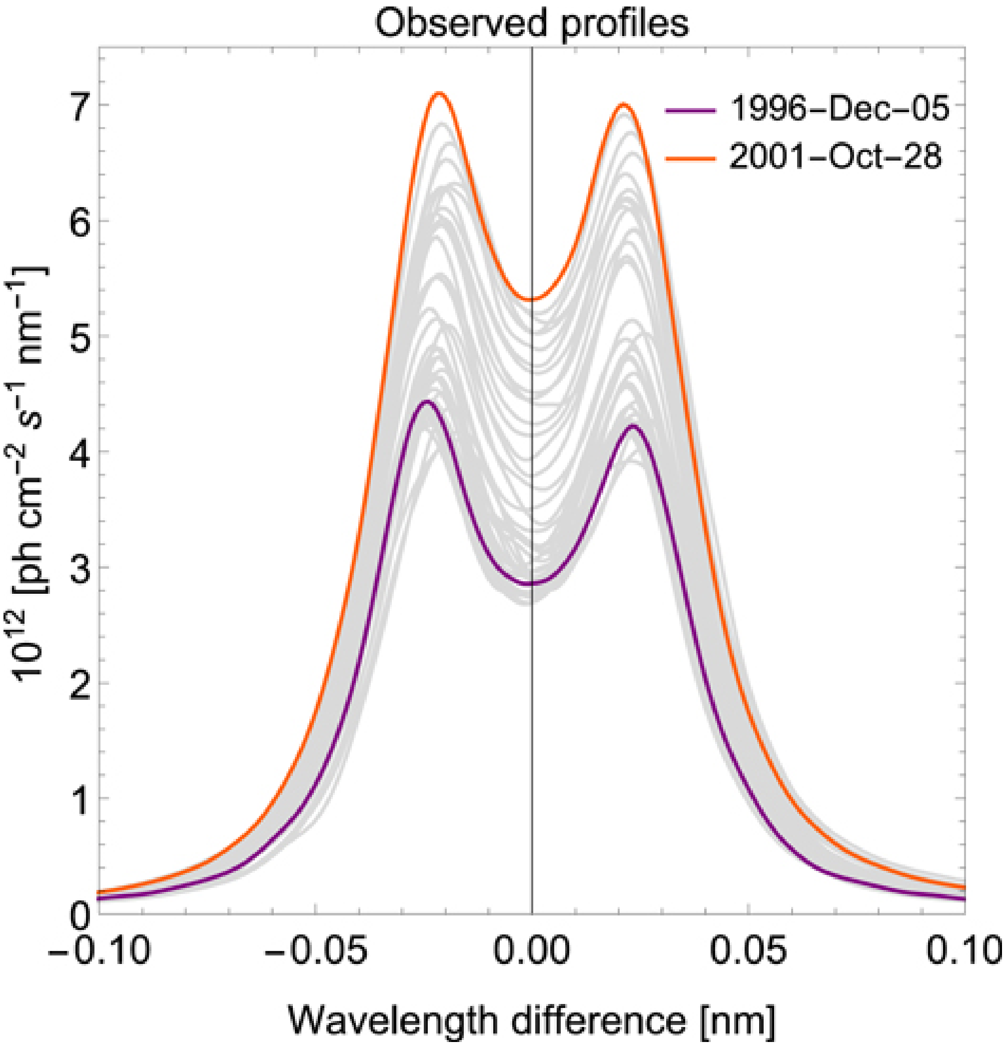

Figure 7.1 Observed profiles of disk-averaged solar Lyα line (Lemaire et al., 2015). The orange line shows a profile associated with solar maximum (2001 October 28), while the purple line represents a profile associated with solar minimum (1996 December 5). The horizontal axis is the wavelength difference from the central wavelength of the line at 121.567 nm. This figure is adopted from Kowalska-Leszczynska et al. (2018).

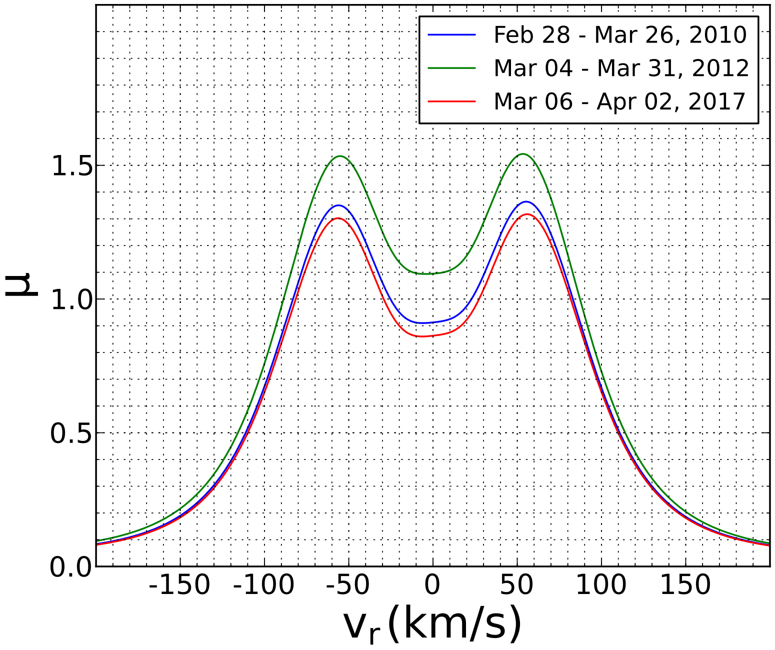

Figure 7.2 Radiation profile based on the Kowalska-Leszczynska et al. (2018) model obtained for the total irradiance averaged over one Carrington cycle for the years 2009, 2012, and 2017. The difference between solar minimum and solar maximum is significant.

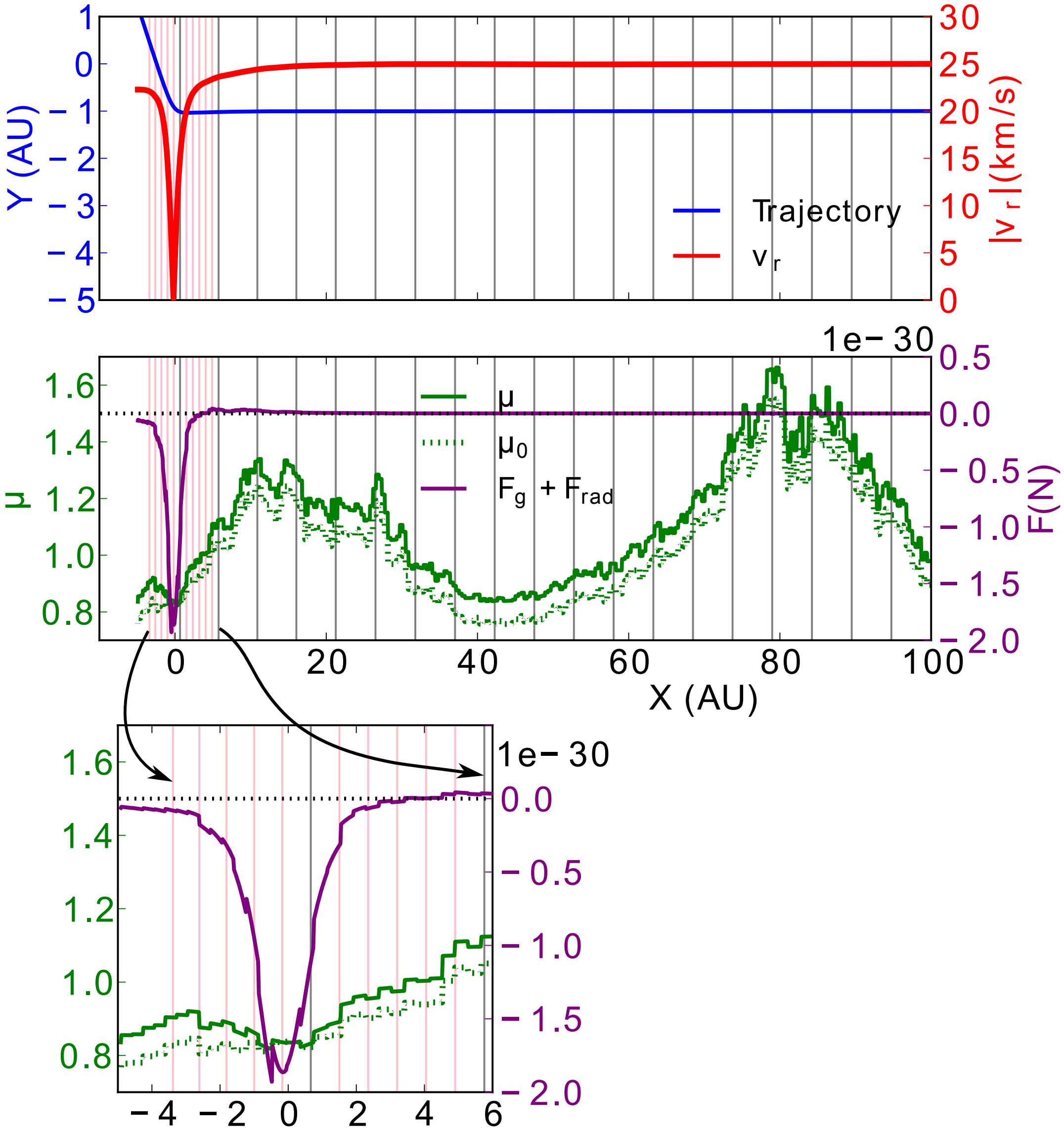

Figure 7.3 Simulated trajectory, radial velocity (top panel), net force, μ, and μ_0 both from the Kowalska-Leszczynska et al. (2018) model (middle panel) for a hypothetical H atom that starts from $x = 100$ AU and $y = -1$ AU with $v_x = -25$ km/s and $v_y = 0$ in 1998. The temporal variation of μ does not significantly affect the negligible net force far from the Sun. Therefore, the radial velocity remains constant and the H atom travels on a straight line until it gets close to the Sun, where the net force becomes large enough to reflect the temporal variations of μ while the radial velocity drops to zero almost abruptly. As can be seen here, this happens during the last two months of the trajectory (grey vertical lines represent years and pink vertical lines separate two-month periods) before the H atom reaches IBEX. More interestingly, during this phase of the journey μ almost equals μ_0, indicating that μ_0 is a good approximation for μ and the ISN H trajectory can be approximated by a hyperbola (bottom panel).

CHAPTER 8

Conclusions and Outlook

The Sun is currently exhibiting an anomalously low solar activity indicating that we may be entering an era of persistent decline in solar activity. The deep minimum of cycle 23 is the longest solar minimum in over 80 years of the space age with weaker heliospheric magnetic fields (Smith and Balogh, 2008) than observed during previous cycles. During this phase, the fast solar wind was slower, less dense and cooler, with lower mass and momentum fluxes (McComas et al., 2008). The following rising activity of the solar maximum of cycle 24 was not able to restore the solar wind mass flux and the heliospheric magnetic flux to the observed level of the previous solar maxima (McComas et al., 2013; Smith et al., 2013), making it the weakest solar maximum of the space age.

In Rahmanifard et al. (2017), I incorporated sunspot number by SILSO, as a proxy for the frequency of CMEs, with the Schwadron et al. (2010b) model to reconstruct a time series of the HMF over the last four centuries. I found timescales associated with the processes involved in the balance between CME-associated and ambient magnetic flux. I showed that a floor ≤ 1.49 nT is sufficient to successfully describe the HMF evolution even during the least active phases of the sun. In this research, I elucidated the evolution of the HMF during periods of extremely low activity including Gleissberg, Dalton, and Maunder grand minima. These results may be important in the context of the extended minimum of cycle 23 - 24 and the extremely small maximum of cycle 24, both indicative of unusually low solar activity that may persist in coming years.

The rise and fall of the HMF can drastically change our space environment, for example, the transport of the GCRs is controlled largely by the strength of the HMF fluctuations in the heliosphere. As a result of the observed extremely low solar activity, the highest fluxes GCRs in the space age have been observed. A long-term mission in deep space will expose astronauts and equipment to a different radiation dose environment than experienced previously. Schwadron et al. (2014) used the evolution of the HMF from Goelzer et al. (2013) to project dose rates of GCRs on the lunar surface predicting a $\sim 20\%$ increase in the dose rates from one solar minimum to the next since the mid-1990s. Comparing these results with actual dose rates observed by CRaTER in the last 4 years showed a 10% further increase, indicating that the radiation environment is worsening even more rapidly than in previous estimates (Schwadron et al., 2018).

In Rahmanifard et al. (2019a), I applied a more recent reconstruction of the HMF from (Rahmanifard et al., 2017) for the past solar grand minima conditions, including the Dalton minimum (1790-1830) and the Gleissberg minimum [1890-1920], to predict the dose rates of GCRs through solar cycle 25. Assuming conditions similar to the past secular minima for cycle 25 leads to a radical decrease in the modulation of the GCRs. As a result, the radiation hazard further increases from the already unprecedentedly high radiation risks, so that a shallow solar maximum similar to the one from cycle 6 (from the Dalton period) will not be able to effectively moderate the radiation environment, leading to a dose rate increase of $\sim 66\%$. Using a sophisticated risk model (de Wet et al., 2019), we found the PMD for extreme cases of a Dalton-like and a Gleissberg-like solar cycle 25.

During phases of solar minimum, similar to our current status, relatively few solar energetic particle events are expected due to the lower occurrence of solar flares and CME-driven shock waves. However, the SEP event of September 2017 was extremely hard, with the largest observed dose rates in the most shielded detectors of CRaTER, which occurred as the result of successive fast CMEs (Schwadron et al., 2018). Our results show that the lens and skin dose on the lunar surface approached the 30 day limits, although even moderate shielding (> 1 g/cm^2 Al shielding) would reduce the radiation dose below the 30 day limits.

The occurrence of the September 2017 event after more than a year of very few solar particle events shows that besides historically large GCR fluxes, discrete SEP events remain a significant hazard, emphasizing the necessity of considering the radiation environment as a critical factor in planning future space missions. Results from Rahmanifard et al. (2019a) suggest that solar maximum is probably safer for long-term space explorations due to more effective modulation of the GCRs by the heliosphere. However, during extravehicular activities, in order to avoid exposing astronauts to radiation from SEP events, which are more frequent during solar maximum, advance warning remains an imperative.

While low fluxes of high energy GCRs can reach the inner heliosphere via diffusion, ISN atoms stream into the inner heliosphere in large fluxes. Unlike the GCRs, the HMF and its variations do not affect the ISN atoms. However, they are effectively filtered by ionization processes, including charge exchange and photoionization, which impose solar cycle variations on their flux rates. For ISN H atoms, these variations are more pronounced since solar radiation pressure, which both decelerates them and shifts their peak longitude, further modifies their distribution function. The temporal and spatial variations of the radiation pressure complicate the analysis of ISN H flow. So far a limited number of studies (Schwadron et al., 2013; Katushkina et al., 2015; Kowalska-leszczynska et al., 2018) have investigated the ISN H flow in the heliosphere using IBEX data. This is due to an ongoing discrepancy in the ratio of the ISN H count rates in the lowest two energy channels between all available models and the observations.

A new release of ISN H comprehensive maps observed by IBEX (Galli et al., 2019), covering the full solar cycle 24, motivated us to study variations of ISN H signal with solar activity throughout the past 10 years. In Rahmanifard et al. (2019b), I used the longitudinal shift as an indicator of the ISN H signal variations with solar activity. In spite of the large uncertainties, the anticipated shift was indeed observed. However, the observations also suggest that the radiation pressure generally exerts a larger force than gravity.I showed that the radiation pressure obtained in this way agrees qualitatively with total irradiance intensities. A better-known response function of the instrument, which could potentially resolve the aforementioned discrepancy in the ratio of the ISN H count in the lowest two energy channels and provide higher resolution data, could lead us to observe the predicted shift more confidently. Further study of the IBEX data and the instrument response to H atoms, will help to refine our understanding of solar radiation pressure and its effect on ISN H distribution. The current anomalously low solar activity may be an indicator of entering a deep phase of a solar grand minimum. Under such conditions, Interstellar Mapping and Acceleration Probe (IMAP), selected for launch in 2024, will provide an opportunity to track the interaction between the heliosphere and the VLISM (McComas et al., 2018), by detecting ISN atoms and GCRs simultaneously, for the first time.

LIST OF REFERENCES

Abreu, J. A., Beer, J., Steinhilber, F., Tobias, S. M., and Weiss, N. O. (2008). For how long will the current grand maximum of solar activity persist? *Geophysical Research Letters*, 35(20).

Arge, C. N., Hildner, E., Pizzo, V. J., and Harvey, J. W. (2002). Two solar cycles of nonincreasing magnetic flux. *Journal of Geophysical Research: Space Physics*, 107(10).

Axford, W. I. (1972). THE INTERACTION OF THE SOLAR WIND WITH THE INTERSTELLAR MEDIUM. *Solar Wind*, 308:609–660.

Babcock, H. W. (1961). The Topology of the Sun's Magnetic Field and the 22-Year Cycle. *Astrophysical Journal*, 133:572.

Badhwar, G. D. and O'Neill, P. M. (1994). LONG-TERM MODULATION OF GALACTIC COSMIC RADIATION AND ITS MODEL FOR SPACE EXPLORATION. *International Journal of Radiation Applications and Instrumentation. Part*, 14(10):749–757.

Baranov, V. B. and Malama, Y. G. (1993). Model of the solar wind interaction with the local interstellar medium: Numerical solution of self-consistent problem. *Journal of Geophysical Research*, 98(A9):15157.

Bard, E., Raisbeck, G. M., Yiou, F., and Jouzel, J. (1997). millennium : comparison between 14C and 10Be records. *Earth and Planetary Science Letters*, 150(3-4):453–462.

Barnard, L., Lockwood, M., Hapgood, M. A., Owens, M. J., Davis, C. J., and Steinhilber, F. (2011). Predicting space climate change. *Geophysical Research Letters*, 38(16).

Beer, J. (2011). *Cosmogenic Radionuclides: Theory and Applications in the Terrestrial and Space Environments*. Springer Science+Business Media Dordrecht, Berlin.

Beer, J., Tobias, S., and Weiss, N. (1998). AN ACTIVE SUN THROUGHOUT THE MAUNDER MINIMUM JÜRG BEER 1 , STEVEN TOBIAS 2 and NIGEL WEISS 3 1. *Solar Physics*, 181(1):237–249.

Bieber, J. W. and Rust, D. M. (1995). The escape of magnetic flux from the sun. *The Astrophysical Journal*, 453:911.

Blum, P. W. and Fahr, H. J. (1970). Interaction between Interstellar Hydrogen and the Solar Wind. *Astronomy & Astrophysics*, 4:280–290.

Bochsler, P., Kucharek, H., Möbius, E., Bzowski, M., Sokół, J. M., Didkovsky, L., and Wieman, S. (2014). SOLAR PHOTOIONIZATION RATES FOR INTERSTELLAR NEUTRALS IN THE INNER HELIOSPHERE : H , He , O , AND Ne. *The Astrophysical Journal Supplement Series*, 210(12).

Brown, G. (1986). Working Group ”A” Report: Long-Term Solar Activity Predictions. In Simon, P. A., Heckman, G., and Shea, M. A., editors, *Solar-Terrestrial Predictions: Proceedings of aWorkshop at Meudon, France*, pages 1–7, Boulder, Colo. Natl. Oceanic and Atmos. Admin.

Bzowski, M. (2017). Annual Report. Technical report, Laboratory for Solar System Physics and Astrophysics Space Research Centre, Polish Academy of Sciences, Warsaw.

Bzowski, M., Fahr, H. J., Ruciński, D., and Scherer, H. (1997). Variation of bulk velocity and temperature anisotropy of neutral heliospheric hydrogen during the solar cycle. *Astronomy & Astrophysics*, 326(April):396–411.

Bzowski, M., Kubiak, M. A., Hłond, M., Sokół, J. M., Banaszkiewicz, M., and Witte, M. (2014). Neutral interstellar He parameters in front of the heliosphere 19942007. *Astronomy & Astrophysics*, 569:A8.

Bzowski, M., Kubiak, M. A., Möbius, E., Bochsler, P., Leonard, T. W., Heirtzler, D., Kucharek, H., Sokół, J. M., Hłond, M., Crew, G. B., Schwadron, N. A., Fuselier, S. A., and McComas, D. J. (2012). Neutral interstellar helium parameters based on IBEX-Lo observations and test particle calculations. *Astrophysical Journal, Supplement Series*, 198(2).

Bzowski, M., Mäkinen, T., Kyrölä, E., Summanen, T., and Quémerais, E. (2003). Latitudinal structure and north-south asymmetry of the solar wind from Lyman- α remote sensing by SWAN. *Astronomy & Astrophysics*, 408(3):1165–1177.

Bzowski, M., Möbius, E., Tarnopolski, S., Izmodenov, V. V., and Gloeckler, G. (2008). Density of neutral interstellar hydrogen at the termination shock from Ulysses pickup ion observations. *Astronomy & Astrophysics*, 491(November):7–19.

Bzowski, M. and Rucinski, D. (1995). Solar Cycle Modulation of the Interstellar Hydrogen Density Distribution in the Heliosphere. In Marsden, R. G., editor, *The High Latitude Heliosphere*, pages 467–470. Springer Netherlands, Dordrecht, 1 edition.

Bzowski, M., Sokół, J. M., Kubiak, M. A., and Kucharek, H. (2013a). Modulation of neutral interstellar He, Ne, O in the heliosphere. Survival probabilities and abundances at IBEX. *Astronomy & Astrophysics*, 557(August):A50.

Bzowski, M., Sokół, J. M., Tokumaru, M., Fujiki, K., Quémerais, E., Lallement, R., Ferron, S., Bochsler, P., and Mccomas, D. J. (2013b). Solar Parameters for Modeling the Interplanetary Backgroun. In Quémerais, E., Snow, M., and Bonnet, R. M., editors, *Cross-Calibration of Far UV Spectra of Solar System Objects and the Heliosphere*, pages 67–139. Springer New York, New York, NY.

Bzowski, M., Summanen, T., Ruciński, D., and Kyrölä, E. (2002). Response of interplanetary glow to global variations of hydrogen ionization rate and solar Lyman α flux. *Journal of Geophysical Research: Space Physics*, 107(A7).

Bzowski, M., Swaczyna, P., Kubiak, M. A., Sokół, J. M., Fuselier, S. A., Galli, A., Heirtzler, D., Kucharek, H., Leonard, T. W., McComas, D. J., Möbius, E., Schwadron, N. A., and Wurz, P. (2015). INTERSTELLAR NEUTRAL HELIUM in the HELIOSPHERE from IBEX OBSERVATIONS. III. Mach NUMBER of the FLOW, VELOCITY VECTOR, and TEMPERATURE from the FIRST SIX YEARS of MEASUREMENTS. *Astrophysical Journal, Supplement Series*, 220(2).

Caballero-Lopez, R. A., Moraal, H., McCracken, K. G., and McDonald, F. B. (2004). The heliospheric magnetic field from 850 to 2000 AD inferred from 10Be records. *Journal of Geophysical Research: Space Physics*, 109(A12):1–15.

Cameron, R. H., Jiang, J., and Schuessler, M. (2016). Solar cycle 25: another moderate cycle? *Astrophysical Journal Letters*, 823(22):5.

Cliver, E. W. (2012). The floor in the solar wind: status report. *Proceedings of the International Astronomical Union*, 7(S286):179–184.

Cliver, E. W., Boriakoff, V., and Bounar, K. H. (1998). Geomagnetic activity and the solar wind during the Maunder Minimum. *Geophysical Research Letters*, 25(6):897.

Cliver, E. W. and Ling, A. G. (2011). The Floor in the Solar Wind Magnetic Field Revisited. *Solar Physics*, 274(1-2):285–301.

Connick, D. E., Smith, C. W., and Schwadron, N. A. (2009). the Flux of Open and Toroidal Interplanetary Magnetic Field As a Function of Heliolatitude and Solar Cycle. *The Astrophysical Journal*, 695(1):357–362.

Connick, D. E., Smith, C. W., and Schwadron, N. A. (2011). Interplanetary Magnetic Flux Depletion During Protracted Solar Minima. *The Astrophysical Journal*, 727(1):8.

Cox, D. P. and Anderson, P. R. (1982). Extended adiabatic blast waves and a model of the soft X-ray background. *The Astrophysical Journal*, 253:268–289.

Crooker, N. U., Gosling, J. T., and Kahler, S. W. (2002). Reducing heliospheric magnetic flux from coronal mass ejections without disconnection. *Journal of Geophysical Research: Space Physics*, 107(A2).

Crooker, N. U., Kahler, S. W., and Gosling, J. T. (2001). Reducing heliospheric magnetic flux from CMEs without disconnection. *American Geophysical Union, Spring Meeting 2001, abstract #SH51C 04*, 107(1).

Crooker, N. U. and Owens, M. J. (2010). Impact of coronal mass ejections, interchange reconnection, and disconnection on heliospheric magnetic field strength. *arXiv.org*, 428(July 2008):279–283.

Cucinotta, F. (1993). Calculations of cosmic-ray helium transport in shielding materials. Technical report, NASA Langley Research Center; Hampton, VA, United States.

Cucinotta, F. A. (2014). Space Radiation Risks for Astronauts on Multiple International Space Station Missions. *PLoS ONE*, 9(4):96099.

Cucinotta, F. A., Alp, M., Rowedder, B., and Kim, M. H. Y. (2015). Safe days in space with acceptable uncertainty from space radiation exposure. *Life Sciences in Space Research*, 5:31–38.

Cucinotta, F. A. and Durante, M. (2006). Essay Cancer risk from exposure to galactic cosmic rays: implications for space exploration by human beings. *Lancet Oncology*, 7:431–435.

Cucinotta, F. A., Hu, S., Schwadron, N. A., Kozarev, K., Townsend, L. W., and Kim, M. H. Y. (2010). Space radiation risk limits and Earth Moon Mars environmental models. *Space Weather*, 8(12):1–12.

Cucinotta, F. A., Schimmerling, W., Wilson, J. W., Peterson, L. E., Badhwar, G. D., Saganti, P. B., and Dicello, J. F. (2001). Space radiation cancer risks and uncertainties for Mars missions. *Radiation research*, 156:682–8.

de Wet, W. C., Slaba, T. C., Rahmanifard, F., Wislon, J. K., Jordan, A. P., Townsend, L. W., Schwadron, N. A., and Spence, H. E. (2019). CRaTER Observed Permissible Mission Duration for Human Operations in Deep Space. *In preparation.*

DeForest, C. E., Howard, T. A., and McComas, D. J. (2012). Disconnecting Open Solar Magnetic Flux. *The Astrophysical Journal*, 745(1):36.

Durante, M. and Cucinotta, F. A. (2008). Heavy ion carcinogenesis and human space exploration. *Nature Reviews Cancer2008*, page 465.

Fahr, H. J. (1968). On the Influence of Neutral Interstellar Matter on the Upper Atmosphere. *Astrophysics and Space Science*, 2(4):474–495.

Fahr, H. J. (1971). The Interplanetary Hydrogen Cone and its Solar Cycle Variations. *Astronomy & Astrophysics*, 14:263.

Fahr, H. J. (1979). Interstellar hydrogen subject to a net repulsive solar force field. *Astronomy & Astrophysics*, 77:101–109.

Feynman, J. and Crooker, N. U. (1978). The solar wind at the turn of the century. *Nature*, 275(5681):626—-627.

Fisk, L. A. and Schwadron, N. A. (2001). The behavior of the open magnetic field of the Sun. *The Astrophysical Journal*, 560:425–438.

Florinski, V., Zank, G. P., and Pogorelov, N. V. (2003). Galactic cosmic ray transport in the global heliosphere. *Journal of Geophysical Research: Space Physics*, 108(6).

Frisch, P. C. (1986). The physical properties of the "Local Fluff". *Advances in Space Research*, 345(6).

Frisch, P. C., editor (2006). *Solar journey: The significance of our galactic environment for the heliosphere and earth.* Springer, Dordrecht.

Frisch, P. C., Bzowski, M., Grun, E., Izmodenov, V. V., Kruger, H., Linski, J. L., Mccomas, D. J., Möbius, E., Redfield, S., Schwadron, N. A., Shelton, R., Slavin, J. D., and Wood, B. E. (2009). The Galactic Environment of the Sun : Interstellar Material Inside and Outside of the Heliosphere. *Space Science Reviews*, 146(May):235–273.

Fuselier, S. A., Bochsler, P., Chornay, D., Clark, G., Crew, G. B., Dunn, G., Ellis, S., Friedmann, T., Funsten, H. O., Ghielmetti, A. G., Googins, J., Granoff, M. S., Hamilton, J. W., Hanley, J., Heirtzler, D., Hertzberg, E., Isaac, D., King, B., Knauss, U., Kucharek, H., Kudirka, F., Livi, S., Lobell, J., Longworth, S., Mashburn, K., McComas, D. J., Möbius, E., Moore, A. S., Moore, T. E., Nemanich, R. J., Nolin, J., O'Neal, M., Piazza, D., Peterson, L., Pope, S. E., Rosmarynowski, P., Saul, L. A., Scherrer, J. R., Scheer, J. A., Schlemm, C., Schwadron, N. A., Tillier, C., Turco, S., Tyler, J., Vosbury, M., Wieser, M., Wurz, P., and Zaffke, S. (2009). The IBEX-lo sensor. *Space Science Reviews*, 146(1-4):117–147.

Galli, A., Wurz, P., Rahmanifard, F., Möbius, E., Schwadron, N. A., Kucharek, H., Heirtzler, D., Fairchild, K., and Bzowski, M. (2019). Model-free maps of interstellar neutral hydrogen measured with IBEX between 2009 and 2018. *The Astrophysical Journal*, 871(1).

Galli, A., Wurz, P., Schwadron, N. A., Kucharek, H., Möbius, E., and Bzowski, M. (2017). The Downwind Hemisphere of the Heliosphere : Eight Years of IBEX -Lo Observations. *The Astrophysical Journal*, 851(2).

Gleeson, L. J. and Axford, W. I. (1967). COSMIC RAYS IN THE INTERPLANETARY MEDIUM. *The Astrophysical Journal*, 149:19–67.

Gleeson, L. J. and Axford, W. I. (1968). Solar Modulation of Galactic Cosmic Rays. *The Astrophysical Journal*, 154:1011.

Gleeson, L. J. and Urch, I. H. (1971). Energy losses and modulation of galactic cosmic rays. *Astrophysics and Space Science*, 11(2):288–308.

Gloeckler, G. and Geiss, J. (2001). Heliospheric and Interstellar Phenomena Deduced from Pickup Ion Observations. In *The 3-D Heliosphere at Solar Maximum*, pages 169–181. Springer Netherlands, Dordrecht.

Gloeckler, G., Möbius, E., Geiss, J., Bzowski, M., Chalov, S., Fahr, H., McMullin, D. R., Noda, H., Oka, M., Ruciński, D., Skoug, R., Terasawa, T., von Steiger, R., Yamazaki, A., and Zurbuchen, T. H. (2004). Observations of the helium focusing cone with pickup ions. *Astronomy & Astrophysics*, 426(3):845–854.

Goelzer, M. L., Smith, C. W., Schwadron, N. A., and Mccracken, K. G. (2013). An analysis of heliospheric magnetic field flux based on sunspot number from 1749 to today and prediction for the coming solar minimum. *Journal of Geophysical Research: Space Physics*, 118(December):7525–7531.

Gosling, J. T., Baker, D. N., Bame, S. J., Feldman, W. C., and Zwickl, R. D. (1987). Bidirectional solar wind electron heat flux events. *JGR*, 92 (A8):8519–8535.

Hall, D. T. (1992). *Ultraviolet resonance radiation and the structure of the heliosphere. Item type text; Dissertation-Reproduction (electronic)*. PhD thesis, The University of Arizona.

Heikkilä, U., Beer, J., Abreu, J. A., and Steinhilber, F. (2013). On the atmospheric transport and deposition of the cosmogenic radionuclides (10Be): A review. *Space Science Reviews*, 176(1-4):321–332.

Helal, H. R. and Galal, A. A. (2013). An early prediction of the maximum amplitude of the solar cycle 25. *Journal of Advanced Research*, 4(3):275–278.

Hoeksema, J. T. (1991). LARGE-SCALE SOLAR AND HELIOSPHERIC MAGNETIC FIELDS. *Adv. Space Res*, 11(1):15–24.

Holzer, T. E. (1989). Interaction between the solar wind and the interstellar medium. *Annual Review of Earth and Planetary Sciences*, 199(27).

Hu, S., Kim, M. Y., McClellan, G. E., and Cucinotta, F. A. (2009). Modeling the acute health effects of astronauts from exposure to large solar particle events. *Health Physics*, 96:465–476.

Izmodenov, V. V. (2001). Interstellar atoms in the heliospheric interface. In Scherer, K., Fichtner, H., Fahr, H. J., and Marsch, E., editors, *The Outer Heliosphere: The Next Frontiers, COSPAR Colloquiua Series*, page 23, Amsterdam. Pergamon Press.

Izmodenov, V. V. (2004). Kinetic modeling of the H atoms in the heliospheric interface: solar cycle effects. In *AIP Conference Proceedings*, volume 719, pages 47–52. AIP.

Izmodenov, V. V. and Alexashov, D. B. (2015). THREE-DIMENSIONAL KINETIC-MHD MODEL OF THE GLOBAL HELIOSPHERE WITH THE HELIOPAUSE-SURFACE FITTING. *The Astrophysical Journal Supplement Series*, 220(2):32.

Jiang, J. and Cao, J. (2018). Predicting solar surface large-scale magnetic field of Cycle 24. *Journal of Atmospheric and Solar-Terrestrial Physics*, 176:34–41.

Jokipii, J. R. (1991). Variations of the cosmic-ray flux with time. In Sonett, P. C., Giampapa, M. S., and Matthews, M. S., editors, *The Sun in Time*, pages 205–220. University of Arizona Press, Tucson.

Joyce, C. J., Schwadron, N. A., Wilson, J. K., Spence, H. E., Kasper, J. C., Golightly, M., Blake, J. B., Mazur, J., Townsend, L. W., Case, A. W., Semones, E., Smith, S., and Zeitlin, C. J. (2013). Validation of PREDICCS using LRO/CRaTER observations during three major solar events in 2012. *Space Weather*, 11(6):350–360.

Joyce, C. J., Schwadron, N. A., Wilson, J. K., Spence, H. E., Kasper, J. C., Golightly, M., Blake, J. B., Townsend, L. W., Case, A. W., Semones, E., Smith, S., and Zeitlin, C. J. (2014). Radiation modeling in the Earth and Mars atmospheres using LRO/CRaTER with the EMMREM Module. *Space Weather*, 12(2):112–119.

Katushkina, O. A., Izmodenov, V. V., Alexashov, D. B., Schwadron, N. A., and McComas, D. J. (2015). INTERSTELLAR HYDROGEN FLUXES MEASURED by IBEX-LO in 2009: NUMERICAL MODELING and COMPARISON with the DATA. *Astrophysical Journal, Supplement Series*, 220(2).

Kowalska-leszczynska, I., Bzowski, M., Sokół, J. M., and Kubiak, M. A. (2018). Evolution of the Solar Ly α Line Pro fi le during the Solar Cycle . II . How Accurate Is the Present Radiation Pressure Paradigm for Interstellar Neutral H in the Heliosphere ? *The Astrophysical Journal*, 868:49.

Kowalska-Leszczynska, I., Bzowski, M., Sokół, J. M., and Kubiak, M. A. (2018). Evolution of the Solar Ly α Line Profile during the Solar Cycle. *The Astrophysical Journal*, 852(2):115.

Krivova, N. A., Balmaceda, L., and Solanki, S. K. (2007). Reconstruction of solar total irradiance since 1700 from the surface magnetic flux. *Astronomy & Astrophysics*, 467:335–346.

Kubiak, M. A., Swaczyna, P., Bzowski, M., Sokół, J. M., Fuselier, S. A., Galli, A., Heirtzler, D., Kucharek, H., Leonard, T. W., McComas, D. J., Park, J., Schwadron, N. A., and Wurz, P. (2016). INTERSTELLAR NEUTRAL HELIUM IN THE HELIOSPHERE FROM IBEX OBSERVATIONS . IV . FLOW VECTOR , MACH NUMBER , AND ABUNDANCE OF THE WARM BREEZE. *The Astrophysical Journal Supplement Series*, 223:13pp.

Lallement, R. and Bertin, P. (1992). Northern-hemisphere observations of the nearby interstellar gas. *Astronomy & Astrophysics*, 266:479–485.

Lallement, R., Quémerais, E., Bertaux, J. L., Ferron, S., Koutroumpa, D., and Pellinen, R. (2005). Deflection of the Interstellar Neutral Hydrogen Flow Across the Heliospheric Interface. *Science*, 307(5714):1447–1449.

Lallement, R., Quemerais, E., Koutroumpa, D., Bertaux, J. L., Ferron, S., Schmidt, W., Lamy, P., Maksimovic, M., Issautier, K., Meyer-Vernet, N., Moncuquet, M., and Pantellini, F. (2010). The Interstellar H Flow: Updated Analysis of SOHOSWAN Data. In *AIP Conference Proceedings*, volume 555, pages 555–558. American Institute of Physics.

le Roux, J. A., Zank, G. P., and Ptuskin, V. S. (1999). An evaluation of perpendicular diffusion models regarding cosmic ray modulation on the basis of a hydromagnetic description for solar wind turbulence. *Journal of Geophysical Research: Space Physics*, 104(A11):24845–24862.

Lee, M. A., Kucharek, H., Möbius, E., Wu, X., Bzowski, M., and McComas, D. J. (2012). An analytical model of interstellar gas in the heliosphere tailored to interstellar boundary explorer observations. *Astrophysical Journal, Supplement Series*, 198(2).

Lee, M. A., Möbius, E., and Leonard, T. W. (2015). THE ANALYTICAL STRUCTURE OF THE PRIMARY INTERSTELLAR HELIUM DISTRIBUTION FUNCTION IN THE HELIOSPHERE. *The Astrophysical Journal Supplement Series*, 220(2):23.

Leighton, R. B. (1969). A Magneto-Kinematic Model of the Solar Cycle. *Astrophysical Journal*, 156(April):1.

Lemaire, P., Vial, J. C., Curdt, W., Schühle, U., and Wilhelm, K. (2015). Hydrogen Ly- α and Ly- β full Sun line profiles observed with SUMER/SOHO (19962009). *Astronomy & Astrophysics*, 581:A26.

Li, G., Moore, R., Mewaldt, R. A., Zhao, L., and Labrador, A. W. (2012). A twin-CME scenario for ground level enhancement events. *Space Science Reviews*, 171(141):141–160.

Lindsay, B. G. and Stebbings, R. F. (2005). Charge transfer cross sections for energetic neutral atom data analysis. *Journal of Geophysical Research*, 110(December):1–10.

Linsky, J. L., Brown, A., Gayley, K., and Diplas, A. (1993). GODDARD HIGH-RESOLUTION SPECTROGRAPH OBSERVATION OF THE LOCAL INTERSTELLAR MEDIUM AND THE DEUTERIUM/HYDROGEN RATIO ALONG THE LINE OF SIGHT TOWARD CAPELLA. *The Astrophysical Journal*, 402:694–709.

Lockwood, M. (2003). Twenty-three cycles of changing open solar magnetic flux. *Journal of Geophysical Research: Space Physics*, 108(A3):1–15.

Lockwood, M. (2013). Reconstruction and prediction of variations in the open Solar Magnetic Flux and interplanetary conditions. *Living Reviews in Solar Physics*, 10.

Lockwood, M., Barnard, L., Nevanlinna, H., Owens, M. J., Harrison, R., Rouillard, A. P., and Davis, C. J. (2013a). Reconstruction of geomagnetic activity and near-Earth interplanetary conditions over the past 167 yr Part 2: A new reconstruction of the interplanetary magnetic field. *Annales Geophysicae*, 31(4):1979–1992.

Lockwood, M., Barnard, L., Nevanlinna, H., Owens, M. J., Harrison, R. G., Rouillard, A. P., and Davis, C. J. (2013b). Reconstruction of geomagnetic activity and near-Earth interplanetary conditions over the past 167 yr - Part 1: A new geomagnetic data composite. *Annales Geophysicae*, 31(11):1957–1977.

Lockwood, M. and Fröhlich, C. (2008). Recent oppositely directed trends in solar climate forcings and the global mean surface air temperature. II. Different reconstructions of the total solar irradiance variation and dependence on response time scale. *The Royal Society*, 464.

Lockwood, M., Nevanlinna, H., Barnard, L., Owens, M. J., Harrison, R. G., Rouillard, A. P., and Scott, C. J. (2014a). Reconstruction of geomagnetic activity and near-Earth interplanetary conditions over the past 167 yr – Part 4: Near-Earth solar wind speed, IMF, and open solar flux. *Annales Geophysicae*, 32(4):383–399.

Lockwood, M., Nevanlinna, H., Vokhmyanin, M., Ponyavin, D., Sokolov, S., Barnard, L., Owens, M. J., Harrison, R. G., Rouillard, A. P., and Scott, C. J. (2014b). Reconstruction of geomagnetic activity and near-Earth interplanetary conditions over the past 167 yr – Part 3: Improved representation of solar cycle 11. *Annales Geophysicae*, 32(4):367–381.

Lockwood, M., Owens, M. J., Barnard, L., and Usoskin, I. G. (2016). AN ASSESSMENT OF SUNSPOT NUMBER DATA COMPOSITES OVER 1845 2014. *The Astrophysical Journal*, 824(1):1–17.

Lockwood, M., Rouillard, A. P., and Finch, I. D. (2009). the Rise and Fall of Open Solar Flux During the Current Grand Solar Maximum. *The Astrophysical Journal*, 700(2):937–944.

Lockwood, M., Stamper, R., and Wild, M. N. (1999). A doubling of the Sun's coronal magnetic field during the past 100 years. *Nature*, 399(3 June):437–439.

Low, B. C. (2001). Coronal mass ejections, magnetic flux ropes, and solar magnetism. *JGR*, 106:25141–25163.

Lugaz, N., Temmer, M., Wang, Y., and Farrugia, C. J. (2017). The Interaction of Successive Coronal Mass Ejections: A Review. *Solar Physics*, 292(64).

Mazur, J. E., Crain, W. R., Looper, M. D., Mabry, D. J., Blake, J. B., Case, A. W., Golightly, M. J., Kasper, J. C., and Spence, H. E. (2011). New measurements of total ionizing dose in the lunar environment. *Space Weather*, 9(7).

Mazur, J. E., Zeitlin, C., Schwadron, N., Looper, M. D., Townsend, L. W., Blake, J. B., and Spence, H. (2015). Update on Radiation Dose From Galactic and Solar Protons at the Moon Using the LRO/CRaTER Microdosimeter. *Space Weather*, 13(6):363–364.

McComas, D. J., Alexashov, D. B., Bzowski, M., Fahr, H. J., Heerikhuisen, J., Izmodenov, V. V., Lee, M. A., Möbius, E., Pogorelov, N., Schwadron, N. A., and Zank, G. P. (2012). The heliosphere's interstellar interaction: No bow shock. *Science*, 336(6086):1291–1293.

McComas, D. J., Allegrini, F., Bochsler, P., Bzowski, M., Christian, E. R., Crew, G. B., Demajistre, R., Fahr, H., Fichtner, H., Frisch, P. C., Funsten, H. O., Fuselier, S. A., Gloeckler, G., Gruntman, M., Heerikhuisen, J., Izmodenov, V., Janzen, P., Knappenberger, P., Krimigis, S., Kucharek, H., Lee, M., Livadiotis, G., Livi, S., MacDowall, R. J., Mitchell, D., Möbius, E., Moore, T., Pogorelov, N. V., Reisenfeld, D., Roelof, E., Saul, L., Schwadron, N. A., Valek, P. W., Vanderspek, R., Wurz, P., and Zank, G. P. (2009). Global observations of the interstellar interaction from the Interstellar Boundary Explorer (IBEX). *Science*, 326(5955):959–962.

McComas, D. J., Allegrini, F., Bzowski, M., Dayeh, M. A., Demajistre, R., Funsten, H. O., Fuselier, S. A., Gruntman, M., Janzen, P. H., Kubiak, M. A., Kucharek, H., Möbius, E., Reisenfeld, D. B., Schwadron, N. A., Sokół, J. M., and Tokumaru, M. (2014). IBEX: The first five years (2009-2013). *Astrophysical Journal, Supplement Series*, 213(2).

McComas, D. J., Angold, N., Elliott, H. A., Livadiotis, G., Schwadron, N. A., Skoug, R. M., and Smith, C. W. (2013). Weakest solar wind of the space age and the current "mini" solar maximum. *Astrophysical Journal*, 779(1).

McComas, D. J., Bzowski, M., Frisch, P., Fuselier, S. A., Kubiak, M. A., Kucharek, H., Leonard, T., Möbius, E., Schwadron, N. A., Sokół, J. M., Swaczyna, P., and Witte, M. (2015a). Warmer local interstellar medium: A possible resolution of the Ulysses-ibex enigma. *Astrophysical Journal*, 801(1).

McComas, D. J., Bzowski, M., Fuselier, S. A., Frisch, P. C., Galli, A., Izmodenov, V. V., Katushkina, O. A., Kubiak, M. A., Lee, M. A., Leonard, T. W., Möbius, E., Park, J., Schwadron, N. A., Sokół, J. M., Swaczyna, P., Wood, B. E., and Wurz, P. (2015b). Local interstellar medium: Six years of direct sampling by ibex. *Astrophysical Journal, Supplement Series*, 220(2).

McComas, D. J., Christian, E. R., Schwadron, N. A., Fox, N., Westlake, J., Allegrini, F., Baker, D. N., Biesecker, D., Bzowski, M., Clark, G., Cohen, C. M. S., Cohen, I., Dayeh, M. A., Decker, R., de Nolfo, G. A., Desai, M. I., Ebert, R. W., Elliott, H. A., Fahr, H., Frisch, P. C., Funsten, H. O., Fuselier, S. A., Galli, A., Galvin, A. B., Giacalone, J., Gkioulidou, M., Guo, F., Horanyi, M., Isenberg, P., Janzen, P., Kistler, L. M., Korreck, K., Kubiak, M. A., Kucharek, H., Larsen, B. A., Leske, R. A., Lugaz, N., Luhmann, J., Matthaeus, W., Mitchell, D., Möbius, E., Ogasawara, K., Reisenfeld, D. B., Richardson, J. D., Russell, C. T., Sokół, J. M., Spence, H. E., Skoug, R., Sternovsky, Z., Swaczyna, P., Szalay, J. R., Tokumaru, M., Wiedenbeck, M. E., Wurz, P., Zank, G. P., and Zirnstein, E. J. (2018). Interstellar Mapping and Acceleration Probe (IMAP): A New NASA Mission. *Space Science Reviews*, 214(8):116.

McComas, D. J., Ebert, R. W., Elliott, H. A., Goldstein, B. E., Gosling, J. T., Schwadron, N. A., and Skoug, R. M. (2008). Weaker solar wind from the polar coronal holes and the whole Sun. *Geophysical Research Letters*, 35(18):L18103.

McComas, D. J., Elliott, H. A., Gosling, J. T., and Skoug, R. M. (2006). Ulysses observations of very different heliospheric structure during the declining phase of solar activity cycle 23. *Geophysical Research Letters*, 33(9):L09102.

Mccomas, D. J., Elliott, H. A., Schwadron, N. A., and Goldstein, B. E. (2003). The three-dimensional solar wind around solar maximum. *Geophysical Research Letters*, 30(10):1–4.

McComas, D. J., Gosling, J. T., and Phillips, J. L. (1992). Interplanetary Magnetic Flux : Measurement and Balance. *Journal of Geophysical Research: Space Physics*, 97:171–177.

McComas, D. J., Gosling, J. T., Phillips, J. L., Bame, S. J., Luhmann, J. G., and Smith, E. J. (1989). Electron heat flux dropouts in the solar wind - Evidence for interplanetary magnetic field reconnection? *Journal of Geophysical Research: Space Physics*, 94:6907–6916.

McComas, D. J., Phillips, J. L., Hundhausen, A. J., and Burkepile, J. T. (1991). OF DISCONNECTION OF OPEN CORONAL Aimos National Aimos , New Mexico High

Altitude Observatory , National for Atmospheric wi [h the outward passage of CMEs in the solar corona. *Geophysical Research Letters*, 18(1):73–76.

McCracken, K., Beer, J., Steinhilber, F., and Abreu, J. (2013). The heliosphere in time. *Space Science Reviews*, 176(1-4):59–71.

McCracken, K. G. (2007). Heliomagnetic field near Earth, 1428-2005. *Journal of Geophysical Research: Space Physics*, 112(9):1–9.

McCracken, K. G. and Beer, J. (2014). Comparison of the extended solar minimum of 2006-2009 with the Spoerer, Maunder, and Dalton Grand Minima in solar activity in the past. *Journal of Geophysical Research: Space Physics*, 119(4):2379–2387.

McCracken, K. G. and Beer, J. (2015). The Annual Cosmic-Radiation Intensities 1391 ??? 2014; The Annual Heliospheric Magnetic Field Strengths 1391 ??? 1983, and Identification of Solar Cosmic-Ray Events in the Cosmogenic Record 1800 ??? 1983. *Solar Physics*, 290(10):3051–3069.

McCracken, K. G., McDonald, F. B., Beer, J., Raisbeck, G., and Yiou, F. (2004). A phenomenological study of the long-term cosmic ray modulation, 850-1958 AD. *Journal of Geophysical Research: Space Physics*, 109(A12):1–17.

McDonald, F. B. and Burlaga, L. F. (1997). Global merged interaction regions. In Jokipii, J. R., Sonett, C. P., and Giampapa, M. S., editors, *Cosmic Winds and the Heliosphere*, pages 581–616. Univ. of Ariz. Press, Tucson.

McIntosh, P. S., Brown, G. M., Buhmann, R., Clark, T., Fougere, P. F., and Hunter, H. (1979). Long-term solar activity predictions. In Donnelly, R., editor, *NASA. Marshall Space Flight Center Solar-Terrest. Predictions Proc.*, pages 246–257, Boulder, Colo. NOAA.

McKee, C. F. and Ostriker, J. P. (1977). A theory of the interstellar medium - Three components regulated by supernova explosions in an inhomogeneous substrate. *The Astrophysical Journal*, 218:148–169.

Meier, R. R. (1977). Some Optical and Kinetic Properties of the Nearby Interstellar Gas. *Astronomy & Astrophysics*, 55:211–219.

Möbius, E., Bochsler, P., Bzowski, M., Crew, G. B., Funsten, H. O., Fuselier, S. A., Ghielmetti, A., Heirtzler, D., Izmodenov, V. V., Kubiak, M. A., Kucharek, H., Lee, M. A., Leonard, T. W., McComas, D. J., Petersen, L., Saul, L., Scheer, J. A., Schwadron, N. A., Witte, M., and Wurz, P. (2009). Direct observations of interstellar H, He, and O by the interstellar boundary explorer. *Science*, 326(5955):969–971.

Möbius, E., Bochsler, P., Bzowski, M., Heirtzler, D., Kubiak, M. A., Kucharek, H., Lee, M. A., Leonard, T. W., Schwadron, N. A., Wu, X., Fuselier, S. A., Crew, G., McComas, D. J., Petersen, L., Saul, L., Valovcin, D., Vanderspek, R., and Wurz, P. (2012). Interstellar gas flow parameters derived from interstellar boundary explorer-Lo observations in 2009 and 2010: Analytical analysis. *Astrophysical Journal, Supplement Series*, 198(2).

Möbius, E., Bzowski, M., Chalov, S., Fahr, H. J., Gloeckler, G., Izmodenov, V. V., Kallenbach, R., Lallement, R., McMullin, D., Noda, H., Oka, M., Pauluhn, A., Raymond, J. C., Ruciński, D., Skoug, R., Terasawa, T., Thompson, W., Vallerga, J., von Steiger, R., and Witte, M. (2004). Synopsis of the interstellar He parameters from combined neutral gas, pickup ion and UV scattering observations and related consequences. *Astronomy & Astrophysics*, 426(3):897–907.

Müller, H. R., Florinski, V., Heerikhuisen, J., Izmodenov, V. V., Scherer, K., Alexashov, D. B., and Fahr, H. J. (2008). Special feature Comparing various multi-component global heliosphere models. *Astronomy & Astrophysics*, 491:43–51.

Muscheler, R., Joos, F., Beer, J., Müller, S. A., Vonmoos, M., and Snowball, I. (2007). Solar activity during the last 1000 yr inferred from radionuclide records. *Quaternary Science Reviews*, 26:82–97.

National Aeronautics and Space Administration (2014). NASA HANDBOOK NASA/SP-2010-3407/REV1 National Aeronautics and Space Administration. Technical report, National Aeronautics and Space Administration, Washington, DC.

NCRP (2000). Radiation protection guidance for activities in low-Earth orbit. Technical report, NCRP Tech. Rep. 132, Natl. Counc. on Radiat. Prot. and Meas, Bethesda, Md.

Nealy, J. E., Cucinotta, F. A., Wilson, J. W., Badavi, F. F., Dachev, T. P., Tomov, B. T., Walker, S. A., De Angelis, G., Blattnig, S. R., and Atwell, W. (2007). Pre-engineering spaceflight validation of environmental models and the 2005 HZETRN simulation code. *Advances in Space Research*, 40(11):1593–1610.

NRC (2008). Managing Space Radiation Risk in the New Era of Space Exploration. Technical report, Natl. Acad. Press, Washington, D.C.

NRC (2012). Technical Evaluation of the NASA Model for Cancer Risk to Astronauts due to Space Radiation. Technical report, Natl. Acad. Press, Washington, D. C.

O'Neill, P. M. (2006). Badhwar-O'Neill galactic cosmic ray model update based on advanced composition explorer (ACE) energy spectra from 1997 to present. *Advances in Space Research*, 37(9):1727–1733.

O'Neill, P. M., Golge, S., and Slaba, T. C. (2015). NASA-TP-2015-218569 - Badhwar-O'Neill 2014 Galactic Cosmic Ray Flux Model Description. Technical Report March, NASA Johnson Space Center, Houston.

Owens, M. J., Arge, C. N., Crooker, N. U., Schwadron, N. A., and Horbury, T. S. (2008). Estimating total heliospheric magnetic flux from single-point in situ measurements. *Journal of Geophysical Research: Space Physics*, 113(12):1–8.

Owens, M. J., Cliver, E., McCracken, K. G., Beer, J., Barnard, L., Lockwood, M., Rouillard, A., Passos, D., Riley, P., Usoskin, I., and Wang, Y. M. (2016). Near-Earth heliospheric magnetic field intensity since 1750: 1. Sunspot and geomagnetic reconstructions. *Journal of Geophysical Research: Space Physics*, pages 1–26.

Owens, M. J. and Crooker, N. U. (2006). Coronal mass ejections and magnetic flux buildup in the heliosphere. *Journal of Geophysical Research: Space Physics*, 111(10):1–8.

Owens, M. J., Crooker, N. U., and Lockwood, M. (2011). How is open solar magnetic flux lost over the solar cycle? *Journal of Geophysical Research: Space Physics*, 116(4):1–13.

Owens, M. J., Crooker, N. U., and Lockwood, M. (2013). Solar origin of heliospheric magnetic field inversions: Evidence for coronal loop opening within pseudostreamers. *Journal of Geophysical Research: Space Physics*, 118(5):1868–1879.

Owens, M. J. and Forsyth, R. J. (2013). The Heliospheric Forsyth, R. JMagnetic Field Imprint / Terms of Use. *Living Reviews in Solar Physics*, 10(5).

Owens, M. J. and Lockwood, M. (2012). Cyclic loss of open solar flux since 1868: The link to heliospheric current sheet tilt and implications for the Maunder Minimum. *Journal of Geophysical Research: Space Physics*, 117(4):1–9.

Owens, M. J., Lockwood, M., and Riley, P. (2017). Global solar wind variations over the last four centuries. *Nature Publishing Group*, 7(January):1–11.

Owens, M. J., Schwadron, N. A., Crooker, N. U., Hughes, W. J., and Spence, H. E. (2007). Role of coronal mass ejections in the heliospheric Hale cycle. *Geophysical Research Letters*, 34:1–5.

Owens, M. J., Usoskin, I., and Lockwood, M. (2012). Heliospheric modulation of galactic cosmic rays during grand solar minima: Past and future variations. *Geophysical Research Letters*, 39(19):1–5.

Park, J., Kucharek, H., Möbius, E., Galli, A., Kubiak, M. A., Bzowski, M., and McComas, D. J. (2016). IBEX OBSERVATIONS OF SECONDARY INTERSTELLAR HELIUM AND OXYGEN DISTRIBUTIONS. *The Astrophysical Journal*, 833(2):130.

Parker, E. N. (1958). Dynamics of the Interplanetary Gas and Magnetic Fields. *The Astrophysical Journal*, 128:664–676.

Parker, E. N. (1965). THE PASSAGE OF ENERGETIC CHARGED PARTICLES THROUGH INTERPLANETARY SPACE. *Planet. Space Sci*, 13(1):9–49.

Pesnell, W. D. (2014). Predicting Solar Cycle 24 Using a Geomagnetic Precursor Pair. *Solar Physics*, 289(6):2317–2331.

Pesnell, W. D. (2016). Predictions of Solar Cycle 24: How are we doing? *Space Weather*, 14(1):10–21.

Pryor, W. R., Ajello, J. M., McComas, D. J., Witte, M., and Tobiska, W. K. (2003). Hydrogen atom lifetimes in the three-dimensional heliosphere over the solar cycle. *Journal of Geophysical Research: Space Physics*, 108(A10):1–11.

Pryor, W. R., Gangopadhyay, P., Sandel, B., Forrester, T., Quémerais, E., Möbius, E., Esposito, L., and Stewart, I. (2008). Special feature Radiation transport of heliospheric Lyman- α from combined Cassini and Voyager data sets. *Astronomy & Astrophysics*, 28:21–28.

Quinn, P. R., Schwadron, N. A., Townsend, L. W., Wimmer-Schweingruber, R. F., Case, A. W., Spence, H. E., Wilson, J. K., and Joyce, C. J. (2017). Modeling the effectiveness of shielding in the earth-moon-mars radiation environment using PREDICCS: five solar events in 2012. *Journal of Space Weather and Space Climate*, 7:A16.

Rahmanifard, F., de Wet, W. C., Schwadron, N. A., Owens, M. J., Jordan, A. P., Wislon, J. K., Joyce, C. J., Smith, C. W., Slaba, T. C., Spence, H. E., and Townsend, L. W. (2019a). Characterization of the Space Radiation Environment Through a Modern Secular Minimum. *Space Weather*, In prepara.

Rahmanifard, F., Möbius, E., Schwadron, N. A., Galli, A., Richards, N., Kucharek, H., Sokół, J. M., Heirtzler, D., Lee, M. A., Bzowski, M., Kowalska-leszczynska, I., Kubiak, M. A., Wurz, P., Fuselier, S. A., and McComas, D. J. (2019b). Radiation Pressure from Interstellar Hydrogen Observed by IBEX Through Solar Cycle 24 . *Astrophysical Journal*, Under revi.

Rahmanifard, F., Schwadron, N. A., Smith, C. W., McCracken, K. G., Duderstadt, K. A., Lugaz, N., and Goelzer, M. L. (2017). Inferring the Heliospheric Magnetic Field Back through Maunder Minimum. *The Astrophysical Journal*, 837(2):165.

Ribes, J. C. and Nesme-Ribes, E. (1993). The solar sunspot cycle in the Maunder minimum AD 1645 to AD 1715. *Astronomy and Astrophysics*, 276:549–563.

Richardson, J. D., Liu, Y., Wang, C., and McComas, D. J. (2008). Determining the LIC H density from the solar wind slowdown. *Astron. Astrophys.*, 491:1–5.

Riedo, A., Wahlström, P., Scheer, J. A., Wurz, P., and Tulej, M. (2010). Effect of long duration UV irradiation on diamondlike carbon surfaces in the presence of a hydrocarbon gaseous atmosphere. *Journal of Applied Physics*, 108(11):1–8.

Riley, P., Lionello, R., Linker, J. A., Cliver, E., Balogh, A., Beer, J., Charbonneau, P., Crooker, N., DeRosa, M., Lockwood, M., Owens, M. J., McCracken, K. G., Usoskin, I. G., and Koutchmy, S. (2015). Inferring the Structure of the Solar Corona and Inner Heliosphere During the Maunder Minimum Using Global Thermodynamic Magnetohydrodynamic Simulations. *The Astrophysical Journal*, 802(105).

Robbrecht, E. and Berghmans, D. (2004). Automated recognition of coronal mass ejections (CMEs) in near-real-time data. *Astronomy and Astrophysics*, 425(3):1097–1106.

Robbrecht, E., Berghmans, D., and Van der Linden, R. A. M. (2009). AUTOMATED LASCO CME CATALOG FOR SOLAR CYCLE 23: ARE CMEs SCALE INVARIANT? *The Astrophysical Journal*, 691(2):1222–1234.

Russell, C. T. (1975). 3 . Polar Cap Magnetograms Polar cap magnetograms have been shown to be quite sensitive indicators of the po-. *Solar Physics*, 42(1):259–269.

Saul, L., Bzowski, M., Fuselier, S., Kubiak, M., McComas, D. J., Möbius, E., Sokół, J. M., Rodríguez, D., Scheer, J. A., and Wurz, P. (2013). Local interstellar hydrogen's disappearance at 1 au: Four years of ibex in the rising solar cycle. *Astrophysical Journal*, 767(2):1–7.

Saul, L., Wurz, P., Rodriguez, D., Scheer, J. A., Möbius, E., Schwadron, N. A., Kucharek, H., Leonard, T. W., Bzowski, M., Fuselier, S., Crew, G., and McComas, D. J. (2012). LOCAL INTERSTELLAR NEUTRAL HYDROGEN SAMPLED IN SITU BY IBEX. *The Astrophysical Journal Supplement Series*, 198(2):14.

Scherer, K., Fichtner, H., and Stawicki, O. (2002). Shielded by the wind: The influence of the interstellar medium on the environment of Earth. *Journal of Atmospheric and Solar-Terrestrial Physics*, 64(7):795–804.

Schrijver, C. J., Livingston, W. C., Woods, T. N., and Mewaldt, R. A. (2011). The minimal solar activity in 2008-2009 and its implications for long-term climate modeling. *Geophysical Research Letters*, 38(6):1–6.

Schröder, W. (1992). On the existence of the 11-year cycle in solar and auroral activity before and during the so-called Maunder Minimum. *J. Geomag. Geoelectr.*, 1:119–128.

Schwadron, N. A., Baker, T., Blake, B., Case, A. W., Cooper, J. F., Golightly, M., Jordan, A., Joyce, C., Kasper, J., Kozarev, K., Mislinski, J., Mazur, J., Posner, A., Rother, O., Smith, S., Spence, H. E., Townsend, L. W., Wilson, J., and Zeitlin, C. (2012). Lunar radiation environment and space weathering from the Cosmic Ray Telescope for the Effects of Radiation (CRaTER). *Journal of Geophysical Research E: Planets*, 117(3).

Schwadron, N. A., Blake, J. B., Case, A. W., Joyce, C. J., Kasper, J., Mazur, J., Petro, N., Quinn, M., Wilson, J. K., and Zeitlin, C. J. (2014). Special Section : Does the worsening galactic cosmic radiation environment observed by CRaTER preclude future manned deep space exploration ? *Space Weather*, 12(11):622–632.

Schwadron, N. A., Boyd, A. J., Kozarev, K., Golightly, M., Spence, H., Townsend, L. W., and Owens, M. J. (2010a). Galactic cosmic ray radiation hazard in the unusual extended solar minimum between solar cycles 23 and 24. *Space Weather*, 8(4).

Schwadron, N. A. and Bzowski, M. (2018). The Heliosphere Is Not Round. *The Astrophysical Journal*, 862(1):11.

Schwadron, N. A., Connick, D. E., and Smith, C. W. (2010b). MAGNETIC FLUX BALANCE IN THE HELIOSPHERE. *The Astrophysical Journal*, 722(September):132–136.

Schwadron, N. A., Crew, G., Vanderspek, R., Allegrini, F., Bzowski, M., DeMagistre, R., Dunn, G., Funsten, H., Fuselier, S. A., Goodrich, K., Heirtzler, D., Kucharek, H., Maynard, K., Möbius, E., McComas, D. J., and Wu, P. (2009). The Interstellar Boundary Explorer Science Operations Center. *Space Sci Rev*, 146:207–234.

Schwadron, N. A. and McComas, D. J. (2008). The solar wind power from magnetic flux. *The Astrophysical Journal*, 686(2003):L33—-L36.

Schwadron, N. A., Möbius, E., Leonard, T. W., Fuselier, S. A., McComas, D. J., Heirtzler, D., Kucharek, H., Rahmanifard, F., Bzowski, M., Kubiak, M. A., Swaczyna, P., and Frisch, P. C. (2015). DETERMINATION OF INTERSTELLAR He PARAMETERS USING FIVE YEARS OF DATA FROM THE IBEX : BEYOND CLOSED FORM APPROXIMATIONS. *The Astrophysical Journal Supplement Series*, 220:11pp.

Schwadron, N. A., Möbius, E., McComas, D. J., Bochsler, P., Bzowski, M., Fuselier, S. A., Livadiotis, G., Frisch, P. C., Müller, H. R., Heirtzler, D., Kucharek, H., and Lee, M. A. (2016a). DETERMINATION OF INTERSTELLAR O PARAMETERS USING THE FIRST TWO YEARS OF DATA FROM THE INTERSTELLAR BOUNDARY EXPLORER. *The Astrophysical Journal*, 828(2):81.

Schwadron, N. A., Moebius, E., Kucharek, H., Lee, M. A., French, J., Saul, L., Wurz, P., Bzowski, M., Fuselier, S. A., Livadiotis, G., Mccomas, D. J., Frisch, P., Gruntman, M., and Mueller, H. R. (2013). SOLAR RADIATION PRESSURE AND LOCAL INTERSTELLAR MEDIUM FLOW PARAMETERS FROM INTERSTELLAR BOUNDARY EXPLORER LOW ENERGY HYDROGEN MEASUREMENTS. *The Astrophysical Journal*, 775(September).

Schwadron, N. A., Opher, M., Kasper, J., Mewaldt, R. A., Möbius, E., Spence, H. E., and Zurbuchen, T. H. (2016b). Interstellar Mapping and Acceleration Probe (IMAP). *Journal of Physics: Conference Series*, 767:12025.

Schwadron, N. A., Owens, M. J., and Crooker, N. U. (2008). The Heliospheric Magnetic Field over the Hale Cycle. *HAL archives*, 4(1):19–26.

Schwadron, N. A., Rahmanifard, F., Wilson, J., and Jordan, A. P. (2018). Update on theWorsening Particle Radiation Environment Observed by CRaTER and Implications for Future Human Deep-Space Exploration. *Space Weather*, 16:289–303.

Schwadron, N. A., Townsend, L., Kozarev, K., Dayeh, M. A., Cucinotta, F., Desai, M., Golightly, M., Hassler, D., Hatcher, R., Kim, M. Y., Posner, A., PourArsalan, M., Spence, H. E., and Squier, R. K. (2010c). Earth-Moon-Mars radiation environment module framework. *Space Weather*, 8(1).

Shepherd, S. J., Zharkov, S., and Zharkova, V. V. (2014). Prediction of solar activity from solar background magnetic field variations in cycles 21-23. *Astrophysical Journal*, 795(1).

Smith, C. W., McCracken, K. G., Schwadron, N. A., and Goelzer, M. L. (2014). The heliospheric magnetic flux, solar wind proton flux, and cosmic ray intensity during the coming solar minimum. *Space Weather*, 12(7):499–507.

Smith, C. W. and Phillips, J. L. (1997). The role of coronal mass ejections and interplanetary shocks in interplanetary magnetic field statistics and solar magnetic flux ejection. *Journal of Geophysical Research: Space Physics*, 102:249–261.

Smith, C. W., Schwadron, N. A., and DeForest, C. E. (2013). Decline and Recovery of the Interplanetary Magnetic Field During the Protracted Solar Minimum. *The Astrophysical Journal*, 775(1):59.

Smith, E. J. and Balogh, A. (2008). Decrease in heliospheric magnetic flux in this solar minimum: Recent Ulysses magnetic field observations. *Geophysical Research Letters*, 35(22):2–5.

Sokół, J. M., Bzowski, M., Tokumaru, M., Fujiki, K., and Mccomas, D. J. (2013). Heliolatitude and Time Variations of Solar Wind Structure from in situ Measurements and Interplanetary Scintillation Observations. *Sol Phys*, 285:167–200.

Sokół, J. M., Kubiak, M. A., Bzowski, M., and Swaczyna, P. (2015). Interstellar neutral helium in the heliosphere from ibex observations. ii. the warsaw test particle model (wtpm). *The Astrophysical Journal Supplement Series*, 220:24pp.

Solanki, S. K., Schüssler, M., and Fligge, M. (2000). Evolution of the Sun's large-scale magnetic field since the Maunder minimum. *Nature*, 408(6811):445–447.

Solanki, S. K., Schüssler, M., and Fligge, M. (2002). Secular variation of the Sun's magnetic flux. *Astronomy and Astrophysics*, 383:706.

Spence, H. E., Case, A. W., Golightly, M. J., Heine, T., Larsen, B. A., Blake, J. B., Caranza, P., Crain, W. R., George, J., Lalic, M., Lin, A., Looper, M. D., Mazur, J. E., Salvaggio, D., Kasper, J. C., Stubbs, T. J., Doucette, M., Ford, P., Foster, R., Goeke, R., Gordon, D., Klatt, B., O'Connor, J., Smith, M., Onsager, T., Zeitlin, C., Townsend, L. W., and Charara, Y. (2010). CRaTER: The cosmic ray telescope for the effects of radiation experiment on the lunar reconnaissance orbiter mission. *Space Science Reviews*, 150(1-4):243–284.

Spruit, H. C. (1977). HEAT FLOW NEAR OBSTACLES IN fields behave as thermal insulators . It is not known if the field within the convection zone reaches values above the equipartition value , but if it does , for example in the toroidal subsurface fields from whic. *Solar Physics*, 55:3–34.

Steinhilber, F., Abreu, J. A., Beer, J., Brunner, I., Christl, M., Fischer, H., Heikkila, U., Kubik, P. W., Mann, M., McCracken, K. G., Miller, H., Miyahara, H., Oerter, H., and Wilhelms, F. (2012). 9,400 Years of Cosmic Radiation and Solar Activity From Ice Cores and Tree Rings. *Proceedings of the National Academy of Sciences*, 109(16):5967–5971.

Stone, E. C., Cummings, A. C., McDonald, F. B., Heikkila, B. C., Lal, M., and Webber, W. R. (2005). Voyager 1 explores the termination shock region and the heliosheath beyond. *Science*, 309(5743):2017–2020.

Svalgaard, L. . (1977). Geomagnetic activity: Dependence on solar wind parameters. Technical report, STANFORD UNIV CALIF INST FOR PLASMA RESEARCH, Boulder, Colo.

Svalgaard, L. (2007). A FLOOR IN THE SOLAR WIND MAGNETIC FIELD L. Svalgaard. *The Astrophysical Journal*, 661(1):203–206.

Svalgaard, L. and Schatten, K. H. (2016). Reconstruction of the Sunspot Group Number: The Backbone Method. *Solar Physics*, pages 1–32.

Swaczyna, P., Bzowski, M., Kubiak, M. A., Fuselier, S. A., Heirtzler, D., Kucharek, H., Leonard, T. W., McComas, D. J., and Schwadron, N. A. (2015). INTERSTELLAR NEUTRAL HELIUM IN THE HELIOSPHERE FROM IBEX OBSERVATIONS . I . UNCERTAINTIES AND BACKGROUNDS IN THE DATA AND PARAMETER DETERMINATION METHOD. *The Astrophysical Journal Supplement Series*, 220:21pp.

Tarnopolski, S. and Bzowski, M. (2009). Neutral interstellar hydrogen in the inner heliosphere under the influence of wavelength-dependent solar radiation pressure. *Astronomy & Astrophysics*, 493(1):207–216.

Thomas, G. E. (1978). The Interstellar Wind and its Influence on the Interplanetary Environment. *Annual Review of Earth and Planetary Sciences*, 6(1):173–204.

Tooley, C. R., Houghton, M. B., Saylor, R. S., Peddie, C., Everett, D. F., Baker, C. L., and Safdie, K. N. (2010). Lunar reconnaissance orbiter mission and spacecraft design. *Space Science Reviews*, 150(1-4):23–62.

Townsend, L. W., Pourarsalan, M., Cucinotta, F. A., Kim, M. Y., and Schwadron, N. A. (2011). Transmission of galactic cosmic rays through Mars atmosphere. *Space Weather*, 9(11).

Upton, L. A. and Hathaway, D. H. (2018). An Updated Solar Cycle 25 Prediction With AFT: The Modern Minimum. *Geophysical Research Letters*, 45(16):8091–8095.

Usoskin, I. G. (2013). A History of solar activity over millennia. *Living Reviews in Solar Physics*, 10(1):1–88.

Usoskin, I. G., Arlt, R., Asvestari, E., Hawkins, E., Käpylä, M., Kovaltsov, G. A., Krivova, N., Lockwood, M., Mursula, K., Reilly, J. O., Owens, M. J., Scott, C. J., Sokolo, D. D., Solanki, S. K., Soon, W., and Vaquero, J. M. (2015). The Maunder minimum (1645 1715) was indeed a grand minimum : A reassessment of multiple datasets. *Astronomy & Astrophysics*, 581.

Usoskin, I. G., Kovaltsov, G. A., Lockwood, M., Mursula, K., Owens, M., and Solanki, S. K. (2016). A New Calibrated Sunspot Group Series Since 1749: Statistics of Active Day Fractions. *Solar Physics*, pages 1–24.

Usoskin, I. G., Mursula, K., Solanki, S., Schuessler, M., and Alanko, K. (2003). Reconstruction of solar activity for the last millennium using ˆ10Be data. *Astronomy*, 751:745–751.

Usoskin, I. G., Solanki, S. K., and Kovaltsov, G. A. (2012). Grand minima of solar activity during the last millennia. *Comparative Magnetic Minima: Characterizing Quiet Times in the Sun and Stars*, 286(286):372–382.

Vallerga, J., Lallement, R., Lemoine, M., Dalaudier, F., and McMullin, D. (2004). EUVE observations of the helium glow: Interstellar and solar parameters. *Astronomy & Astrophysics*, 426(3):855–865.

Vaquero, J. M., Kovaltsov, G. A., Usoskin, I. G., Carrasco, V. M. S., and Gallego, M. C. (2015). Level and length of cyclic solar activity during the Maunder minimum as deduced from the active day statistics. *Astronomy & Astrophysics*, 577:A71.

Vasyliunas, V. M. and Siscoe, G. L. (1976). On the flux and the energy spectrum of interstellar ions in the solar system. *Journal of Geophysical Research*, 81(7):1247–1252.

Vieira, L. E. A. and Solanki, S. K. (2010). Evolution of the solar magnetic flux on time scales of years to millenia. *Astronomy & Astrophysics*, 509(100):1–13.

Wang, Y., Lean, J., and Sheeley, N. R. (2000). The long-term variation of the Sun' s open magnetic flux. *Geophysical Research Letters*, 27(4):505.

Wang, Y. M. (2017). Surface Flux Transport and the Evolution of the Sun's Polar Fields.

Wang, Y.-M. and Colaninno, R. (2014). Is Solar Cycle 24 Producing More Coronal Mass Ejections Than Cycle 23? *The Astrophysical Journal*, 784(2):L27.

Wang, Y. M. and Sheeley, N. R. (2003). ON THE TOPOLOGICAL EVOLUTION OF THE CORONAL MAGNETIC FIELD DURING THE SOLAR CYCLE. *The Astrophysical Journal*, 599:1404–1417.

Wang, Y.-M. and Sheeley, N. R. (2013). the Solar Wind and Interplanetary Field During Very Low Amplitude Sunspot Cycles. *The Astrophysical Journal*, 764(1):90.

Webber, W. R. and Lockwood, J. A. (1988). Characteristics of the 22-year modulation of cosmic rays as seen by neutron monitors. *Journal of Geophysical Research*, 93(A8):8735.

Wilson, J. W. and Badavi, F. F. (1986). Methods of Galactic Heavy Ion Transport. *Radiation Research*, 108(3):231–237.

Wilson, J. W., Nealy, J. E., de Angelis, G., Clowdsley, M. S., and Badavi, F. F. (2003). Deep Space Environment and Shielding. In *AIP Conference Proceedings*, pages 993–1010. AIP Publishing.

Witte, M. (2004). Kinetic parameters of interstellar neutral helium. *Astronomy & Astrophysics*, 426(3):835–844.

Wood, B. E., Müller, H. R., Bzowski, M., Sokół, J. M., Möbius, E., Witte, M., and McComas, D. J. (2015). Exploring the possibility of O and Ne contamination in ulysses observations of interstellar helium. *Astrophysical Journal, Supplement Series*, 220(2).

Woods, T. N., Prinz, D. K., Rottman, G. J., London, J., Crane, P. C., Cebula, R. P., Hilsenrath, E., Brueckner, G. E., Andrews, M. D., White, O. R., Vanhoosier, M. E., Floyd, L. E., Herring, L. C., Knapp, G., Pankratz, C. K., and Reiser, A. (1995). Validation of the

UARS solar ultraviolet irradiances: Comparison with the ATLAS I and 2 measurements. *The Astrophysical Journal*, 442(6):898–906.

Woods, T. N., Tobiska, W. K., Rottman, G. J., and Worden, R. (2000). Improved solar Lyman irradiance modeling from 1947 through 1999 based on UARS observations. *Journal of Geophysical Research: Space Physics*, 105.

Wu, F. M. and Judge, D. L. (1979). Temperature and flow velocity of the interplanetary gases along solar radii. *The Astrophysical Journal*, 231(July):594–605.

Wurz, P., Saul, L., Scheer, J. A., Möbius, E., Kucharek, H., and Fuselier, S. A. (2008). Negative helium generation upon surface scattering : Application in space science. *Journal of Applied Physics*, 103:054904.

Wurz, P., Schletti, R., and Aellig, M. R. (1997). Hydrogen and oxygen negative ion production by surface ionization using diomond surfaces. *Surface Science*, 373:56–66.

Yoshida, A. (2014). Difference between even- and odd-numbered cycles in the predictability of solar activity and prediction of the amplitude of cycle 25. *Annales Geophysicae*, 32(8):1035–1042.

Zank, G. P. and Frisch, P. C. (1999). Consequences of a Change in the Galactic Environment of the Sun. *The Astrophysical Journal*, 518:965–973.

Zank, G. P., Heerikhuisen, J., Wood, B. E., Pogorelov, N. V., Zirnstein, E., and McComas, D. J. (2013). Heliospheric structure: The bow wave and the hydrogen wall. *Astrophysical Journal*, 763(1).

Zank, G. P., Pauls, H. L., Williams, L. L., and Hall, D. T. (1998). Interaction of the solar wind with the local interstellar medium: A multifluid approach. *Journal of Geophysical Research: Space Physics*, 101(A10):21639–21655.

Zolotova, N. V. and Ponyavin, D. I. (2015). The Maunder Minimum is not as grand as it seemed to be. *Astrophysical Journal*, 800(42).

APPENDIX A

Derivation of Parker Spirals

Let's start with the assumtions that are widely accepted in the heliospheric physics:

1- Assuming a constant solar wind flow, requires the radial component of the HMF, B_r, to fall off quadratically with the heliocentric distance, R, to keep the magnetic flux conserved. Therefore, in a spherical coordinate (distance R, colatitude θ and longitude ϕ), we can write:

$$B_R(R, \theta, \phi) = B_R(R_0, \theta, \phi_0)(\frac{R_0}{R})^2 \tag{A.1}$$

where $B_R(R_0, \theta, \phi_0)$ is the radial component of the HMF at the source surface (distance R_0 from the Sun), at colatitude θ, and with its footpoint fixed at longitude ϕ_0.

2- Under the assumptions of steady-state solar wind, the frozen-in magnetic field and the plasma flow vectors are always parallel in the frame of reference rotating with the Sun:

$$\frac{B_\phi(R, \theta, \phi)}{B_R(R, \theta, \phi)} = \frac{V_\phi}{V_R} = \frac{-\Omega R \sin\theta}{V_R} \tag{A.2}$$

where V_R is the asymptotic Solar wind speed in the inertial frame, and V_ϕ is the azimuthal solar wind speed in the reference frame rotating with the mean solar rotation speed, Ω. The $\sin(\theta)$ leadis in a decrease in the speed of footpoint motion with latitude. substituting Equation (1) into Equation (2) obtains the azimuthal componant of the magnetic field:

$$B_\phi(R, \theta, \phi) = -B_R(R_0, \theta, \phi_0)\frac{\Omega R_0^2 \sin\theta}{V_R R} \tag{A.3}$$

3- The assumption of an exactly radial solar wind flow gives:

$$B_\theta(R, \theta, \phi) = 0 \tag{A.4}$$

Combining Equations (1), (3), and (4) obtains the HMF vector **B**, first described by Eugene Parker (and called the Parker spiral), which is a subset of the Archimedean spiral:

$$\mathbf{B}(R, \theta, \phi) = B_R(R_0, \theta, \phi_0)(\frac{R_0}{R})^2 \hat{e_r} - B_R(R_0, \theta, \phi_0)\frac{\Omega R_0^2 \sin\theta}{V_R R}\hat{e_\phi} \tag{A.5}$$

APPENDIX B

Sunspot Group Number

Along with all other updates, this study takes advantage of the new release of the sunspot number and sunspot group number by Sunspot Index and Long-term Solar Observations (SILSO) presented in Svalgaard and Schatten (2016). They have applied a backboning method to original sources to reconstruct the group number rather than comparing and correcting the existing series. Their method is solely based on the solar index and does not utilize other proxies (for example auroral sightings, geomagnetic records or radionuclides). There are other sunspot and group sunspot number data sets proposed by other groups (for example Lockwood et al. 2016; Usoskin et al. 2016; Vaquero et al. 2015). Usoskin et al. (2016) have employed a novel method to calibrate the quality of data by different observers and obtain a new series 1749-1900. Calibrating these data with data from the Royal Greenwich Observatory for the period 1749-1900, readily extended to the present day using the SOON data, they have composited a homogeneous series since 1749. Vaquero et al. (2015) used three different levels of conservatism to assess inactive days (days with no sunspot records) and evaluate the level and length of solar cycle based on original sources. They generated a database of reliable sunspot observation around the Maunder minimum (1637-1715) with sunspot numbers not greater than 10 (in the most conservative model). Lockwood et al. (2016) evaluated the new sunspot data composites over the interval 1845-2014 by comparing six data series for sunspot number including the data series by Usoskin et al. (2016) and the new backbone data series by Svalgaard and Schatten (2016), used in this study. Lockwood et al. (2016) have shown problems with the method used to generate the backbone series, which results in an accumulative overestimation of the sunspot group numbers going back in time.

In this study we need to use a data set that covers the Maunder period and persists to the present day so it can be compared to CME rate data. The sunspot group number released by SILSO and presented by Svalgaard and Schatten (2016) meets both these criteria. The new annual sunspot number data set dates back to 1700 as did the old one. However, it is corrected by lowering all numbers after 1947 by 18% to remove the influence of a different counting technique applied in Zrich since then (`http://sidc.oma.be/press/01/welcome.html`). Also as can be seen in Figure B.2 and Figure B.3 there is a significant underestimation before 1850 in the old group number, causing a significant discrepancy between the sunspot number and the group number that is corrected in the reconstruction of the group number Svalgaard and Schatten (2016). This correction leads to more pronounced group numbers for the Maunder period, which leads to more remarkable values for the HMF. Figures B.1 to B.4 are adapted from `http://sidc.oma.be/press/01/welcome.html`.

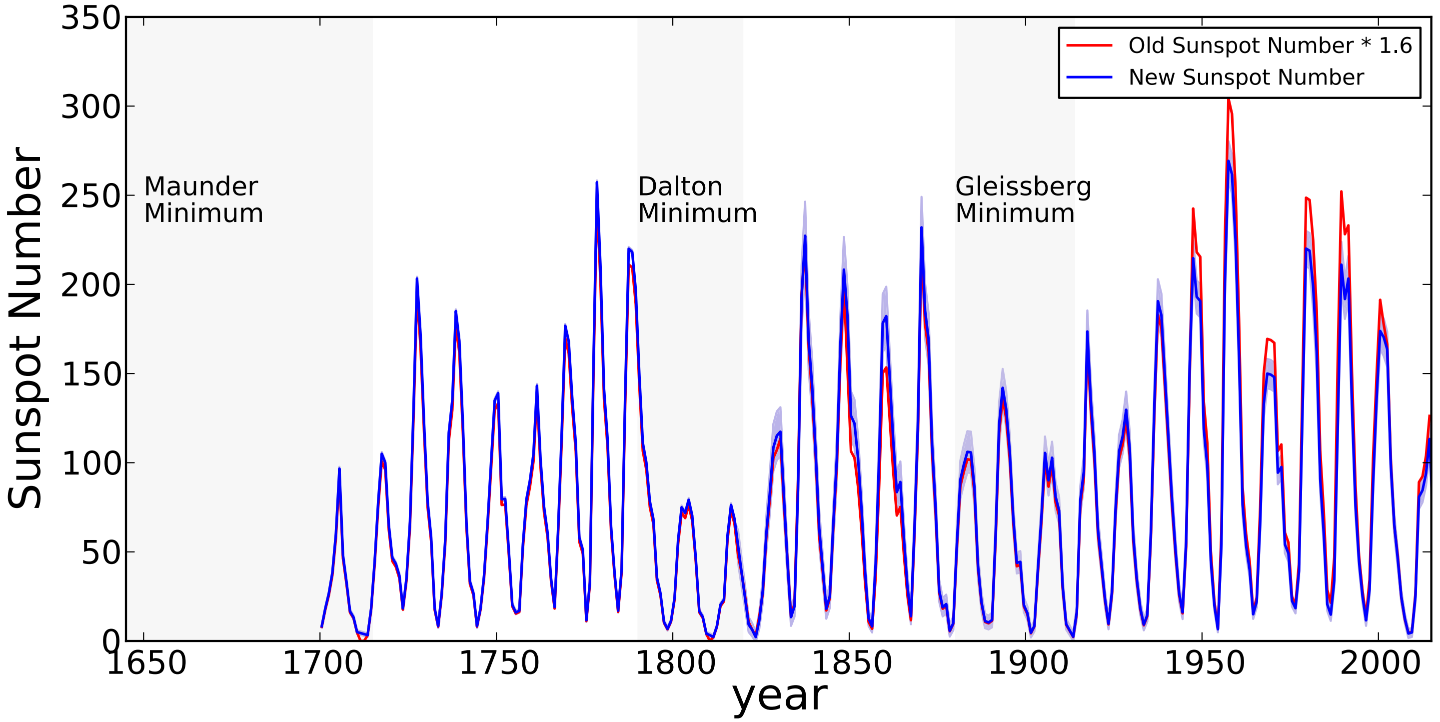

Figure B.1 The old sunspot number (red) is compared to the new sunspot number (blue) since 1700. The shaded blue regions show the uncertainty associated with the new sunspot numbers. A decrease in the new sunspot numbers can be noticed since 1947.

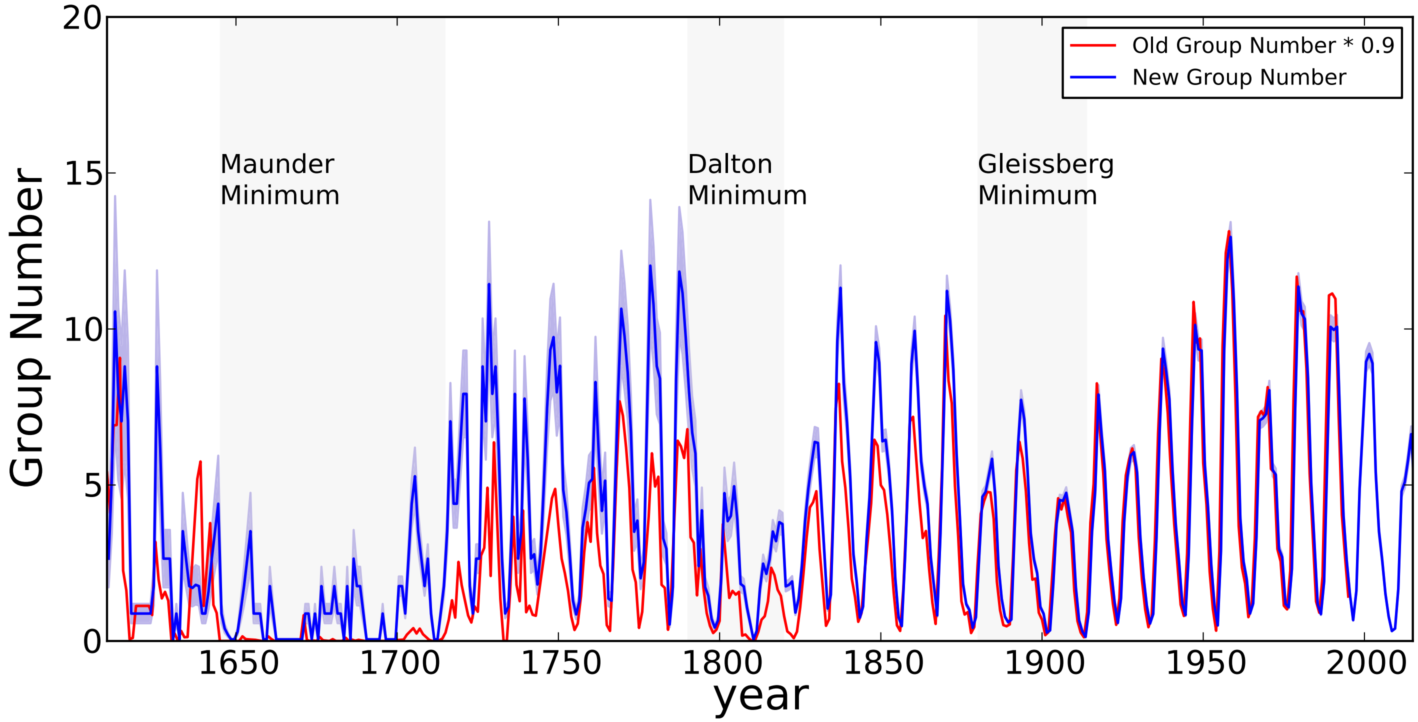

Figure B.2 The old sunspot group number (red) is compared to the new sunspot group number (blue) since 1700. The shaded blue regions show the uncertainty associated with the new sunspot group numbers. As can be see the group numbers are largely increased in the new set.

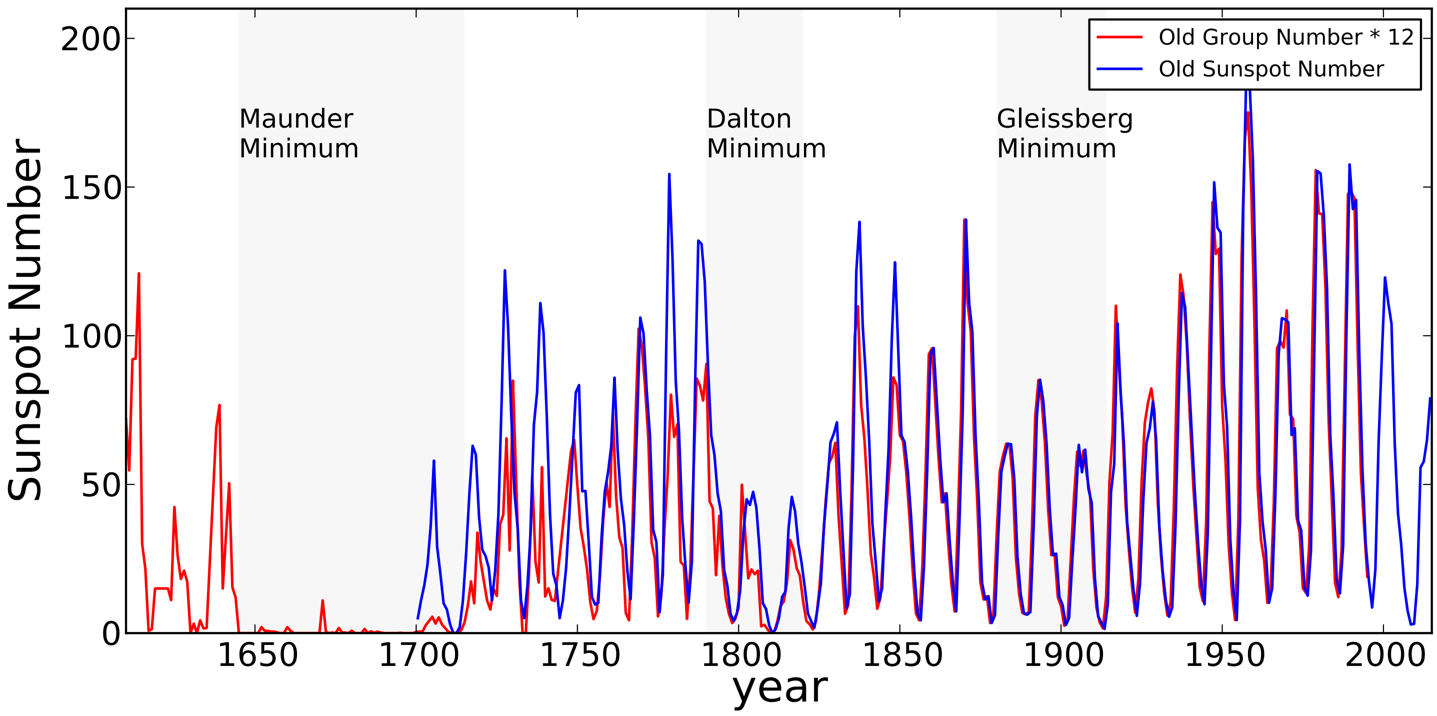

Figure B.3 The old sunspot group number (red) is compared to the old sunspot number (blue) since 1700. The so-called discrepancy between the sunspot numbers and group numbers is notable in this figure.

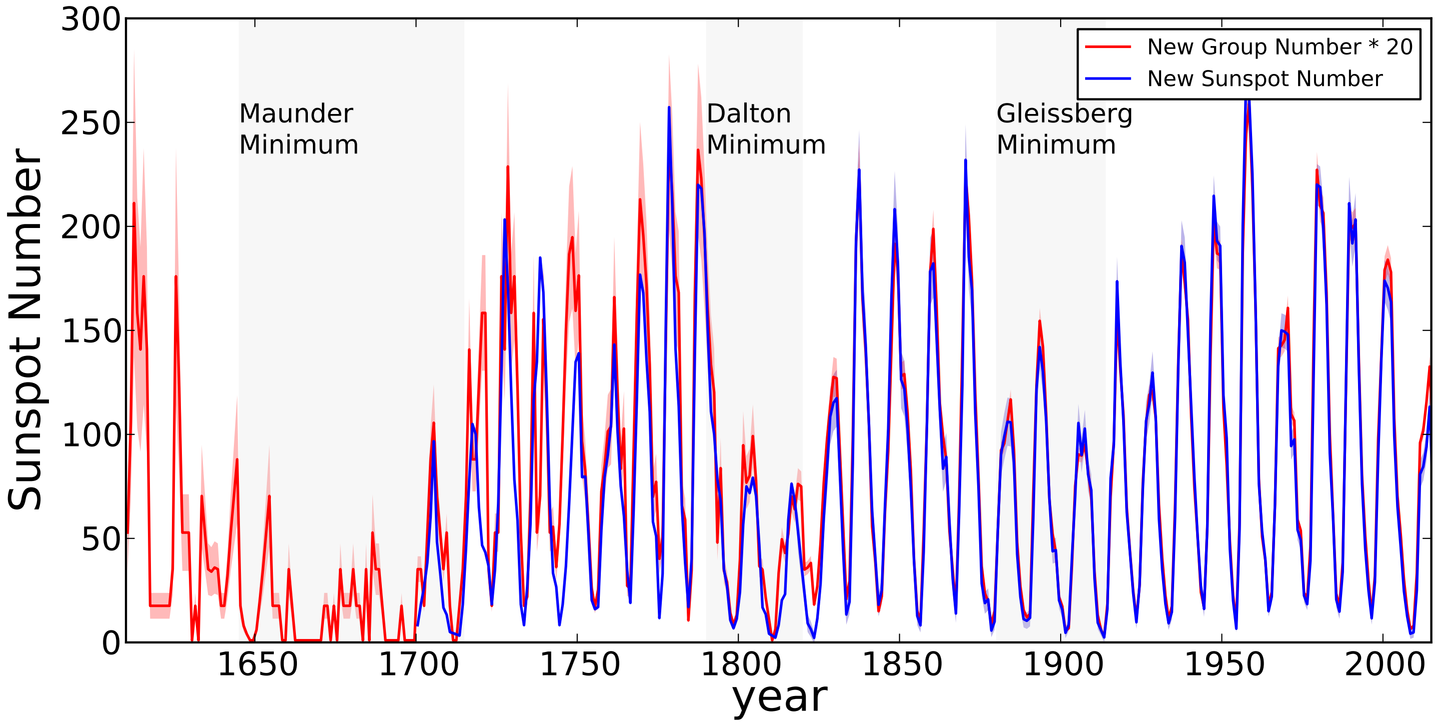

Figure B.4 The new sunspot group number (red) is compared to the new sunspot numbers (blue) since 1700. The shaded blue regions show the uncertainty associated with the new sunspot numbers. The shaded red regions show the uncertainty associated with the new sunspot group numbers.